UNIVERSITÀ DI SIENA 1240

Department of Physical Sciences, Earth and Environment

PhD in Experimental Physics

XXXIII Cycle

Coordinator: Prof. Riccardo Paoletti

State-of-the-Art Setups for K-Edge Imaging

Disciplinary Scientific Sector: FIS/07

PhD Student
Vittorio Di Trapani
University of Siena
Via Roma 56

Supervisor
Prof. Pasquale Delogu
University of Siena

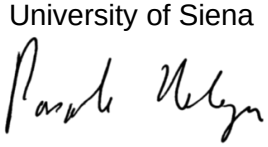

Academic Year 2019/2020

ABSTRACT

Spectral imaging is an emerging area of X-ray imaging that includes all the techniques which exploit the energy-dependent absorption properties of the matter to either provide quantitative information about the scanned object or to discriminate different materials. Though the potentials of spectral imaging are well known for over many years, the interest on spectral techniques is rapidly increasing only in recent years due to the development and widespread of dedicated acquisition systems able to acquire simultaneous (or nearly simultaneous) X-ray images at different energies. In this context, the development of energy resolving X-ray photon counting detectors (XPCDs) and the increasing availability of synchrotron radiation can provide interesting solutions for spectral imaging applications such as e.g. the K-edge technique. This thesis presents the implementation and the optimization of two state-of-the art acquisition systems suitable for spectral imaging applications with particular interest on the K-edge technique. The first system is an acquisition setup for spectral Computed Tomography (CT) made by coupling a polychromatic source with an energy resolving XPCD implementing two energy thresholds. The work carried out with this setup concerned the thorough characterization of an innovative XPCD featuring a sharp energy resolution, the design of a dedicated image processing procedure to achieve high quality CT images and the development of an automated procedure to produce accurate 3D maps of a K-edge element within a sample. Moreover, to allow further optimization studies, a simulator able to reproduce X-ray images with energy resolving XPCDs has been modeled, developed and validated. The last part of this thesis presents the development and the implementation of an acquisition setup for spectral imaging at synchrotron sources based on bent-Laue crystal optics. The results achieved with a prototype setup optimized for energies around 20 keV are presented, the future developments of the technique are discussed.

ACKNOWLEDGMENTS

I warmly thank all the members of the KISS, KEST and SYRMA-3D collaborations. I sincerely thank my supervisor, prof. Pasquale Delogu for his support and guidance during my Master's degree and my PhD program. I really thank also dr. Francesco Brun for sharing with me his incomparable knowledge of image processing and above all for his friendship and encouraging esteem. I wish to thank dr. Silvia Cipiccia and dr. Darren Batey for involving me in their interesting and fruitful experimental activity at the I13 beamline of Diamond light source (Didcot, UK). A warm thank also to dr. Alberto Bravin, his valuable comments in my first research papers were very helpful. Last but not least, I want to express my gratitude to prof. Dean Chapman for welcoming me in his group at the University of Saskatchewan (Saskatoon, Canada), his enthusiastic approach to the research activity was an inspiring example.

CONTENTS

ACRONYMS

ASIC Application Specific Integrated Circuit

ASTRA All Scales Tomographic Reconstruction Antwerp

BMD Basis Material Decomposition

BMIT Biomedical imaging and Therapy

CNR Contrast to Noise Ratio

CLS Canadian Light Source

CT Computed Tomography

DSCT Dual source CT scanner

ESF Edge Spread Function

ESRF European Synchrotron Radiation Facility

FN false negatives

FP false positives

FBP Filtered Back-Projection

FDK Feldkamp, Davis and Kress

FWHM Full Width Half Maximum

INFN Italian National Institute of Nuclear Physics

KES K-Edge Subtraction

KEST K-Edge Spectral μ-Tomography

KISS K-edge Imaging with Synchrotron Sources

LSF Line Spread Function

MC Monte Carlo

MTF Modulation Transfer Function

NEQ Noise Equivalent number of Quanta

NNPS Normalized Noise Power Spectrum

NPS Noise Power Spectrum

NPI Neighbor Pixel Inhibit mode

NPISUM Neighbor Pixel Inhibit and SUmming Mode

PM Pixel Mode

ROI Region Of Interest

SNR Signal to Noise Ratio

SR Synchrotron radiation

SYRMEP SYnchrotron Radiation for MEdical Physics

TP true positives

TIGRE Tomographic Iterative GPU-based Reconstruction Toolbox

XPCD X-ray Photon Counting Detector

INTRODUCTION

Thanks to the ability of penetrating through the matter, X-rays revolutionized the history of diagnostics in medicine. Since the very first days of their discovery [1] (1985, Wilhelm Conrad Röntgen) the potentials of X-rays were clear to its discoverer who soon produced the first image of the bone of his wife's hand. In the following years, the use of X-rays was widely recognized as an essential tool for clinical care [2]. Nowadays, at more than a century after the X-rays discovery, X-ray imaging is part of our daily lives, finding application in many fields, from medical diagnostics to airport security and industrial research. The continuous demand for improving the diagnostic quality of images available to physicians as well as the expansion of variety and scope of available imaging technologies make of X-ray imaging an exciting and challenging field still after many years from the first application.

Spectral imaging is a branch of X-ray imaging that aims at improving the knowledge about the sample by exploiting the characteristic energy dependence of the attenuation properties of different materials. As an example, K-Edge Subtraction (KES) technique exploits the strong increase in the absorption at the binding energy of the K-shell of elements (e.g. iodine, barium or gadolinium) embeddable in injectable pharmaceuticals (contrast agents). This imaging technique requires the acquisition of two images respectively below and above the target K-edge to provide suitable quantitative information about the distribution of the contrast agent within the sample. More generally, for clinical applications spectral techniques offer the attractive possibility of both observing and quantifying multiparameter events, thus providing insights into biological processes with valuable diagnostic capabilities.

In order to exploit the energy content of X-ray images, the implementation of spectral imaging requires the acquisition of a sample with at least two different X-ray energies. These images are then processed by spectral algorithms to extract the information of interest from the sample. In the context of spectral imaging, the main challenge is represented by the design and implementation of acquisition setups capable of acquiring simultaneous images of the sample at different energies in the shortest time possible, thus minimizing motion artifacts and allowing a proper application of spectral algorithms.

This thesis focuses on the development of two state-of-the art setups for spectral imaging, with particular interest on the KES technique. The first setup involves the use of a spectral X-ray Photon Counting Detector (XPCD) and looks mainly at the daily clinical practice; the

second setup, mainly devoted to research purposes at synchrotron sources, uses bent-Laue crystal optics to prepare a polychromatic X-ray spectrum focused at the sample. The experimental activity of this work has been carried out within the two projects K-Edge Spectral μ-Tomography (KEST) [3] and K-edge Imaging with Synchrotron Sources (KISS), both funded by the Italian National Institute of Nuclear Physics (INFN).

This thesis is organized in 5 chapters that can be outlined as follows.

Chapter 1 provides a brief introduction to X-ray imaging and to the Computed Tomography (CT) technique.

Chapter 2 introduces the physics underlying spectral imaging with particular interest on KES technique. In this chapter, the main spectral algorithms for the segmentation and quantification of a contrast agent within the sample are presented. The last section of the chapter is devoted to the description of the main designs for the implementation of acquisition systems dedicated to spectral imaging. In particular, the main characteristics and strengths of the two setups for spectral imaging, object of this thesis, are presented.

Chapter 3 presents the technology of XPCD: challenges and state-of-the art. The main subject of this chapter is the innovative Pixirad-1/pixie-iii XPCD implementing acquisition modes specifically designed to improve both the spatial and the spectral resolution achievable. The thorough characterization of the pixie-iii acquisition system provided in this chapter proved that the system shows energy resolution and imaging features suitable for spectral imaging applications.

Chapter 4 focuses on the implementation and characterization of an acquisition setup for single-shot spectral micro-CT implementing the Pixirad-1/pixie-iii XPCD. The sections present the experimental setup, the workflow developed to obtain artifact-free KES-CT images and the main results achieved within the KEST collaboration. Among the main results, a simulator for X-ray imaging with spectral XPCDs and polychromatic sources has been implemented and validated. Finally, in perspective of *in vivo* applications, a protocol for low dose KES imaging with spectral XPCDs exploiting discrete reconstruction algorithms has been established.

Chapter 5 presents the synchrotron setup for spectral imaging with bent-Laue optics. The physics of crystal optics is briefly introduced. The necessary characteristics of Si crystals to achieve polychromatic beams focused at the sample and optimized for the target K-edge energies are described. Finally, a prototype setup including a bent-Laue crystal optimized for energies around 20 keV has been implemented at the SYnchrotron Radiation for MEdical Physics (SYRMEP) beamline of Elettra synchrotron (Trieste). The preliminary results obtained with this setup are presented and discussed.

1

INTRODUCTION TO X-RAY IMAGING

The simplest implementation of X-ray imaging requires an X-ray source, an object to be imaged, and an X-ray detector. The basic idea of X-ray imaging is the following: a homogeneous X-ray beam interacts with a sample, in this process a fraction of photons is absorbed by the matter depending on its thickness and chemical composition while the outcoming radiation bearing information about the object is registered by an X-ray detector as a grayscale image. This image reproduces the internal morphology of the scanned object.

1.1 INTERACTION RADIATION-MATTER

In the range of energies of medical imaging (18 keV-140 keV), the main mechanisms of interaction radiation-matter summarized in Figure 1.1 are the following:

- **Photoelectric Absorption**: the energy of an X-ray photon is totally absorbed by the atom; as consequence an energetic photoelectron is released. When an electron is kicked out from its shell, the vacancy left is replaced by one electron from the outer shell. In this case, the photoelectric absorption is followed by the emission of a characteristic X-ray (fluorescence).
- **Compton scattering**: inelastic scattering. A fraction of the energy of the incident X-ray is converted into kinetic energy of a quasi-free electron of the target atom; the scattered X-ray has a lower energy when continuing its path through the matter.
- **Rayleigh scattering**: elastic scattering where the incident and the scattered X-ray have equal energy, but different directions.

The probability per unit of length for an X-ray photon to interact with one of the mechanisms above mentioned is described by the linear attenuation coefficient μ (cm^{-1}). This parameter is a function of the energy of the X-ray photon, the atomic number Z, and the density ρ of the material interacting with the X-ray radiation. In more detail, the linear attenuation coefficient can be written as a function of the integral cross sections σ of the related matter-interaction mechanisms:

$$\mu = \frac{\rho N_A}{A} \cdot \sigma_{tot} \tag{1.1}$$

where A is the atomic weight of the atom interacting with the X-ray and $\sigma_{tot} = \sigma_R + \tau + \sigma_C$ is the global cross-section including the cross

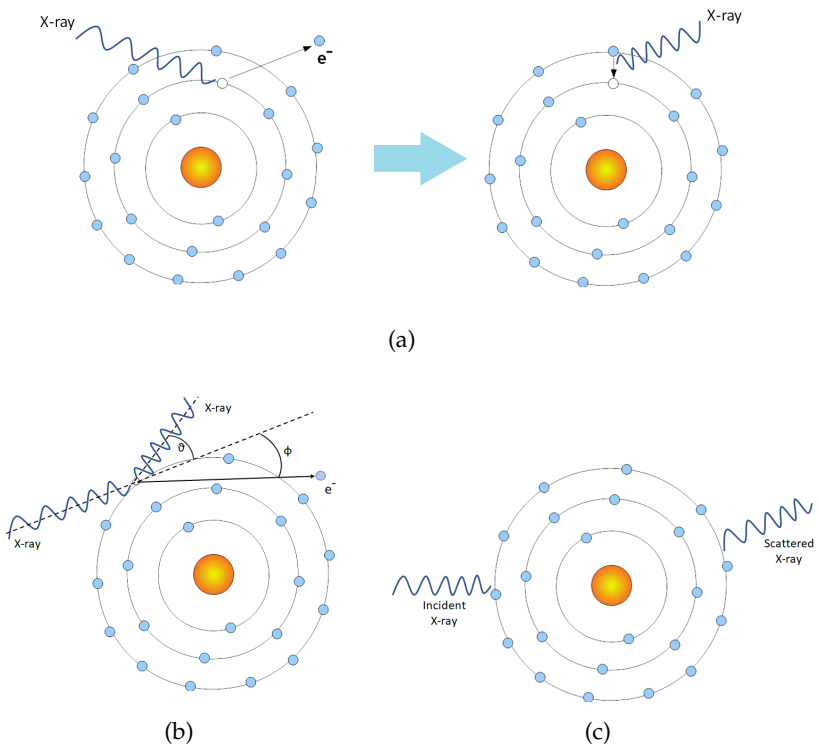

Figure 1.1: Interaction X-ray matter: (a) photoelectric absorption (left) with consequent fluorescence emission (right); (b) Compton scattering; (c) Rayleigh scattering.

sections of Rayleigh scattering (σ_R), photoelectric absorption (τ) and Compton scattering (σ_C). A detailed description of the mechanisms of interaction radiation-matter, here briefly introduced, can be found in various literature sources [4, 5, 6, 7]. Usually, the mass attenuation coefficient μ/ρ (cm^2/g) is reported instead of the linear attenuation coefficient. Accurate measurements for the mass attenuation coefficients of elements with $Z \leq 100$ are available in literature [8, 9, 10] as well as in computer-based data libraries [11, 12]. In this work, where necessary, the database for mass attenuation coefficients available at the U.S. National Institute of Standards and Technology (NIST) website [11] has been consulted.

The tabulated μ/ρ coefficients refer to pure elements of the periodic table. For materials made by mixtures/compounds of different elements, the mass attenuation coefficient can be calculated according to the mixture rule [13]:

$$\frac{\mu}{\rho}(E) = \sum_i \alpha_i \left(\frac{\mu}{\rho}\right)_i (E) \tag{1.2}$$

where α_i is the fraction by weight of the i^{th} atomic constituent of the compound/mixture. As an example, considering that the atomic mass of the two atoms of hydrogen approximately equals two atomic mass units ($u \approx 1.66054 \cdot 10^{-24}\ g$) and that the atom of oxygen has an atomic

mass of about 16 u, the mass attenuation coefficient of water (H_2O) following from eq. 1.2 is:

$$\left(\frac{\mu}{\rho}\right)_{H_2O}(E) \approx \frac{1}{9}\left(\frac{\mu}{\rho}\right)_{H}(E) + \frac{8}{9}\left(\frac{\mu}{\rho}\right)_{O}(E) \tag{1.3}$$

In Figure 1.2 are plotted a few mass attenuation coefficients for some elements/compounds in the range of energies of interest for medical imaging.

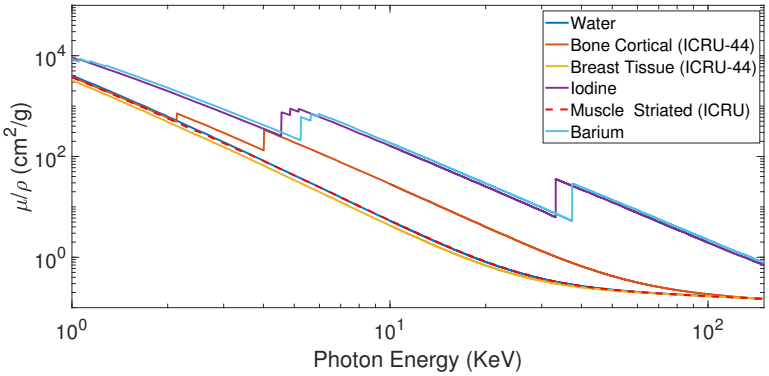

Figure 1.2: Mass attenuation coefficients for some elements/compounds of interest in medical imaging.

1.2 ATTENUATION OF X-RAYS THROUGH THE MATTER

The attenuation of X-ray radiation through the matter is described by the Lambert-Beer's law. Given an input X-ray beam, with intensity $W_0(E)$ at the energy E, crossing a homogeneous material with thickness ξ and with a linear attenuation coefficient μ, the Lambert-Beer's law calculates the transmitted intensity of the X-ray beam $W(E)$ as follows:

$$W(E) = W_0(E) \cdot e^{-\mu(E)\ \xi} \tag{1.4}$$

In the more general case the sample is a spatial distribution of linear attenuation coefficients $\mu = \mu(\bar{r})$ so that, along the X-ray path, different materials with different thicknesses are crossed by the incident X-ray beam. Moreover, a polychromatic spectrum $W(E)$ is employed. In this case, eq. 1.4 can be rewritten as follows:

$$\int_E W(E)\ dE = \int_E W_0(E) \cdot e^{-\int_\xi \mu(\bar{r},E)\ d\bar{r}} \tag{1.5}$$

where $\int_\xi \mu(\bar{r},E)\ \bar{r}$ is the line integral of the distribution of the linear attenuation coefficient along the direction ξ. In the monochromatic case $W(E) = \delta(E - E_0)$, therefore eq. 1.5 is simplified as follows:

$$W(E_0) = W_0(E_0) \cdot e^{-\int_\xi \mu(\bar{r},E_0)\ d\bar{r}} \tag{1.6}$$

1.3 ENERGY RESPONSIVITY OF X-RAY DETECTORS

In the practical case, X-ray images are produced by X-ray detectors. Such devices can operate in different ways, but essentially they convert X-ray radiation into an amount of charges proportional to the energy of the detected X-ray photon. The charges are therefore collected at the pixels and processed to produce a digital image. Essentially there are two main architectures to process such signals: charge integrating and photon counting. In the first family, each pixel integrates the charge collected in a fixed exposure time. Thus, the signal recorded is proportional to the total energy released in the pixel in the exposure time. In the second family, each X-ray quantum is counted, thus providing a direct measure of the incident number of X-rays.

To mathematically describe the signals recorded by a generic X-ray detector from an input X-ray beam, it is useful to introduce the concept of energy responsivity $\epsilon(E)$ [14]. This function $\epsilon(E)$ yields the relative signal output generated by an X-ray photon with energy E for a given X-ray detector. Therefore, when imaging an input X-ray beam $W(E)$, for each pixel (x, y) the signals recorded in the images $I(x, y)$ by the X-ray detector are described by the following expression:

$$I(x, y) = W(E) \cdot \epsilon(E) \tag{1.7}$$

The parameter $\epsilon(E)$ depends on the physical characteristics of the detector and on its architecture. As an example, for an ideal photon counting device with 100% detection efficiency, $\epsilon(E) = 1$ since each photon is counted once. For an ideal charge integrating detector that records signals proportional to the energy E of the incident X-ray quanta, often $\epsilon(E) \approx E$ is assumed. In real cases, summarizing the processes involved in the formation of the digital signals recorded by the X-ray detector, the responsivity is a complex function of the energy that can be experimentally measured with monochromatic radiation at synchrotron sources or simulated with Monte Carlo models simulating the characteristics of the actual detector.

1.4 DIGITAL RADIOGRAPHY

Radiography is the simplest X-ray imaging technique producing 2D images of the sample. In this application the images are recorded by a digital imaging system as a 2D matrix of signals. In practice, to produce a radiographic projection two images are acquired. The first is the image of the sample $I(x, y)$ recording, for each position (x, y), the transmitted beam $\int W(E, x, y) \cdot \epsilon(E)\, dE$; the second is the image of the beam (i.e. obtained without any sample) also called flat-field image that records the input X-ray flux, i.e. $I_{flat}(x, y) =$

$\int W_0(E,x,y) \cdot \epsilon(E)\ dE$. The two images are therefore processed as follows:

$$P(x,y) = -\log \frac{I(x,y)}{I_{flat}(x,y)} \tag{1.8}$$

With this process, higher values of $P(x,y)$ (i.e. brighter gray levels) are recorded in correspondence of the most absorbing objects, while low values are recorded along weakly absorbing objects (darker gray levels).

To better understand the physical meaning of the signals recorded in digital radiography, it is useful to introduce the concept of radiographic projection. In the monochromatic case, referring to the eq. 1.6, the radiographic projection directly reproduces the inversion of the Lambert-Beer's law:

$$P(x,y) = -\log \frac{W(E_0)}{W_0(E_0)} = \int_{\xi} \mu(E,\bar{r})\ d\bar{r} \tag{1.9}$$

In the polychromatic case, the equation for radiographic projection is more complex due to the energy dependence of both the spectrum and the linear attenuation coefficient:

$$P(x,y) = -\log \frac{\int W(E) \cdot \epsilon(E) \cdot e^{-\int_{\xi} \mu(E,\bar{r})\ d\bar{r}} dE}{\int W(E) \cdot \epsilon(E)\ dE} \tag{1.10}$$

By introducing the spectral weighting factor

$$\boldsymbol{w}(E) = \frac{W(E) \cdot \epsilon(E)}{\int W(E) \cdot \epsilon(E)\ dE} \tag{1.11}$$

eq. 1.10 can be rewritten as follows:

$$P(x,y) = -\log \int \boldsymbol{w}(E) \cdot e^{-\int_{\xi} \mu(E,\bar{r})\ d\bar{r}} dE \tag{1.12}$$

In the Linear Radon approximation described in [14] and summarized in Appendix A, eq. 1.10 can be approximated by the following expression:

$$P(x,y) \approx \int_{\xi} \bar{\mu}(\bar{r})\ d\bar{r} \tag{1.13}$$

where the quantity:

$$\bar{\mu}(\bar{r}) = \int \boldsymbol{w}(E) \cdot \mu(E,\bar{r})\ dE \tag{1.14}$$

is called spectral weighted linear attenuation coefficient.

Formally, the two equations for the radiographic projection 1.9 and 1.13 are equivalent, with the only difference consisting in the physical meaning of the linear attenuation coefficients: the monochromatic case considers the actual linear attenuation coefficient $\mu(E,\bar{r})$; the polychromatic case considers the spectral weighted linear attenuation coefficient $\bar{\mu}(\bar{r})$.

1.5 COMPUTED TOMOGRAPHY

Computed Tomography (CT) is an imaging technique that, from a series of 2D X-ray images collected at different angles source-object, reconstructs the 3D distribution of the attenuation coefficients $\mu(\bar{r})$ of which a sample is made. Being a 3D imaging technique, CT removes the overlaps of different anatomical structures that hamper the diagnostic power of the 2D radiographic technique.

Defining the sample to be imaged as 3D mathematical function of the space $O(\bar{r})$, the basic idea of CT technique shown in Figure 1.3 can be summarized as follows:

- **Tomographic scan**: multiple X-ray projections $P_\varphi(x, y)$ of the sample are collected under different angles source-detector (φ).
- **Radon transform**: the collection of the captured projections as a function of φ produces the so-called sinogram $S(x, y, \varphi)$. This mathematical transform is better known as Radon transform of the object: $S(x, y, \varphi) = \mathscr{R}\{O(\bar{r})\}$.
- **CT reconstruction**: the sinogram of the image is processed by a reconstruction algorithm that reconstructs the sample $O(\bar{r})$ by performing the inverse of the Radon transform ($\mathscr{R}^{-1}$): $O(\bar{r}) = \mathscr{R}^{-1}\{\mathscr{R}\{O(\bar{r})\}\}$

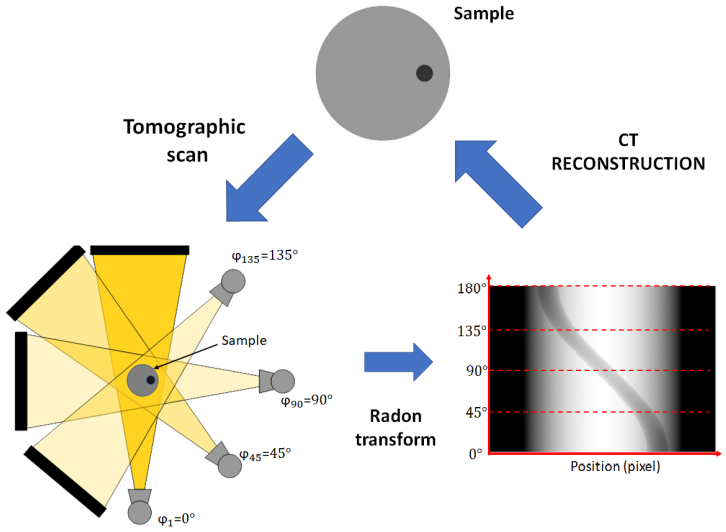

Figure 1.3: Workflow of CT: (top) sample; (bottom left) tomographic scan; (bottom right) Radon transform; (top) CT reconstruction.

The acquisition geometries for a CT scanner are shown in Figure 1.4. For each geometry, specifically designed reconstruction algorithms are implemented. That of reconstruction algorithms for CT is a very wide field and a description of such algorithms is beyond this work. Thorough descriptions of the most common reconstruction algorithms

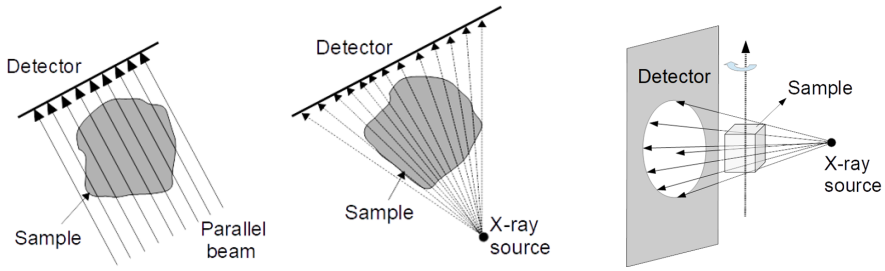

(a) (b) (c)

Figure 1.4: Acquisition geometries implemented by CT scanners: (a) parallel beam (b) fan beam (c) cone beam.

can be found in [6] and in [15]. The simplest and most common reconstruction algorithm is the Filtered Back-Projection (FBP). Specific implementations of FBP are available for each CT geometry. For the particular case of cone-beam geometry a modified version of the FBP has been implemented by (Feldkamp, Davis, and Kress [16]). In this case, the implementation of the FBP algorithm is often identified by the acronym Feldkamp, Davis and Kress (FDK).

The unit elements of a CT image are called voxels. In the monochromatic case, a voxel $V(\bar{r})$ directly measures the linear attenuation coefficient:

$$V(\bar{r}) = \mu(\bar{r}) \tag{1.15}$$

where the coordinate $(\bar{r})$ identifies the position of the voxel V in the 3D CT image. In the polychromatic case, considering the Linear Radon approximation, each voxel reconstructs a spectral weighted linear attenuation coefficient defined by eq 1.14:

$$V(\bar{r}) = \bar{\mu}(\bar{r}) = \int \boldsymbol{w}(E) \cdot \mu(E, \bar{r})\, dE \tag{1.16}$$

In contrast with radiography, CT imaging provides a direct measure of the linear attenuation coefficients $\mu(\bar{r}_i)$ (or $\bar{\mu}(\bar{r})$ in the polychromatic case) of which the sample is made. This feature makes of CT a quantitative technique.

2

X-RAY SPECTRAL IMAGING

X-ray imaging reproduces the internal morphology of a sample by providing a measure of the linear attenuation coefficients of which the sample is made. This means that materials with different chemical composition but similar attenuation coefficients are not distinguished by conventional X-ray imaging.

As shown in sect 1.1, the linear (or mass) attenuation coefficient of a specific element, compound or mixture is a function of the energy of the X-ray beam. Spectral imaging is a branch of X-ray imaging that aims at improving the knowledge about the sample by exploiting the different energy dependence of the linear attenuation coefficients shown by different materials.

The general application of spectral X-ray imaging requires the acquisition of information about the energy-dependent properties of the sample by imaging the sample with at least two different X-ray energies or two different X-ray spectra in the polychromatic case. The relative spectral algorithms have two main objectives: the first is that of allowing an improved separation between two materials that have similar gray levels in the conventional approach; the second is to provide quantitative information about the chemical composition of the sample.

In the clinical practice spectral imaging is performed to improve the diagnostic power of images for specific exams. As an example, in angiography usually an opaque iodine-based contrast agent is employed to increase the contrast of blood vessels. However, in the conventional approach the signal of the iodine solution can result to be close to the signals produced by vascular calcifications. Spectral techniques are employed to separate the iodine solution from the calcium plaques, thus allowing a proper diagnosis [17, 18]. In medical imaging, spectral techniques find many applications such as e.g. the separation of bone and soft tissues [19], the mapping of the inhaled xenon in the imaging of lungs [20], and the the detection of uric acid in kidney stones [21].

This section focuses on the particular application of spectral imaging called KES. The relative spectral algorithms and the most relevant concept designs of setups for this application are presented.

2.1 K-EDGE SUBTRACTION IMAGING

KES imaging is an X-ray spectral technique that exploits the strong increase in the absorption coefficients at the K-Edge of bio-compatible

elements embeddable in injectable pharmaceuticals called contrast agents. The common K-edge elements employed for clinical applications are iodine, barium, xenon and gadolinium. In recent years, also gold and silver nanoparticles are gaining some interest especially for theranostics applications, where both imaging and therapy are aimed to be performed at the same time. Usually, a contrast agent is a water-based solution which the main ingredient is a more or less complex molecule embedding the K-edge element of interest.

The ideal application of this imaging technique requires the acquisition of two images of the sample (either radiographic or CT) with two monochromatic energies, one below (E_1) and one above (E_2) the K-edge of the target contrast medium. Alternatively, KES imaging can be performed with two polychromatic X-ray beams with mean energies below and above the target K-edge.

Considering that in general the attenuation coefficients $\mu(E)$ are deceasing functions of the energy, in this approach only in the regions containing the K-edge element realize the condition $\mu(E_2) > \mu(E_1)$. This information can be exploited by a spectral algorithm to localize and quantify the concentrations of contrast agent within the sample.

2.2 ALGORITHMS FOR K-EDGE IMAGING

2.2.1 *Image subtraction*

The simplest and straightforward approach to perform KES imaging consists in the subtraction of the two images of the sample acquired at the energies E_1 and E_2, respectively below and above the target K-edge energy. The result of this subtraction is called KES image. The signals recorded by radiographic and CT KES images can be described by the following equations:

$$\begin{cases} P_{KES}(x,y) = \int_{\bar{\zeta}} [\mu(E_2,\bar{r}) - \mu(E_1,\bar{r})]\, d\bar{r}, & \textit{Radiography} \\ V_{KES}(\bar{r}) = \mu(E_2,\bar{r}) - \mu(E_1,\bar{r}), & CT \end{cases} \tag{2.1}$$

Of note, by considering the spectral weighted linear attenuation coefficients $\bar{\mu}(\bar{r})$, eq. 2.1 is valid also for the polychromatic case.

Due to the particular condition $\mu(E_2,\bar{r}_i) > \mu(E_1,\bar{r}_i)$ occurring only for the K-edge material, in KES images only the distribution of the contrast medium has a positive signal. This signal, called KES signal, is a function of the concentration α of the K-edge element in the contrast agent. A theoretical derivation of KES-CT signal as a function of α is reported in Appendix B.

For both radiographic and CT images, the KES technique allows localizing the contrast agent within the sample. Moreover, for CT images it is also possible to achieve quantitative information about the concentrations of the segmented contrast agent. A theoretical formula

to convert KES-CT images into maps of density concentrations of the K-edge element is hereafter reported.

Quantitative distribution of contrast agent from KES signal

In the most frequent applications the K-edge element is distributed in a homogeneous background material. Therefore, the reconstructed linear attenuation coefficients result from a mixture/compound of two main materials. As an example, when injected in the patient, a contrast agent solution diluted in blood can be described as a mixture of the K-edge element (e.g. Iodine, Barium) and water. For the particular case of inhaled Xenon, a compound of lungs and Xenon can be considered in the calculations for the KES signal.

For two elements/materials, the mixture rule can be written as follows:

$$\frac{\mu}{\rho}(E) = \alpha \cdot \frac{\mu_k}{\rho_k}(E) + (1-\alpha)\frac{\mu_b}{\rho_b}(E) \tag{2.2}$$

where α is the relative weight of the K-edge element in the background material, $\{\bar{\mu}_k, \bar{\mu}_b, \rho_k, \rho_b\}$ are respectively the attenuation coefficients and the densities of the K-edge element and the background material. Moreover, the density of a compound made by two elements is defined by the following rule:

$$\rho = \frac{\rho_k \rho_b}{\alpha\rho_b + (1-\alpha)\rho_k} \tag{2.3}$$

By coupling eq. 2.2 and 2.3 and omitting simple mathematical calculations, the KES signal recorded by each single voxel of a CT image can be written as follows:

$$V_{KES} = \frac{\rho_k \rho_b}{\alpha\rho_b + (1-\alpha)\rho_k}\left(\alpha \cdot \frac{\Delta\mu_k}{\rho_k} + (1-\alpha)\frac{\Delta\mu_b}{\rho_b}\right) \tag{2.4}$$

with $\Delta\mu_k = \mu_k(E_2) - \mu_k(E_1)$ and $\Delta\mu_b = \mu_b(E_2) - \mu_b(E_1)$.

The physical meaning of eq. 2.4 is that the KES signal of a CT image is a function of the relative weight α of the K-edge element located in a voxel. The solution for α of eq. 2.4 is the following:

$$\alpha = \frac{\rho_k(V_{KES} - \Delta\mu_b)}{(\rho_k - \rho_b)V_{KES} + \rho_b\rho_k(\frac{\Delta\mu_k}{\rho_k} - \frac{\Delta\mu_b}{\rho_b})} \tag{2.5}$$

The density (ρ_i) of the K-edge element contained in the i^{th} voxel is finally described by the following expression:

$$\rho_i = \frac{\alpha \cdot \rho_k}{\alpha \cdot \rho_b + (1-\alpha)\rho_k} \tag{2.6}$$

2.2.2 *Basis material decomposition*

A diffused and reliable approach that yields quantitative information about the sample from spectral imaging acquisitions is provided by

the Basis Material Decomposition (BMD) algorithm, first proposed in 1976 by Alvarez and Macovski [22].

The underlying idea of BMD algorithm is to consider that the ground truth of the scanned object can be written as a combination of basis functions representing a set of absorbing materials/elements:

$$\mu(E,\bar{r}) = \sum_{i}^{N} a_i \boldsymbol{f}_i \tag{2.7}$$

where a_i are characterization values of the N bases employed to describe the absorption material.

By choosing as set of basis the mass attenuation coefficients $\boldsymbol{f} = \mu/\rho(E)$, eq. 2.7 describes the mixture rule [13]:

$$\mu(E,\bar{r}) = \sum_{i} \rho_i \left(\frac{\mu}{\rho}\right)_i (E) \tag{2.8}$$

where the parameters $a_i = \rho_i$ represent the densities (or the concentrations) of the material described by the i^{th} basis material/element.

With the parameterization of eq. 2.8, eq. 1.9 for a planar projection can be rewritten as follows:

$$P = \sum_{i} \left(\frac{\mu}{\rho}\right)_i (E) \cdot \rho_i \xi_i \tag{2.9}$$

were ρ_i and ξ_i are respectively the density and the equivalent thickness of the i^{th} material/element parameterized.

In the simplest spectral implementation, two radiographic projections of the sample P_1 and P_2 (or two sets of tomographic projections) are acquired at two different energies E_1 and E_2 (or two spectra with different mean energies in the polychromatic case). In this case, the two radiographic projections can be exploited to solve (pixel by pixel) the following system of equations:

$$\begin{pmatrix} P_1 \\ P_2 \end{pmatrix} = \begin{pmatrix} \left(\frac{\mu}{\rho}\right)_1 (E_1) & \left(\frac{\mu}{\rho}\right)_2 (E_1) \\ \left(\frac{\mu}{\rho}\right)_1 (E_2) & \left(\frac{\mu}{\rho}\right)_2 (E_2) \end{pmatrix} \cdot \begin{pmatrix} \rho_1 \xi_1 \\ \rho_2 \xi_2 \end{pmatrix} \tag{2.10}$$

By calling $\boldsymbol{M}$ the matrix of the mass attenuation coefficients:

$$\boldsymbol{M} = \begin{pmatrix} \left(\frac{\mu}{\rho}\right)_1 (E_1) & \left(\frac{\mu}{\rho}\right)_2 (E_1) \\ \left(\frac{\mu}{\rho}\right)_1 (E_2) & \left(\frac{\mu}{\rho}\right)_2 (E_2) \end{pmatrix}. \tag{2.11}$$

the solution of eq. 2.10 for the parameters $\rho_i \xi_i$ can be obtained by computing the inverse matrix $\boldsymbol{M}^{-1}$. This inversion can be performed with numerical linear least squares approaches [23, 24]. Customizable functions to solve least squares problems are available in different programming platforms such as Matlab (the Mathworks, Natick MA)

and Python. Formally, the solution of eq. 2.10 can be written as follows:

$$\begin{pmatrix} \rho_1\xi_1 \\ \rho_2\xi_2 \end{pmatrix} = \boldsymbol{M}^{-1} \cdot \begin{pmatrix} P_1 \\ P_2 \end{pmatrix} \tag{2.12}$$

To avoid negative solutions for $\rho_i\xi_i$, non negative constrains [25] can be also considered in the least squares problem solution.

The BMD method can be extended to the case of n projections acquired at N different energies:

$$\begin{pmatrix} \rho_1\xi_1 \\ \vdots \\ \rho_m\xi_m \end{pmatrix} = \boldsymbol{M}^{-1} \cdot \begin{pmatrix} P_1 \\ \vdots \\ P_n \end{pmatrix} \tag{2.13}$$

In this general case, $\boldsymbol{M}$ is a $m \times n$ matrix where n is the number of energies and m the number of bases selected to describe the sample. A unique solution for $\rho_i\xi_i$ can be obtained if the condition $m \leq n$ is met. This means that the number of bases used to decompose the sample must be equal or less than the number of energies used to image the sample.

By applying the BMD algorithm, 2D images reproducing (pixel by pixel) the maps of $\rho_i\xi_i$ are produced for each selected basis. For CT imaging, the BMD algorithm can be applied to each tomographic projection prior to CT reconstruction. The resulting CT images directly reproduce the 3D map of densities ρ_i for each basis.

For the particular application of KES imaging, usually water and the K-edge element(s) are selected as bases in the BMD algorithm. Focusing on KES technique, both the image subtraction and the BMD algorithm take advantage from the K-edge jump. Therefore, regardless of the algorithm employed, the energies and the acquisition system must be optimized to maximize the detectability of the KES signal.

More generally, the BMD algorithm can be extended to other applications. As an example, by selecting bone and water as bases, the BMD algorithm can be employed to separate soft tissues from bones.

2.3 ACQUISITION SYSTEMS FOR SPECTRAL IMAGING

Spectral imaging applications basically require the acquisition of multiple images of a sample with different energies (or spectra). In this section, the main setups designed for multiple energy acquisitions are described.

2.3.1 *Separate energy acquisition*

The simplest acquisition scheme is that of acquiring images of the sample at different energies in different acquisitions (or CT scans). This

straightforward approach requires the use of a source (with settable energies) and an X-ray detector (Figure 2.1)

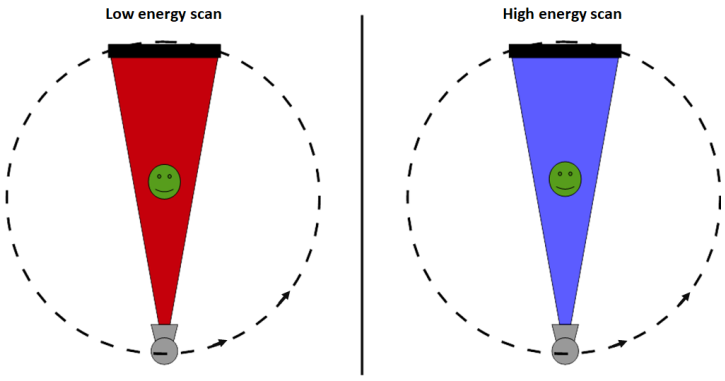

Figure 2.1: Example of separate scan for spectral imaging.

This approach is usually performed at synchrotron sources where it is possible to set monochromatic beams with fluence rates suitable for X-ray imaging. In particular, for KES imaging the use of two monochromatic X-ray beams with energies just below and above the target K-edge allows for the detection of very subtle concentrations of a known K-edge element [26] and brings the experimental KES performances close to the theoretical limits in terms of image quality [27].

The limitations of the approach above described are clearly deducible. In fact, especially for in-vivo applications, motion artifacts due to the misregistration of the images acquired at different times in two different acquisitions hamper the application of spectral algorithms that require perfectly co-registered images of the sample at different energies.

The growing interest for spectral imaging applications for both clinical and research purposes has led to the development of acquisition systems specifically designed to allow the simultaneous acquisition of the sample at different energies. The main solutions developed to achieve this goal are hereafter presented.

2.3.2 *Dual energy commercial systems*

The main system designs for clinical spectral imaging are based on acquisitions with two polychromatic spectra. Though such systems are not properly focused on the KES technique, they are suitable for imaging with contrast agents by implementing specifically designed versions of the BMD algorithm. The main solutions implemented by commercial CT scanners to minimize the acquisition time and the influence of motion artifacts in spectral images are described in the following sections.

Rapid kV switching

The rapid kV switching system design was first introduced in 1986 by Kalender et al. [28] and then adopted by GE Healthcare for the production of dual energy CT scanners [29]. In this system the kV settings of the X-ray tube are rapidly switched among two values (usually 80 kV and 140 kV) during the CT scan. With this acquisition scheme, two subsequent CT projections refer respectively to two different energy contents. The images are then co-registered and processed with a spectral algorithm. A schematic of this system is shown in Figure 2.2.

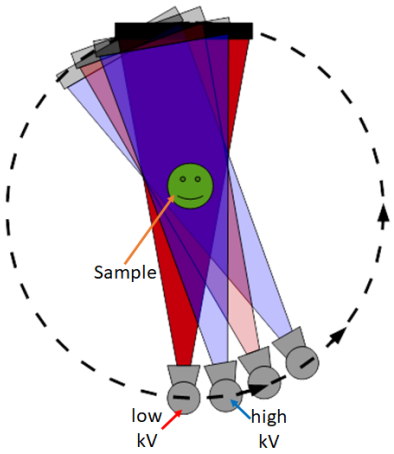

Figure 2.2: Schematic of CT scanner implementing the rapid kV switching procedure.

The rapid kV switching method presents some disadvantages. The main issue is due to the fact that the current technology of X-ray tubes does not allow a current switching while performing a rapid kV switching. This technical limitation has consequences for both the dose and the image quality achievable. In fact, to match the noise between the low and high energy images, the exposure time of low energy image (80 kV) must be about three times higher than the high energy image exposure. Other disadvantages are the co-registration of the low and high images that can induce motion artifacts and the limited switching time that slightly increases the acquisition time of this system if compared to a conventional (non spectral) CT scanner.

Dual source CT scanner

Dual source CT scanner (DSCT) is a commercial system produced by Siemens Healthcare that implements two couples X-ray source-detector mounted with an angular offset of 90 *degrees* operating independently [30]. During the CT acquisition the two X-ray tubes operate with different kV settings. Typical settings for this setup are (80 kVp; 140 kVp) and (100 kVp; 140 kVp). A schematic of DSCT system is shown in Figure 2.3.

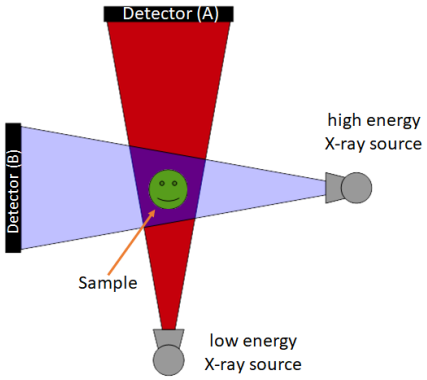

Figure 2.3: Schematic of dual source CT scanner.

DSCT system allows the simultaneous collection of two sets of CT projections with low and high energy contents suitable for spectral applications. Moreover, in contrast with the rapid kV switching, the use of two independent X-ray sources allows a proper calibration of the currents to optimize the dose and the achievable image quality.

The main disadvantages of DSCT system arise from its design. The first issue is due to the possibility that the scattered radiation from source A is detected by the detector B (cross-scattering). Cross scattering can both induce artifacts and reduce the suitable Signal to Noise Ratio (SNR) of the reconstructed images. Another limitation of this system is due to the 90 degrees offset. In fact, since the two sets of images need to be co-registered, motion artifacts can occur especially when imaging rapidly moving organs [14].

Dual layer detector system

A detector-based solution for dual energy imaging has been implemented by Philips Healthcare [31]. This system implements a dual layer detector made by superimposing two scintillation detectors as shown in Figure 2.4.

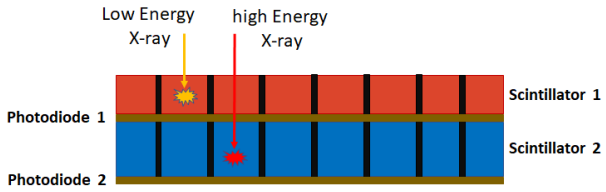

Figure 2.4: Schematic of dual layer detectors.

In these detectors, the first layer is optimized to detect low energy photons while to bottom layer detects the remaining high energy photons. Therefore, two images with different energy contents are produced by the two different layers. For the Philips Healthcare systems, the top layer scintillator is a yttrium-based garnet; the bottom

layer scintillator is gadolinium-oxysulphide (GOS) [31]. Other typical scintillators used in the top layer with different thicknesses are: GOS, CsI, ZnSe, BGO, LSO [14].

Dual layer detectors simplify the design concept of dual energy scanners. In particular, the implementation of a dual layer detector in a common CT scanner enables spectral imaging techniques in a single acquisition with a single couple source/detector.

The main limitation to this technique is represented by the limited energy resolution achieved by dual layer detectors. In particular, low energy photons detected by the bottom layer or high energy photons detected by the top layer can induce an energy contamination that can reduce the spectral separation between the low energy and high energy images. The energy separation and the imaging performance depend on the types and thicknesses of the scintillator layers. Another limitation for dual layer detectors is the limited spatial resolution due to the two different scintillator layers.

2.3.3 *State-of-the-art acquisition systems for K-edge imaging*

This section presents two different acquisition systems specifically designed for KES imaging, but extensible to other spectral techniques. The main advantages of such systems, subject of this thesis work, are: (i) the ability of acquiring simultaneous images of a sample at different energies; (ii) the possibility to properly tune the energy content of the images according to specific K-edge element; (iii) the use of a single couple source-detector that simplifies the design of the acquisition setup.

Spectral imaging with energy sensitive XPCDs

The development of direct detection spectral XPCDs is revitalizing the interest for spectral imaging applications [32].

The attractiveness of detector-based spectral setups is the possibility of acquiring multiple images with different energy content in a single shot. However, if compared with dual layer detectors, direct detection spectral XPCDs mounting high-Z sensors present numerous advantages: (i) the photon counting architecture totally remove the electronic noise; (ii) the direct detection (i.e. the absence of scintillators) allows for improved spatial resolution and high detection efficiency; (iii) by implementing two (or more) settable energy thresholds, the energy content of each image can be properly selected by the user.

The main advantage of setups implementing energy resolving XPCDs is the possibility of performing spectral imaging with common X-ray tubes [14, 33, 34], thus encouraging the development of the technique with portable devices that look at the daily clinical practice. Moreover, the single shot nature allows for a fast and reliable detection of the contrast medium by totally removing motion artifacts.

For the specific case of KES imaging, an XPCD implementing at least two energy thresholds allows imaging the sample at two properly set energy bins with mean energies below and above the target K-edge in a single acquisition. A schematic of KES imaging with an XPCD implementing two thresholds is shown in Figure 2.5.

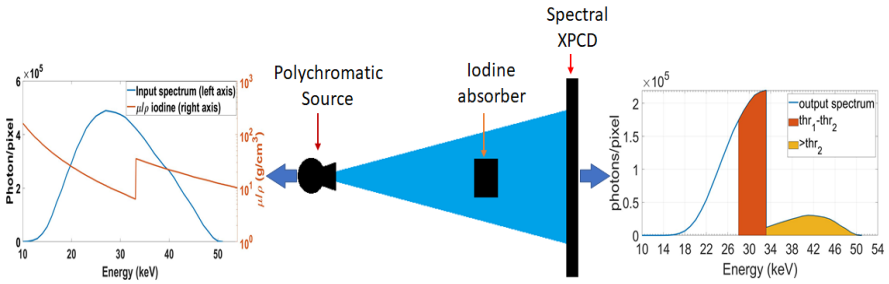

Figure 2.5: Example of KES imaging for an iodine-based contrast agent with an XPCD implementing two thresholds.

Whereas spectral imaging with XPCDs is considered very promising, at present its practical application is mainly limited to the imaging of small animals due to the small detection areas (few cm^2) available by the state-of-the-art detection modules [35]. Another limiting factor to spectral imaging with XPCDs is represented by the charge sharing issue [32] that can affect the energy resolution, the spatial resolution, and the detection efficiency of such detectors [36, 37, 38, 39, 40].

In recent years, XPCDs implementing solutions to cope with the charge sharing issue, such as e.g. medipix-3 and Pixirad/pixie-iii, have been introduced in the market [41, 42, 43, 44]. By correcting for the charge sharing issue, such XPCDs allow achieving improved energy resolutions and detection efficiencies suitable for spectral imaging. A thorough description of spectral XPCDs, charge-sharing issue and related hardware/algorithmic solutions, as well as a complete characterization of the Pixirad/Pixie-iii XPCD is reported in chapter 3.

The effort made in recent years by XPCD manufacturers has been that of increasing the active area, the number of thresholds and the achievable energy resolution. If the minimum feature to perform spectral imaging with XPCDs is the implementation of two thresholds, an increased number of thresholds allows a more detailed spectral separation, thus increasing the spectral information obtainable from the sample. Among the manufactured XPCDs that can implement more than two thresholds it is worth to cite the medipix-3 chip. In principle this chip has 2 thresholds/counters in each 55×55 μm^2 pixel. However, by connecting the chip to a sensor matrix with a pitch of 110 μm it is possible to group 4 pixels together. In this configuration, up to 8 thresholds/counters are available in a pixel area of 110×110 μm^2.

Setups for X-ray spectral imaging with XPCDs implementing two thresholds and the charge-sharing correction have been successfully

tested within the medipix and the KEST collaborations using respectively medipix3 and Pixirad/Pixie-iii detection systems [45, 46, 47, 48, 49, 50].

The results achieved in the framework of the KEST collaboration are presented in Chapter 4.

Spectral imaging with Bent-Laue monochromators

An alternative and interesting approach for KES imaging at synchrotron sources is to prepare a specifically designed setup by using bent-Laue monochromators. In particular, by exploiting the properties of monochromator crystals and the focusing bent-Laue geometry it is possible to focus a polychromatic X-ray beam with limited energy dispersion ΔE around the target K-edge energy. With this setup, the polychromatic beam is focused at the sample and then diverges at the detection position. As result, each image collects an ideal row of the sample at different energies enabling spectral imaging applications [51, 52, 53, 54, 55]. In bent-Laue setups for KES imaging the sample must be scanned at the focus to have 2D images.

The two main setups for KES imaging with bent-Laue crystals are shown in Figure 2.6.

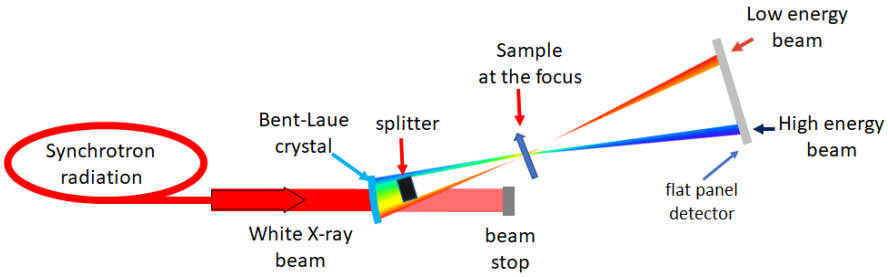

(a)

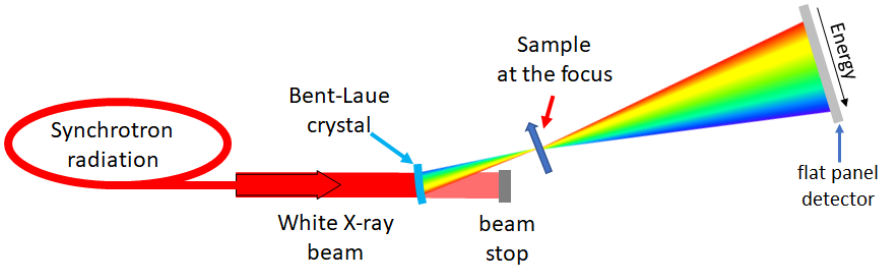

(b)

Figure 2.6: Setups for KES imaging with bent-Laue crystals: (a) double beam KES setup; (b) spectral-KES setup.

Figure 2.6 (a) shows a first setup, called dual-beam KES, implemented at the ID17 beamline of the European Synchrotron Radiation Facility (ESRF) Facility (Grenoble, France). This setup exploits a Si(1,1,1) crystal and a splitter to prepare a dual energy beam, with energies

below and above the K-edge energy of iodine [51]. Due to the poor energy dispersive properties of the bent-Laue crystal employed in this setup, a significant fraction of the beam (about 1/3) is involved in the crossing of the energies around the target K-edge. This fraction of beam is not suitable for KES technique, therefore it must be removed by using a beam stopper called splitter.

The second setup (Figure 2.6 b), called spectral-KES setup, was implemented by prof. D. Chapman's group at the Biomedical imaging and Therapy (BMIT) beamline of the Canadian Light Source (CLS) [54], Saskatoon (Canada). This setup does not require the use of a splitter. The key feature of the proposed approach is to exploit the energy focusing properties of asymmetrically cut Si crystals to retain a fine energy resolution while producing a wide energy bandwidth.

The spectral-KES setup, has been demonstrated to be suitable for simultaneous KES imaging of multiple K-edge contrast agents [55]. Moreover, the high energy dispersive properties of this setup were also exploited by Qi et al. [56] for fast X-ray absorption spectroscopy (XAS) imaging.

The main advantage of the spectral-KES is the possibility to acquire simultaneously a row of the sample with finely sampled multiple energies crossing one or more K-edge of interest. The data acquired with this setup can be therefore processed with the BMD algorithm in its general formulation with more than two bases [55].

The main limitation to spectral imaging with bent-Laue crystals arises from the modality of scanning the sample at the focus that allows acquiring only one ideal row at a time. Another limitation arising from the scan at the focus is the so-called crossover artifact that can impair the suitability of the images [57, 58, 59]. This artifact is generated by the fact that since the sample is unavoidably extended over the focus, the multiple monochromatic laminar beams at different energies cross the sample at different angles, thus referring to slightly different line integrals. Under these conditions, when applying the KES subtraction or the BMD spectral algorithm the slight mismatch between the line integrals generates the crossover artifact resulting into artificial shadows with a derivative-like contrast (positive/negative) along the direction of the scan in correspondence of high absorbing features of the sample. A thorough characterization of the crossover artifacts as well as a model-based algorithmic solution to cope with this issue can be found in [57]. Solutions to achieve artifact-free images by scanning the sample out from the focus are at present under investigation by the Author in collaboration with prof. Chapman's group at the BMIT beamline of CLS.

The focusing properties of a specific asymmetrically cut Si crystal change with the energy. Therefore, for each target K-edge a specifically cut crystal with proper asymmetry angle must be implemented in the bent-Laue geometry. With the aim of further developing the technique

for KES imaging in collaboration with prof. Chapman's group, the INFN funded a three year project called KISS. The collaboration aims at extending the technique also to non-conventional contrast agents based on silver and gold nanoparticles. A setup for spectral-KES imaging with bent-Laue crystals has been implemented within the KISS project at the SYRMEP beamline of Elettra synchrotron (Trieste, Italy). The first experimental results achieved within the KISS project are presented in Chapter 5.

3

PIXIRAD-1/PIXIE-III XPCD: DESCRIPTION AND CHARACTERIZATION

3.1 INTRODUCTION TO ENERGY SENSITIVE XPCDS

Large area direct detection X-ray Photon Counting Detectors (XPCD) are of great interest in medical imaging [60, 32] thanks to their high detection efficiency and low intrinsic noise, which allow overcoming the main limitations of the charge integrating devices. These imaging detectors are nowadays available with pixel sizes in the range of 50-70 microns; all these characteristics make them suitable for a broad range of applications, from material science to biomedicine. For instance, XPCDs are attractive for low dose imaging applications; and they have been already employed in mammography and breast computed tomography in both commercial systems [61, 62] and experimental setups [63, 64].

Hybrid architecture

The basic design principle of an XPCD is the so-called 'hybrid architecture' (see Figure 3.1). In this architecture, pixelated thick semiconductor sensors are coupled with the Application Specific Integrated Circuit (ASIC). Both components are separately fabricated and then, electrically connected, generally, with micro-bumps. The main advantage of this design is that the same ASIC can be coupled with different sensor materials (such as, e.g. Si, Ge, CdTe, CdZnTe crystals). This architecture enables manufacturers to provide detection systems optimized in a specific manner for the intended application.

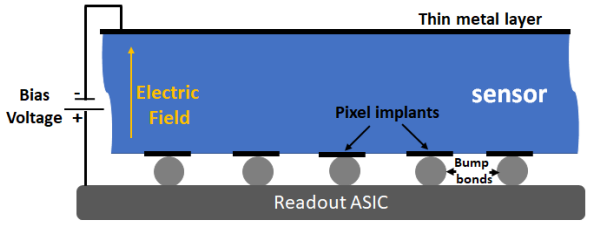

Figure 3.1: Sketch of hybrid architecture photon counting detectors.

Operating mode of hybrid XPCDs

The operating mode of a hybrid XPCD can be summarized as follows: (i) the sensor is biased, an electric field is applied to the sensor and the system is ready for photon detection; (ii) the incoming X-ray photon interacts with the sensor releasing a number of electron-hole pairs (Fig. 3.2 (a)) that is proportional to the energy deposited by each single interaction (e.g. photoelectric, Compton); (iii) the carriers drift and diffuse towards the electrodes inducing a current signal collected by the pixels implemented in the ASIC (Fig. 3.2 (b)); (iv) each

pixel implements a threshold discriminator system (Fig. 3.2 (c)) that properly shapes the output signal and compare it to one (or more) threshold value(s) (Fig. 3.2 (d)). Whenever the signal exceeds the threshold level, the counter corresponding to the selected threshold is increased by one. The stages (i), (ii), (iii) and (iv) are schematized in Figure 3.2.

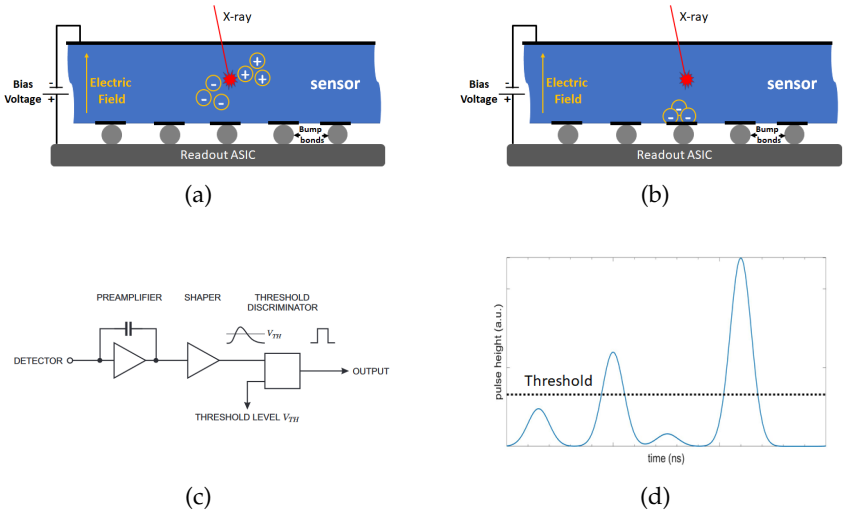

Figure 3.2: Operating mode of hybrid XPCDs: (a) the interacting photon releases holes electron pairs; (b) electron (or holes) collection at pixels; (c) example of threshold discriminator system [65]; (d) example of threshold discrimination process.

Energy thresholds

By implementing one or more programmable energy thresholds, an XPCD is able to remove the electronic noise and to discriminate the incoming photons according to their energy. This feature makes XPCDs suitable also for spectral imaging applications with polychromatic sources. In particular, XPCDs implementing two (or more) energy thresholds and two (or more) counters are enabled to acquire perfectly registered images over multiple energy bins in a single scan.

Charge Sharing effect

In the detection process, while drifting towards the electrodes the charges unavoidably diffuse. Therefore, it can happen that the charge cloud produced by a single event spreads over multiple pixels (Figure 3.3). This effect, called 'charge sharing', occurs for each combination of sensor material and thickness, but it is enhanced when the thickness-to-pixel size ratio increases.

single pixel mode

In the simplest acquisition mode, usually called single pixel mode (or pixel mode), the pixels work independently from their neighbors and the collected charge by each single pixel is treated as an independent event. Several works [36, 66, 37, 40, 38, 39, 67, 68] showed how this acquisition mode is affected by the charge sharing effect which can induce multiple counts from a single interacting photon and can impair the spectral resolution, the spatial resolution, and the detection efficiency.

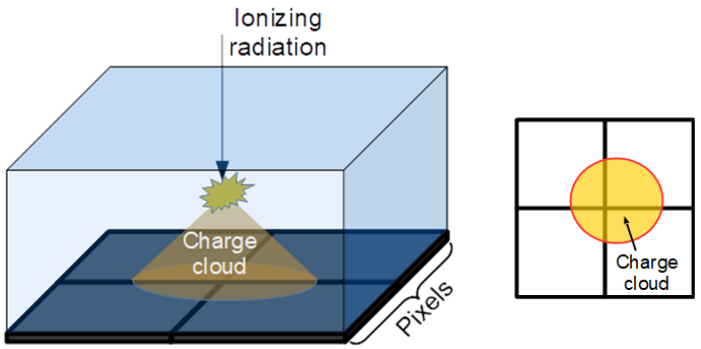

(a) (b)

Figure 3.3: Sketch of Charge sharing effect: (a) lateral view; (b) top view.

At least for monochromatic photons, the problem of multiple counts and the degradation of the spatial resolution can be partially or totally removed by properly tuning the discrimination threshold (*thr*). As an example, for photons with energy E, quadruple, triple and double counts induced by the charge sharing issue can be removed by setting respectively $thr > E/4$; $thr > E/3$; $thr > E/2$. However, the removal of multiple counts by thresholding firstly can induce a loss of efficiency and secondly it does not solve the degradation of the energy resolution. Different solutions have been proposed to correct for the charge-sharing effect. Solutions proposed in literature include (i) the change of the pixel geometry, e.g. using hexagonal pixels instead of square pixels [69]; (ii) the reduction of the charge collection time by operating with high bias voltages [70]; and (iii) the implementation of specifically designed algorithms for charge sharing suppression in the readout systems [69, 71, 72, 73, 35, 74]. These algorithms trace back the energy deposited by a single photon by summing the charge collected in a cluster of (3 up to 8) pixels and assigning the hit to the pixel receiving the highest fraction of the total charge [75, 76, 69]. This latter solution, usually called charge-summing algorithm, is of particular interest since it allows a proper evaluation of the energy deposited by each single event while keeping a small pixel side. This mode has been implemented in several readout chips such as e.g. the medipix-3 [77], the Pixie-iii [72], the X-Counter PC [78] and the AGH Fermilab chip [79].

Charge sharing correction

Charge Summing algorithm

3.2 THE PIXIRAD-1/PIXIE-III PHOTON COUNTING DETECTOR

Pixirad-1/Pixie-iii is a hybrid XPCD made by coupling, with the flip-chip bonding technique, a high Z sensor with an application specific integrated circuit (ASIC) [72]. The sensor is a Schottky type diode array made of a 650 μm thick CdTe semiconductor with electron collection on the pixels. For each pixel, the readout has two 15-bit counters fed

by two independent discriminators with settable energy thresholds. Pixie-iii is a CMOS ASIC with an active area of $3.17 \times 2.49\ cm^2$ covered by a 512×402 matrix of square pixels with $62\ \mu m$ pitch.

The Pixie-iii ASIC implements three acquisition modes, two of which specifically designed to correct for the charge sharing issue:

- Pixel Mode (PM): each pixel counts independently from the others.
- Neighbor Pixel Inhibit mode (NPI) mode: only one counter per event is enabled. When the charge cloud spreads over multiple pixels, the NPI mode assigns the count to the pixel receiving the highest fraction of the total charge. This mode solves the problem of multiple counts and preserves the spatial resolution, however it does not fix the loss in spectral resolution due to the charge-sharing.
- Neighbor Pixel Inhibit and SUmming Mode (NPISUM) mode: the total energy of one event involving up to 4 neighboring pixels is evaluated by summing the signals collected by these 4 pixels. The recovered charge is converted into voltage and then discriminated against the threshold to assign the hit to a unique pixel, i.e. the one receiving the highest fraction of the total charge.

With high detection efficiency and a frame rate larger than $500\ fps$, Pixirad/pixie-iii is suitable for X-ray in vivo microtomography [80, 81]. Moreover, by implementing two energy thresholds and the charge summing algorithm (NPISUM mode) this system is particularly suitable for spectral imaging with polychromatic sources [48, 49].

3.2.1 *CdTe sensor crystal*

Thanks to its high detection efficiency and thickness, the CdTe sensor mounted in the Pixirad-1/pixie-iii XPCD allows performing spectral imaging at the K-edge energy of a wide range of elements employed in medical imaging from Silver (K-edge energy 25.52 keV) to Gadolinium (K-edge energy 50.24 keV). However, despite its attractive characteristics, the CdTe material sensor can affect both the spatial and spectral resolution achievable by the XPCD. In fact, in addition to charge sharing, when energies above Cd or Te K-edges ($E_{K(Cd)} = 26.7\ keV$ and $E_{K(Te)} = 31.8\ keV$) are employed, a characteristic X-ray emission (fluorescence) of Cd and Te can occur.

Being isotropically emitted, fluorescence photons may:

1. Be absorbed by the same pixel in which the primary interaction occurs (Fig. 3.4 a).

2. Be detected by another pixel potentially inducing multiple counts from fluorescence and affecting both the spatial and spectral resolution (Fig. 3.4 b).

3. Leave the sensor completely affecting the detection efficiency and the spectral resolution (Fig. 3.4 c).

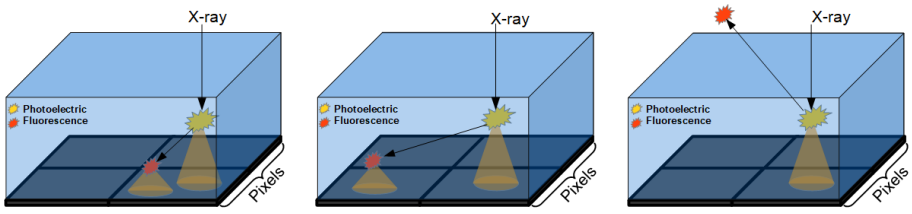

(a) (b) (c)

Figure 3.4: The primary interaction and the fluorescence are detected by (a) the same pixel; (b) different pixels. (c) the fluorescence photon escapes from the sensor and it is not detected.

The energies of the main transitions (i.e. fluorescence photons) emitted by Cd and Te are $E_{Cd} = 23.1\ KeV$ and $E_{Te} = 27.4\ KeV$. The mean free paths, in CdTe, of these photons are respectively of $\lambda_{Cd} = 124.4\ \mu m$ and $\lambda_{Te} = 61.6\ \mu m$. Of note, the higher energy Te fluorescence photon has a lower mean free path due to its proximity to the Cd K-edge.

When using a monochromatic beam of energy E above Cd or Te K-edges, fluorescence photons can interact far from the point in which the primary interaction occurs. Since the mean free path of both Cd and Te characteristic X-rays is greater than or equal to the size of individual pixels, three different cases can occur:

1. the energy E is released in the pixel where the photon interacts.

2. the energy $E - E_{Cd}$ is released in correspondence of the pixel where the primary interaction occurs, the energy E_{Cd} in a different pixel (Fig 3.4 b).

3. the energy $E - E_{Te}$ is released in correspondence of the pixel where the primary interaction occurs, the energy E_{Te} in a different pixel (Fig 3.4 c).

In the cases 2 and 3, fluorescence photons can also induce multiple counts that can affect the spatial and spectral resolution as well as the detection efficiency. When imaging with the NPISUM mode, if the pixels (in cases 2 and 3) belong to the cluster considered by the charge summing algorithm, the distortion in the detected spectrum induced by fluorescences can be partially corrected.

In general, the overall performance of this detection system are expected to differ for energies below and above Cd and Te K-edges.

Another limiting factor of CdTe sensor arises from local charge trapping effects due to impurities in the sensor crystalline structure [82, 83, 84]. As result, when the sensor is biased for several minutes, the images show dark/bright regions and stripes that can severely impair the suitability of the images [85]. To handle this unwanted effects, dedicated pre-processing procedures have been developed [85, 84]. In alternative, since these effects get worse with the increase of the acquisition time and become prominent after several seconds, this issue can be tackled by limiting the time in which the CdTe sensor is biased. For example, for applications requiring long acquisition times, dedicated acquisition protocols can be developed to acquire sequences of images where the bias of the CdTe sensor is periodically rebooted. Thus, in the fraction of time where the bias is turned off, the trapped charges within the sensor are released.

3.3 CHARACTERIZATION OF PIXIRAD/PIXIE-III WITH MONOCHROMATIC RADIATION

By allowing switching among different acquisition modes, Pixirad/Pixie-iii is an optimal device to test the performance of the charge summing algorithm (NPISUM mode) and to compare it with the basic pixel mode (PM mode). As described in the previous sections, multiple counts (detection or removal) and charge-sharing (level of correction) strongly influence the performance of a system in terms of spectral and spatial resolution, noise response, and detection efficiency. A comprehensive characterization of the acquisition modes implemented in the Pixie-iii ASIC has been carried out with monochromatic radiation at the ESRF Grenoble, France. During the acquisitions the detection system was cooled down to $-30\ ^{\circ}C$ and the CdTe crystal was biased with a working voltage of 400 V.

The linearity range of the three acquisition modes has been measured with monochromatic photons with energy 24 keV (below the Cd and Te K-edges).

The Energy resolution has been measured for four energies: 26 keV, 33 keV, 37 keV and 50 keV.

The characterization of the imaging features of the detection system has been carried out for two energies 26 keV and 33 keV (below and above the CdTe K-edges) by using the objective metrics for digital systems usually employed in medical imaging. In particular, the spatial resolution has been evaluated by means of the Line Spread Function (LSF) in the spatial domain and the presampling Modulation Transfer Function (MTF) in the frequency domain; the noise response has been evaluated in the frequency domain by using the Normalized Noise Power Spectrum (NNPS) [86, 87, 88].

Finally, for the two energies 26 keV and 33 keV, the imaging performance achieved by the different modes and with different discrimina-

tor thresholds have been compared by using the Signal to Noise ratio (SNR) and the Noise Equivalent number of Quanta (NEQ) as the figure of merit. Both metrics, SNR and NEQ, evaluate the signal to noise ratio respectively in the spatial and frequency domain and they are effective in objectively evaluating the overall image quality achievable by an imaging system under different conditions.

3.3.1 *X-ray source*

Data have been acquired at the biomedical beamline ID17 of ESRF. The source is a 21-pole wiggler, placed 150 m upstream of the detection system. The beam, monochromatized by a double Silicon-bent Laue crystal, has a quasi-parallel geometry with divergence < 1 $mrad$ and < 0.1 $mrad$ respectively along the horizontal and the vertical directions and can reach a maximum size of 150×10 mm^2 $(H \times V)$ [89]. The shape of the beam is flat along the horizontal direction and roughly Gaussian along the vertical direction.

At ID17, the beam can be shaped by three different remotely controlled slits systems installed at different distances from the source. For this characterization work the beam size has been chosen to cover the entire horizontal length of the detector; in the vertical direction, the slits have been opened to have a beam height of 6.6 mm at the detector position.

The storage ring worked in top up mode (injections every hour), with a 2.5% maximum current difference; during the acquisitions, the current of the ring has been constantly monitored. For a fixed energy, all the acquisitions have been performed with similar ring currents to limit variations of fluence rate below 1%.

3.3.2 *Image pre-processing*

Although the beam-shape does not affect the measurements of the linearity and of the spectral resolution, the evaluation of the image features (LSF, MTF, NNPS, SNR and NEQ measurement) must be carried out over homogeneous regions in the images. Therefore, the images must be corrected for the beam shape. The images devoted to the measurements of the image features have been thus corrected with the flat field procedure introduced in sect 1.4:

$$I_{corr}(x,y) = \frac{I(x,y)}{I_{flat}(x,y)} \tag{3.1}$$

This correction, in addition to being used to prepare radiographic projections for CT (eq. 1.8), is common to most X-ray imaging applications and serves to equalize the acquired images by removing systematic inhomogeneities and correcting for the beam shape. The

practical effects of this correction are shown in Figure 3.5 comparing both uncorrected and corrected images.

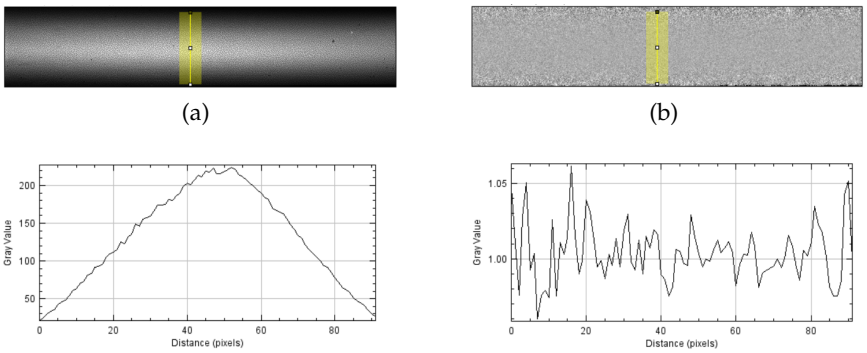

Figure 3.5: (a) image of the synchrotron beam, (c) vertical profile of the beam; (b) flat field corrected image, (d) vertical profile of corrected image.

As shown in Figure 3.5 (b), the effect of the flat-field correction is to flatten the shape of the X-ray beam and to correct the inhomogeneities of the gain of pixels, thus strongly reducing the systematic noise. However, this procedure unavoidably induces an increase of the stochastic noise that is defined as the standard deviation (σ) of the gray levels of the image evaluated in a homogeneous region. As an example, if the flat field image has the same statistics (i.e. the same gray levels and standard deviation) of the image to be corrected, the noise in the corrected image will be increased by a factor $\sqrt{2}$. To minimize the increase of the stochastic noise induced by the flat field correction, the flat field image $I_{flat}(x,y)$ must have a high statistics if compared to the image to be corrected. This can be achieved by averaging a set of N flat field images instead of using a single image:

$$I_{flat}(x,y) = \frac{1}{N}\sum_{k=1}^{N} I^{k}_{flat}(x,y) \tag{3.2}$$

Theoretically, considering a pure Gaussian noise and stationary conditions, the increase of the stochastic noise in the corrected images is a function of the number N of the frames $I^{k}_{flat}(x,y)$ used to create the flat-field image $I_{flat}(x,y)$ and it can be evaluated by propagating the noise from eq. 3.1. For the purposes of this work, for each combination of energies, thresholds and acquisition mode, the matrix employed for the flat field correction has been obtained by averaging 100 flat field frames $I^{k}_{flat}(x,y)$. In this case, the increase the stochastic noise of the corrected images is estimated to be roughly 0.5% and thus negligible.

As briefly discussed in sect. 3.2.1, for long acquisition times, detectors based on high Z crystal sensors (such as CdTe) show a systematic time-dependent inhomogeneous pixels gain and the the stationary

hypothesis is no longer valid. To overcome this limitation, in this work stationary conditions were approximated by limiting each acquisition to a maximum of 10 *s*.

3.3.3 *Linearity*

For an imaging system, the relationship between the input events and the recorded signal influences the maximum fluence rate over which the system can be suitable. The definition of 'input event' depends on the architecture of the imaging system. In the photon counting architecture, an event is the signal generated by an input photon and collected by the pixels.

In nearly all imaging systems, two different events must be separated by a minimum amount of time in order to be treated and recorded as two separate signals [4]. This time is usually called '*dead time*' and it is the minimum time required by the system to process a signal generated by a single event. For an XPCD, when two (or more) photons interact with the same pixel in a time shorter than the dead time, the signals generated by separate events merge into a single signal that will be treated as a single event. This phenomenon is called paralysis and it is illustrated in Figure 3.6. The bottom of the figure shows six randomly distributed events over the time; the center of the figure shows how the dead time windows triggered by separate input events can overlap; the top of the figure shows how the signals generated by different events can merge into a single signal becoming indistinguishable. When two or more dead time windows overlap the system is temporarily paralyzed and a loss of counts occurs.

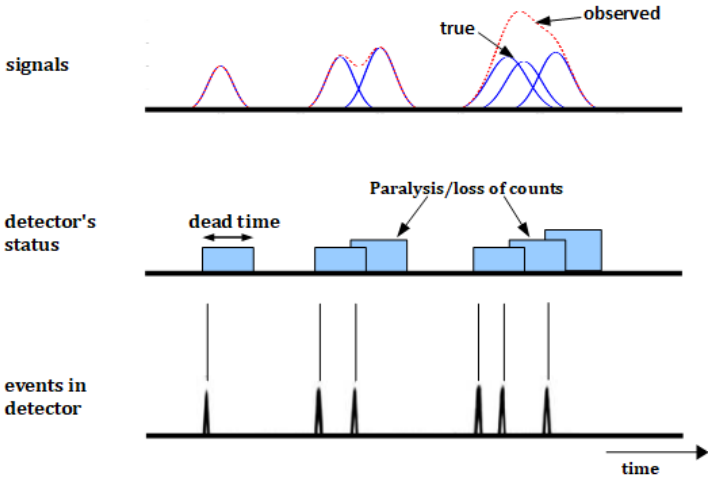

Figure 3.6: Illustration of the paralysis for an XPCD.

For a photon counting detector, with the increase of the photon fluence rate, three regimes can be observed (Figure 3.7):

- **Linear regime:** the recorded counts linearly increase with the increase of the input events.
- **Linearizable regime:** for higher fluence rates some counts are lost, but the number of counts still increases with the increase of the input events up to a maximum C_{max}, i.e. the maximum counts per pixel per second achievable by the system. In this range, the response of the system is linearizable and the system is still suitable for imaging.
- **Non-linearizable regime:** when the fluence rate is too high, the number of counts decreases with the increase of the input events due to a time-extended paralysis occurring in extended regions of the XPCD. The system is no longer suitable for imaging.

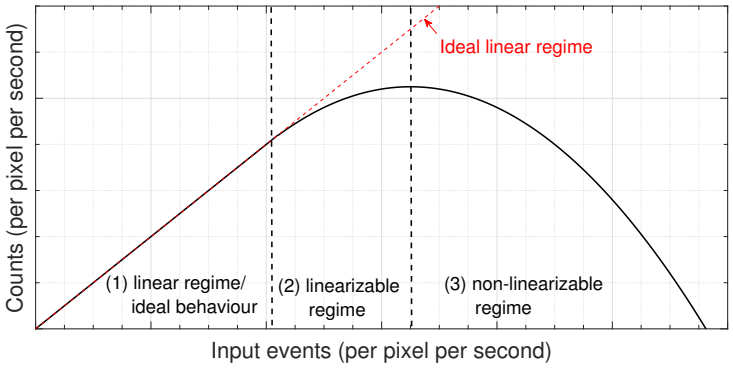

Figure 3.7: Plot of counts as a function of the input events for a paralyzable XPCD.

For the Pixirad-1/pixie-iii XPCD, linearity measurements have been performed with a monochromatic beam set to $E = 24\ keV$ and with $thr = 3\ keV$ using the method proposed in Delogu et al. [36]. Under these conditions, i.e. $E < 26.7\ keV$ (Cd K-edge) and $thr < E/4$, considering the high detection efficiency of the CdTe crystal (almost 100% at $E = 24\ keV$) all the input photons are expected to be detected and processed by all the acquisition modes implemented in the pixie-iii detection system. The method in [36] consist in acquiring sets of flat field images at different mean fluence rates. The vertical shape of the synchrotron beam (see Fig. 3.8, left panel) allows extracting from a single image the mean counts of the pixels in different rows, corresponding to different fluence rates. Since for high fluence rates the shape of the beam can be distorted due to the paralysis of the detection system, the actual shape of the beam is extracted from the images acquired with a low fluence rate, where the detector is supposed to work in linear regime. For the images where the beam shape is distorted, the number of input events is calculated by exploiting the fact that the beam shape does not change by increasing the fluence

rate. In particular, the number of input events is estimated by rescaling the actual shape of the monochromatic beam to the higher fluence rates.

In this analysis, for each mode and beam filtration, 100 images with an exposure time of 100 ms have been acquired and averaged to improve the statistics. To extend the range of the mean counts to the nonlinear range, the images were acquired with a few different aluminum filtration thicknesses (12.7, 5.7 and 0 $mmAl$). A quantitative analysis of the linearity has been performed by plotting, for each mode, the number of counts against the number of input events. To directly compare the results achieved by the different modes, for all the plots the number of input events per pixel per second employed as 'x' axis refer to the NPISUM mode. In the approximation of CdTe efficiency of 100%, this choice can be justified considering that the number of input events recorded by the NPISUM mode is expected to be very close to the actual number of impinging photons since, for construction, this mode does not record multiple counts from charge-sharing. For this analysis, the scale factor to estimate the number of input events at higher fluence rates (were the images of the beam are distorted by the high number of events to be processed) has been calculated by using the Lambert-Beer's law. In particular, the increase (in percentage) of the photon fluence rates expected for 0 and 5.7 $mmAl$ filtration has been calculated with respect of the maximum filtration 12.7 $mmAl$.

Figure 3.8 shows the flat field images acquired respectively with the PM, NPI and NPISUM modes with the lowest (left panel) and the highest (right panel) fluence rates corresponding respectively to 12.7 $mmAl$ and 0 $mmAl$ filtration. The low-flux images (Figures 3.8 a, e, i) allow defining the actual beam profile (Figures 3.8 c, g, k) that appears distorted in the high-flux ones (Figures 3.8 b, f, j).

The distorted beam profiles at high fluence rates (Figure 3.8, right panel) show that all modes are affected by the paralysis. However, as it is clear from the magnitude of the distortions induced in the images by high fluence rates, the NPISUM and the NPI modes are more prone to paralysis if compared to the PM mode.

Fig. 3.9 shows the counts per pixel per second as a function of the input events per pixel per second for PM, NPI and NPISUM modes. As reference, in Figure 3.9 are shown also the linear fits (of equation $p1 \cdot x$) limited to the low flux data. Since with the maximum flux the PM mode does not reach the paralysis, a quadratic fit (of equation $p1 \cdot x^2 + p2 \cdot x$) has been performed to extrapolate the maximum counts per pixel per second achievable ($C_{max} = -p2/(2 \cdot p1)$).

For the NPI and the NPISUM modes, the maximum counts per pixel per second achievable have been extrapolated directly on the plots. For all the modes, the maximum linearity range (L_{max}) has been roughly estimated considering the residuals plot between the linear fit and the experimental data. In particular, in the assumption that in the linearity

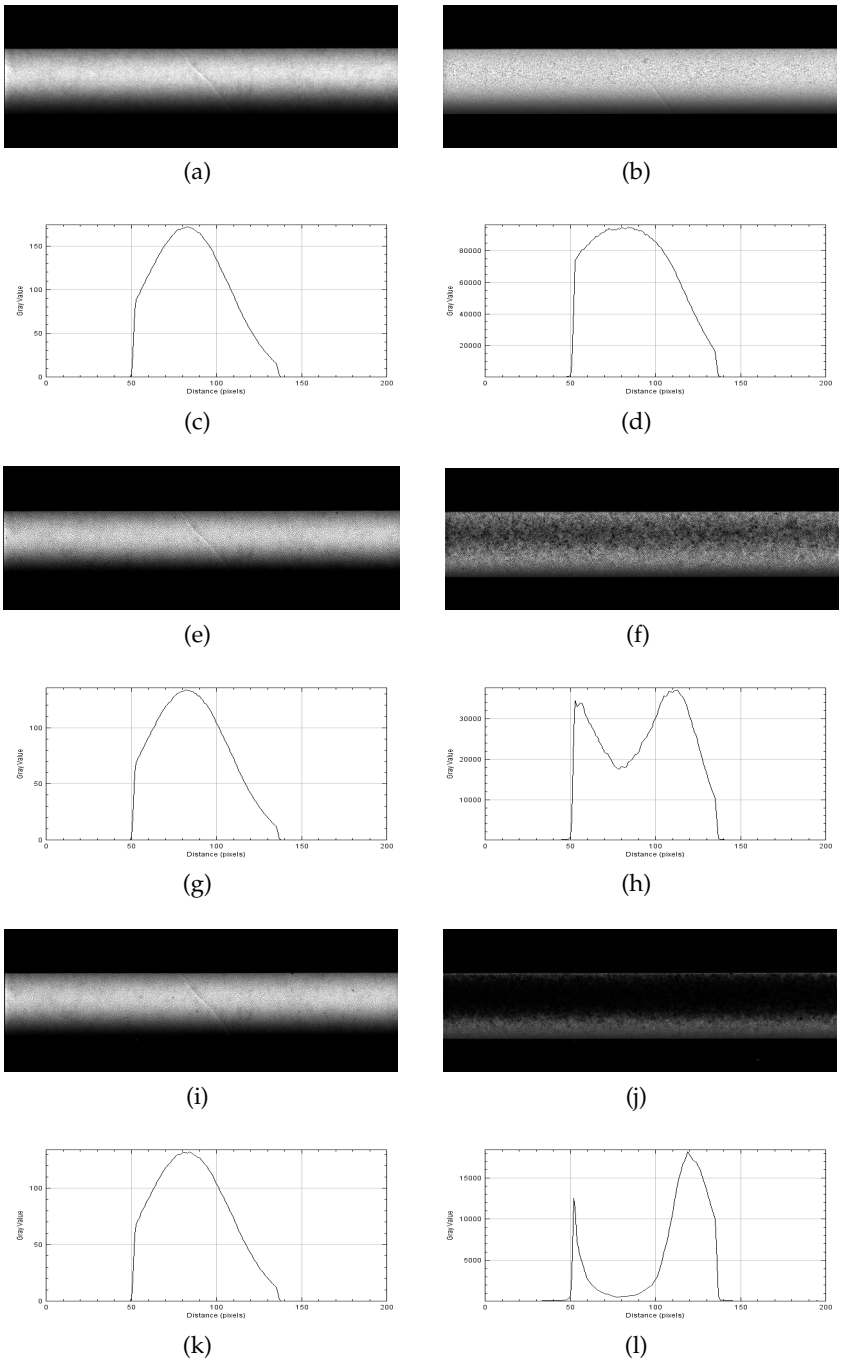

Figure 3.8: White field images and vertical profiles for 12.7 *mmAl* (left panel) and 0 *mmAl* (right panel). Top (a-d) PM mode; center (e-h) NPI mode; bottom (i-l) NPISUM mode.

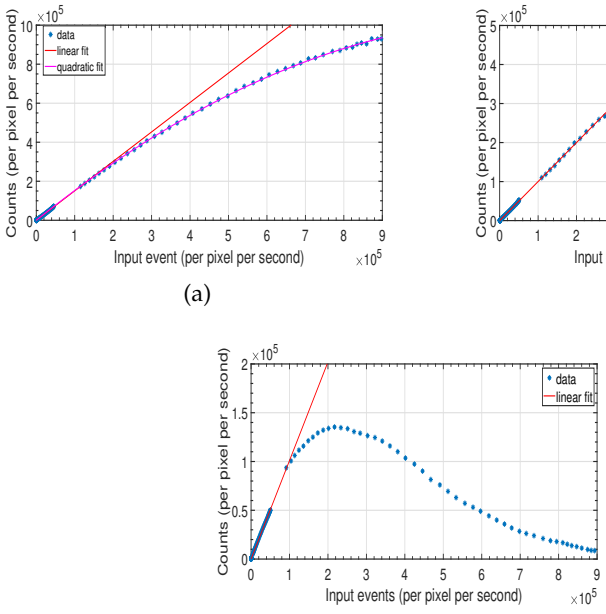

Figure 3.9: Plot of counts as a function of the input events for: (a) PM mode; (b) NPI mode; (c) NPISUM mode.

range the residuals are randomly distributed around the fit, L_{max} has been detected as that point above which the residuals systematically diverge (with increasing negative values in the case of study) from the fit. The linearity and the linearizable ranges are summarized in Table 3.1.

mode	L_{max} (input events/pixel/s)	C_{max} (input events/pixel/s)
PM	$2.0 \cdot 10^5$	$1.3 \cdot 10^6$
NPI	$2.9 \cdot 10^5$	$4.9 \cdot 10^5$
NPISUM	$1.0 \cdot 10^5$	$2.2 \cdot 10^5$

Table 3.1: Linearity and linearizable ranges (L_{max} and C_{max}) for PM, NPI and NPISUM modes.

Referring to the L_{max} in table 3.1, the linearity range of the PM mode is reduced if compared to the NPI mode. This behavior is due to the charge sharing effect. In fact, considering the same number of input events, when charge-sharing occurs the PM mode processes separately all the signals splitted over multiple pixels while the NPI mode processes only the highest signal in a cluster 2x2 pixels. The lowest linear range achieved by the NPISUM mode, instead, is due to the charge summing algorithm that increases the lengths and the heights of the signals to process, thus increasing the dead-time.

By comparing the C_{max} achievable (Table 3.1) it follows that the acquisition modes paralyze in the order NPISUM<NPI<PM. As explained

for the linearity, also in this case the lower C_{max} achieved by the NPISUM mode can be explained considering that the charge summing algorithm (implemented by the NPISUM mode) increases the height and the time-length of the reconstructed signals, thus increasing the dead-times. If compared to the PM mode, also the NPI mode, by selecting only the highest signals in a cluster of pixels increases the length of the dead time induced by each event.

Considering that the heights and the lengths of the signals increase with the energy of the input photons, for energies ≥ 24 keV the limits here reported must be considered as superior limits.

3.3.4 *Energy resolution*

The energy resolution is defined as the ratio between the Full Width Half Maximum (FWHM) of a peak in the differential spectrum and its energy [4]:

$$\frac{\Delta E}{E} = \frac{FWHM}{E} \tag{3.3}$$

The differential spectra have been obtained by acquiring and differentiating the integral spectra. These integral spectra have been recorded through a threshold scan, i.e. by moving the threshold thr at steps of 0.5 keV at fixed beam energy and fluence. For each value of thr, 50 images of the beam with an exposure time of 100 ms have been recorded and then summed. The integral spectrum has been obtained by plotting the average signal, measured in a fixed 450×30 $pixel$ Region Of Interest (ROI), against thr. The ROI has been chosen to take the biggest area avoiding dead/hot pixels and inhomogeneities of the beam. In particular, the height of the ROI was the FWHM of the vertical (broadly Gaussian) shape of the beam. This choice allowed to take into account only the most intense part of the beam excluding the inhomogeneities of the beam along the tails.

The measured energy resolution depends on the properties of the CdTe crystal, the source and the electronics. When measured over several pixels, as in this work, the energy resolution is further degraded by the slight offset of the thresholds implemented in different pixels [38].

The measurements have been performed for photons with energies close to the K-edges of the contrast agents of interest in KES imaging such as e.g. Ag (25.52 keV), I (33.17 keV), Xe (34.56 keV), Ba (37.44 keV) and Gd (50.24 keV), i.e. 26 keV, 33 keV, 37 keV and 50 keV. For each energy, the energy spread of the beam was estimated in 116 eV, 187 eV, 235 eV and 429 eV (combined energy spread given by the beam divergence and the intrinsic Darwin curve of the crystals) [89].

Figure 3.10 shows the differential spectra obtained with the monochromatic beam set to 26 keV, 33 keV, 37 keV and 50 keV.

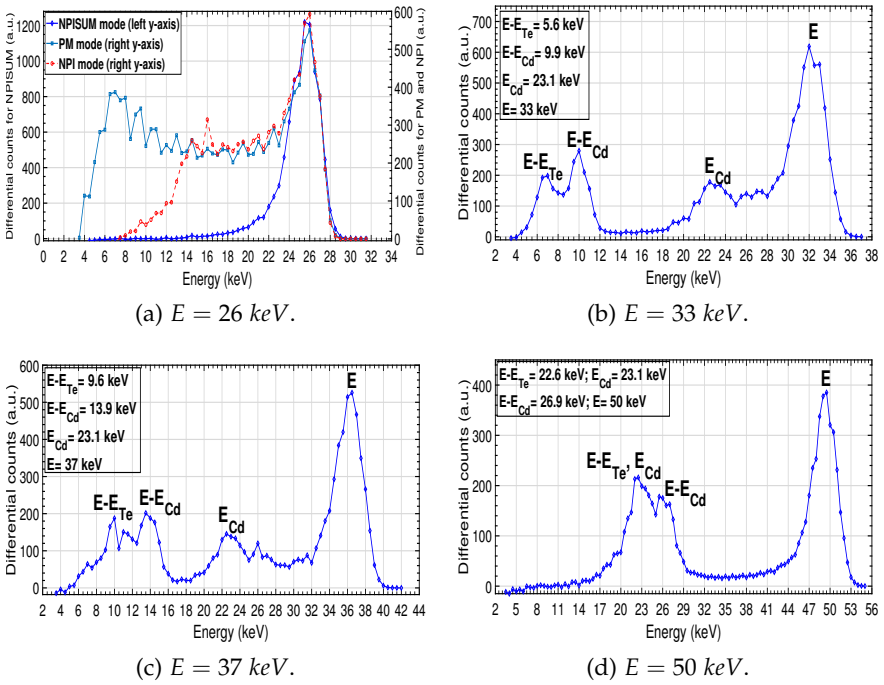

(a) $E = 26\ keV$. (b) $E = 33\ keV$.

(c) $E = 37\ keV$. (d) $E = 50\ keV$.

Figure 3.10: Differential spectra for: (a) $E = 26\ keV$ (PM and NPI right y axis; NPISUM left y axis); (b) $E = 33\ keV$ (NPISUM); (c) $E = 37\ keV$ (NPISUM); (d) $E = 50\ keV$ (NPISUM).

Figure 3.10 (a) shows that, for the beam energy $E = 26\ keV$ ($E < E_{K(Cd)}$), the spectra depend only on the acquisition modes as follows:

- **NPISUM** mode recovers the charge spread, no multiple counts are recorded and the differential spectrum shows only one peak corresponding to the energy of the impinging photons (i.e. the full energy peak). The comparison with PM and NPI modes shows that the NPISUM mode achieves the highest number of counts in the full energy peak. This means that, if compared to the other modes, NPISUM mode preserves the detection efficiency when a high threshold is set.

- **PM** mode does not remove multiple counts. The spectrum shows a not resolved full energy peak with a long left tail, according to [38].

- **NPI** mode removes multiple counts, but it does not recover the spread of the charge. This means that for $thr > E/2$ there is a loss of detection efficiency depending on the threshold value. As a consequence, the spectrum shows a not completely resolved full energy peak with asymmetric tails.

All the spectra in Figures 3.10 (b) (c) and (d), obtained using energies above the Cd and Te K-edges, show additional signals due to fluorescence and escape peaks corresponding to $E_{Cd} = 23.1\ keV$ and

E-E_{Cd}, E-E_{Te} respectively. The Te fluorescence photons do not produce a clearly visible signal in the differential spectra at $E_{Te} = 27.4\ keV$ because, having an energy just above the Cd K-edge, in CdTe they have a mean free path ($\lambda_{Te} = 61.6\ \mu m$) comparable with the pixel size. For this reason, the re-absorption of the Te fluorescence photon is highly probable within the same range in which charge sharing occurs and is corrected by the NPISUM mode.

Table 3.2 reports both the FWHM and the energy resolution for the NPISUM mode at all the beam energies here considered.

Energy (keV)	FWHM (keV)	$\Delta E/E$
26	3.4 ± 0.4	$(13 \pm 2)\%$
33	3.6 ± 0.4	$(11 \pm 1)\%$
37	3.7 ± 0.4	$(10 \pm 1)\%$
50	4.1 ± 0.4	$(8.2 \pm 0.8)\%$

Table 3.2: FWHM and energy resolution measured on the full energy peak.

3.3.5 *Spatial resolution*

The presampling LSFs have been measured by using the slanted edge method [90, 91, 92]. This method consists in the acquisition of images of a thick absorber with a sharp edge placed near the detection system and slanted by a small angle with respect to the pixels; the digital images of the edge are then processed to obtain the presampling Edge Spread Function (ESF), whose derivative is the presampling LSF (see Figure 3.11).

The presampling MTF has been obtained from the 1D FFT (Fast Fourier Transform) of the LSF. All the MTF have been normalized to 1 at MTF(0).

To study the dependence of the spatial resolution on the threshold, the latter has been scanned at steps of 2 keV; this operation has been repeated for each of the three acquisition modes. For each value of the threshold, 100 images of a slanted edge were acquired and averaged.

The performance under the different conditions have been studied in both the spatial and the frequency domains by plotting respectively the FWHM of the LSF and the MTF 50% (i.e. the frequency for which MTF $= 0.5$) against *thr*.

Figure 3.12 shows the plots of the FWHM of the presampling LSFs and MTF 50% against the threshold *thr* for the beam energy $E = 26\ keV$.

The results can be summarized as follows:

- NPISUM mode: no multiple counts are recorded; both the FWHM and *the*MTF 50% are almost independent from the applied *thr*.

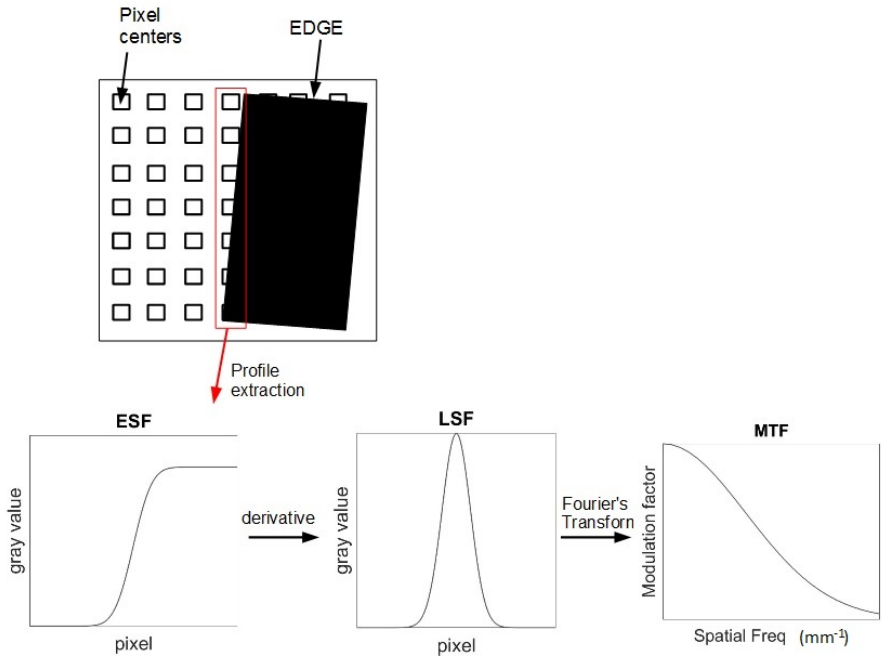

Figure 3.11: Diagram of the slanted edge method for LSF and MTF measurements. The procedure is described in the main text.

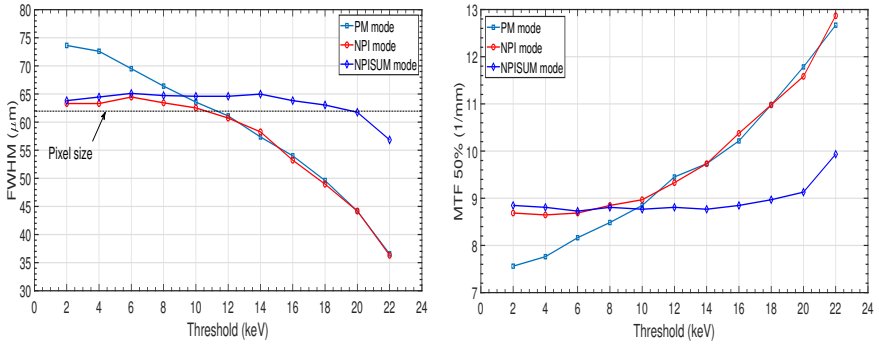

(a) (b)

Figure 3.12: $E = 26keV$: (a) plot of FWHM of the Line Spread Function against the threshold; (b) MTF 50% against the threshold.

Moreover, the FWHM of the LSF has a size of 64 μm, comparable with that of the pixel pitch 62 μm.

- PM mode: the spatial resolution improves by increasing *thr*; the FWHM and MTF 50% respectively decreases and increases with *thr*. In particular for $thr < E/2$ the FWHM is larger than the pixel size, for $thr > E/2$ there is a reduction of the effective pixel size that improves the spatial resolution in agreement with [93], [68] and [36].

- NPI mode: for $thr < E/2$, thanks to the removal of multiple counts the NPI mode shows the same behavior of the NPISUM

mode. For $thr > E/2$ the spatial resolution improves as observed for the PM mode.

Figure 3.13 shows the plots of the FWHM of the presampling LSFs and of MTF 50% against the threshold thr for the beam energy $E = 33\ keV$.

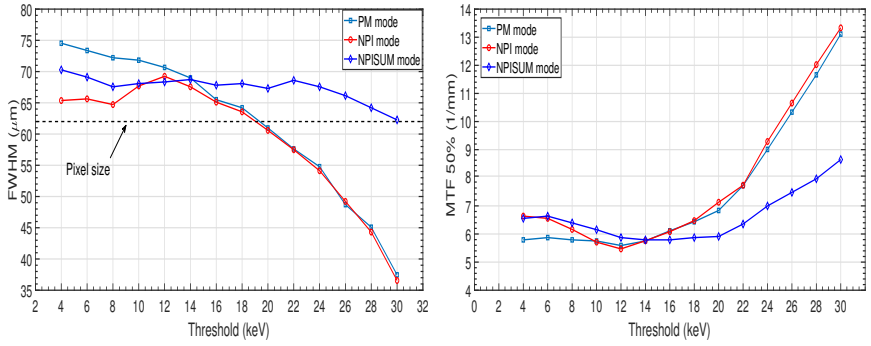

(a) (b)

Figure 3.13: $E = 33keV$: (a) plot of FWHM of the Line Spread Function against the threshold; (b) MTF 50% against the threshold.

Referring to Figure 3.13, the behavior of the acquisition modes can be described as follows:

- the NPISUM mode shows almost constant FWHM and MTF 50% values up to $thr \leq E_{Cd}$. For $thr > E_{Cd}$ the fluorescence photons are totally removed inducing an improvement of the spatial resolution. In particular, with respect of $thr = 22\ keV$, the MTF 50% increases from a minimum of 10% ($thr = 24\ keV$) to a maximum of 36% ($thr = 30\ keV$).

- in PM mode the spatial resolution improves with the increase of thr. In particular, for $thr < E/2$ the PM mode has a lower spatial resolution if compared to the NPISUM mode. For $thr > E/2$ the FWHM decreases to values below the true aperture of 62 μm, in agreement with the behavior at 26 keV.

- the NPI mode shows roughly the same performance of the NPISUM mode for $thr < E/2$ and the same performance of PM mode for $thr > E/2$.

Figure 3.14 compares the presampling MTF obtained with PM and NPISUM modes coupled with two representative thresholds (one below and one above E/2) for the two energies (a) 26 keV and (b) 33 keV.

In Figure 3.14, the Nyquist frequency (f_{Ny}) and the aperture function have been represented as reference. The aperture function is given by $|sinc(\pi \cdot u \cdot \Delta x)|$ and it is the Fourier transform of the ideal aperture for a square pixel with side Δx. By comparing Figures 3.14 (a) and (b), it appears clear how, at fixed threshold, the MTF values measured

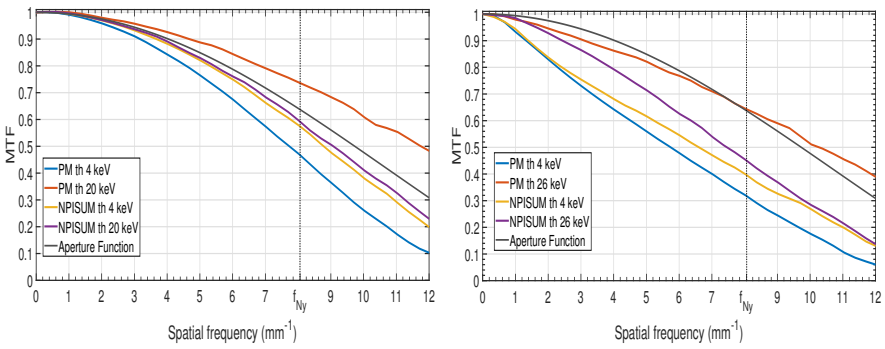

(a) (b)

Figure 3.14: Comparison of MTFs response for the two energies (a) 26 keV and (b) 33 keV for PM and NPISUM modes and different thresholds.

with $E = 33\ keV$ are lower than those measured with $E = 26\ keV$. This worsening of the spatial resolution involves both the PM and the NPISUM modes and it is due to Cd-emitted fluorescence photons that, having a mean free path of $\lambda_{Cd} = 124\ \mu m$ in CdTe, play a major role in the spatial resolution degradation if compared to the effects due to charge sharing.

Figure 3.14 shows also that for each combination of acquisition mode, energy and thresholds the MTF extends above the Nyquist frequency. This means that the system is always undersampled.

3.3.6 *Normalized Noise Power Spectrum (NNPS)*

The NNPS is the decomposition of the variance measured over a homogeneous region of the image (i.e. σ^2). This function measures the noise texture and gives useful information about the frequency components of the noise in a digital image [86, 87].

The algorithm to measure the NNPS in digital images is the following [87]:

$$NNPS(u,v) = \frac{\Delta x \Delta y}{N_x N_y M} \sum_{i=1}^{M} \frac{|FFT_{2D}(I_i(x,y) - \bar{I}_i)|^2}{\bar{Q}^2} \tag{3.4}$$

where u and v are the horizontal and vertical axes of the frequency domain, $I_i(x,y)$ is the *i-th* sub ROI, $\bar{I}_i$ the average signal of the *i-th* sub-ROI, $\bar{Q}^2$ the square of the average recorded signal, M the total number of ROIs, Δx, Δy the pixel sides and N_x, N_y the number of pixels of the ROI along horizontal and vertical directions.

In this work, the NNPS has been determined by analyzing the flat field images acquired with threshold scans as done for the measurement of the spatial resolution. For the 2D NNPS, 1600 (59×59 *pixel*) sub-ROIs were acquired. Such ROIs overlap for half of their area horizontally.

The uncertainty of each data point of the $NNPS(u,v)$ has been quantified as the standard deviation of the average of the M realizations used for the measure of the NNPS with the eq. (3.4).

The NNPS describes the correlation between different pixels allowing to study the cross-talk induced by multiple counts in neighboring pixels. In particular, the correlations between neighboring pixels act as a low-pass filter that shapes the high frequency components of the NNPS [93]. Thus, the NNPS magnitude is expected to decrease with the increase of the frequency when a bigger fraction of multiple counts is recorded.

Since the data points of the 2D NNPS along the axes ($u = 0\ mm^{-1}$ and $v = 0\ mm^{-1}$) can have higher values which are not representative of the stochastic noise [87], the 1D NNPS has been evaluated from the measured $NNPS(u,v)$ omitting the axes. The 1D NNPSs profiles were extracted from the 2D NNPS by adapting the procedure explained by the IEC-62220-1 [94] to our experimental conditions. In particular, horizontal and vertical 1D NNPSs profiles were obtained by averaging the data points from one row just above and below the axes $v = 0\ mm^{-1}$ ($NNPS_x$) and $u = 0\ mm^{-1}$ ($NNPS_y$). Each data point of $NNPS_x$ and $NNPS_y$ was associated with the frequency $f = \sqrt{u^2 + v^2}$. Finally, the two profiles $NNPS_x$ and $NNPS_y$ were averaged to obtain a smoothed 1D NNPS profile.

The plots of 1D NNPS for monochromatic photons at $E = 26\ keV$ for few threshold values are reported in Figure 3.15 (a) and (b) for PM and NPISUM mode, respectively.

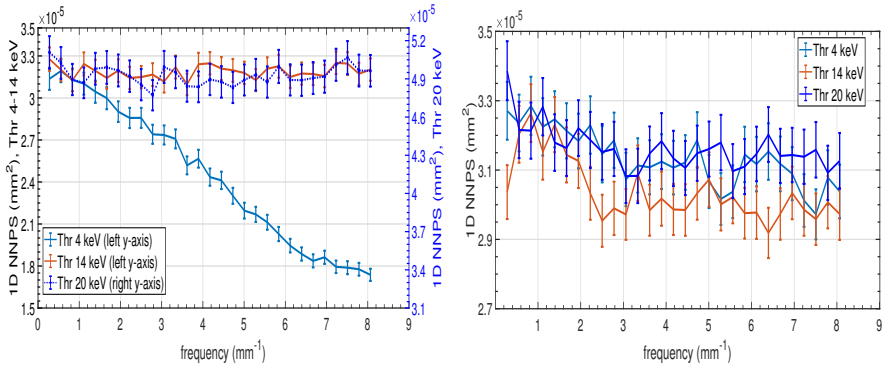

(a) (b)

Figure 3.15: 1D NNPS response for different thresholds with monochromatic beam $E = 26\ keV$: (a) PM mode; (b) NPISUM mode.

In PM mode:

- for $thr = 4\ keV$ ($thr < E/2$) multiple counts induce correlations between adjacent pixels acting as a low-pass filter that reduces the high frequency components of the NNPS.
- for $thr = 14\ keV$ ($thr \approx E/2$) multiple counts are totally removed and the NNPS is flat.

- for $thr = 20\ keV$ ($thr > E/2$) multiple counts are totally removed and the NNPS flat. The increase of NNPS magnitude is due to the loss of detection efficiency.

For NPISUM mode, the NNPS is quite flat with its magnitude independent from *thr* (Figure 3.15 (b)).

Figure 3.16 (a) and (b) show the 1D NNPS for PM and for NPISUM modes respectively, for photons with $E = 33\ keV$.

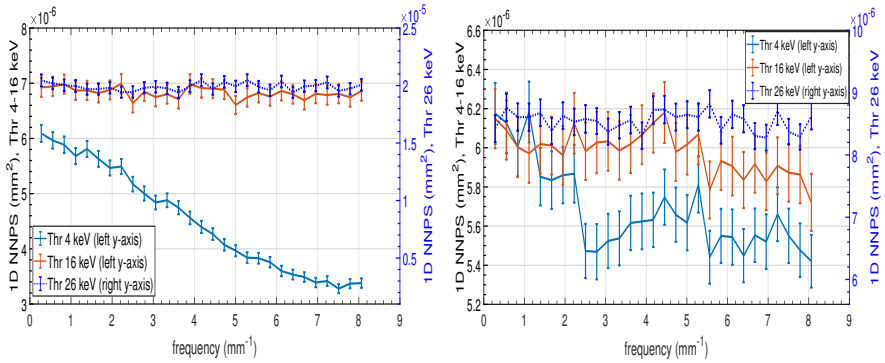

(a) (b)

Figure 3.16: 1D NNPS response for different thresholds using monochromatic beam $E = 33\ keV$. (a) PM mode; (b) NPISUM mode.

For $thr = 4\ keV$ ($< E_{Cd}/2$), the low-pass filtering effect on the 1D NNPSs is visible for both modes: in NPISUM mode it depends on Cd-emitted fluorescence photons; in PM mode it is due to multiple counting both from charge sharing and from fluorescence photons. By increasing the threshold to $thr > E/2$ the 1D NNPS flattens for both modes. The increase of the 1D NNPS in PM mode for $thr = 26\ keV$ can be explained in terms of loss of efficiency. This effect occurs also in NPISUM mode for $thr \geq 26\ keV$ when fluorescence photons are not recorded.

Aliasing

A digital imaging system with a pixel pitch of Δx is characterized by its Nyquist frequency $f_{Ny} = 1/(2\Delta x)$, that is the maximum frequency which can be correctly sampled without incurring in aliasing [87]. Since the presampling MTF is the response of the system to a sinusoidal input before the stage of sampling, all the components of MTF with frequency higher than f_{Ny} are aliased in the sampled image. For a pixellated detection system the NNPS is proportional to the MTF^2 [88]. Thus, when aliasing occurs, the components of the presampling NNPS above f_{Ny} are folded back and overlap with those below f_{Ny} increasing the high frequency components of the NNPS measured on sampled images [87, 95]. In these cases, the NNPS directly measured on digital images is flattened respect to the presampling NNPS.

For an XPCD, multiple counts act as a low-pass filter reducing the high frequency components of the signal. This means that when the system is undersampled multiple counts can limit the aliasing effects on noise by reducing the magnitude of the signal components above f_{Ny}.

Figure 3.14 shows that for all the settings the presampling MTF extents above the Nyquist frequency. This implies that the system is always undersampled and aliasing occurs.
Aliasing increases the high frequency components of noise, thus flattening the NNPS. Referring to Figures 3.15 and 3.16, the flattening of the NNPS is enhanced when using settings which remove multiple counts, i.e. PM mode combined with $thr > E/2$ or NPISUM mode for $E = 26\ keV$ and both PM and NPISUM modes combined with $thr > E/2$ for $E = 33\ keV$.
The effect of the detection or removal of multiple counts on both NNPS and presampling MTF can be summarized as follows:

- multiple counts detection worsens the presampling MTF and reduces the high frequency components of the NNPS. Moreover, working as a low-pass filtering in the stage before the sampling, it prevents aliasing effects such the flattening of the NNPS.
- multiple counts removal improves the spatial resolution but increases the high frequency components of the NNPS. The improvement of the spatial resolution leads to an increase of the magnitude of the presampling MTF components above f_{Ny}, thus aliasing effects are increased too.

3.3.7 *Signal to Noise Ratio (SNR)*

The SNR is a figure of merit extensively employed in medical imaging to evaluate, in the spatial domain, the performance of an imaging system. The SNR has been measured as follows:

$$\mathrm{SNR} = \frac{\bar{I}_{ROI}}{\sigma_{ROI}} \tag{3.5}$$

where $\bar{I}_{ROI}$ and σ_{ROI} are respectively the average signal and the standard deviation measured in a homogeneous ROI. The SNR has been evaluated on images corrected with the flat field procedure described in sect. 3.3.2. For the measure, ROIs large 450×30 *pixel* have been chosen to take the biggest area avoiding dead/hot pixels and inhomogeneities of the beam not corrected by the flat field procedure.

In this analysis, as done for the MTF and the NNPS measurements, the SNR has been evaluated as a function of the acquisition thresholds for two energies $E = 26\ keV$ and $E = 33\ keV$.

Considering an ideal detection system, for a monochromatic radiation with energy E the SNR is expected to be a flat function of the threshold (i.e. independent from the threshold settings) with a

sharp drop around $thr = E$. The plots of SNR against the acquisition thresholds are shown in Figure 3.17.

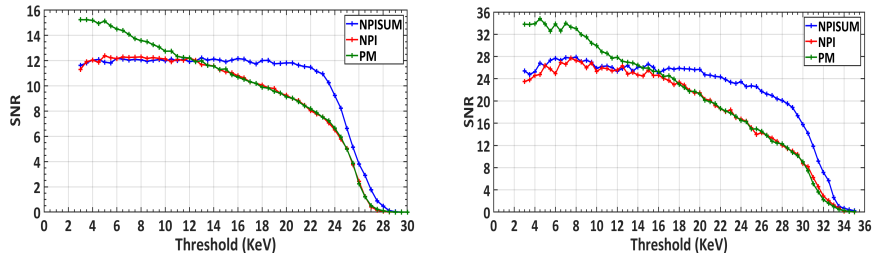

(a) (b)

Figure 3.17: Plots of SNR against the acquisition thresholds: (a) 26 KeV; (b) 33 KeV.

Referring to Figures 3.17 (a) and (b), the behaviors of PM, NPI and NPISUM modes can be explained as follows:

- PM mode does not correct charge sharing issues, thus pixels detecting shared signals measures a fraction of the total energy deposited in the sensor. The SNR is a decreasing function of the acquisition threshold since by increasing the threshold, the shared signals are gradually discriminated.

- NPI mode removes multiple counts without recovering shared signals. In this case, the SNR shows an ideal flat behavior up to $thr = E/2$. For $thr > E/2$ KeV, the shared signals are gradually discriminated with the increase of the acquisition threshold inducing a loss of efficiency. In this second range, the NPI mode behaves as the PM mode.

- NPISUM mode acts recovering the shared signals. For this mode the SNR is a flat function of the energies with a sharp drop off at thresholds around the actual energy of the impinging photons.

Figures 3.17 (a) and (b) show also that, for thresholds below $E/2$, the PM mode achieves the highest SNR if compared to the NPI and NPISUM modes. The increased SNR achievable by the PM mode can be explained considering that for $thr < E/2$, the PM mode detects multiple counts from charge-sharing that provide a smoothing of the high frequency components of the noise also preventing the occurrence of aliasing effects. The magnitude of such smoothing is proportional to the fraction of multiple counts detected and it decreases with the increase of the threshold. For thresholds above $E/2$, the NPISUM shows the best SNR response achievable among all the acquisition modes implemented in pixie-iii ASIC. This is explained considering that for $thr \geq E/2$ the NPISUM mode is the only one that preserves the detection efficiency, while both PM and NPI modes discriminate all the shared signals.

3.3.8 *Noise Equivalent Number of Quanta (NEQ)*

The global imaging performance of a detection system are the result of a compromise between spatial resolution and noise. For instance, if a physical phenomenon (such the charge sharing) induces a blur during the detection process, the noise decreases at the cost of a worsening of spatial resolution.

The NEQ measures the square of the Signal to Noise Ratio (SNR) in the frequency domain and it is defined as follows [87]:

$$NEQ(u) = \frac{MTF^2(u)}{NNPS(u)} \tag{3.6}$$

By quantifying, for each frequency, how the spatial resolution is impaired by the noise response, the NEQ stands as the optimal metrics to directly compare the overall imaging performance of a detection system under different acquisition settings.

The NEQ has been calculated from the presampling 1D MTF and from the measured 1D NNPS and studied as a function of the threshold.

Figure 3.18 shows the NEQ calculated in PM and NPISUM modes for the energy $E = 26\ keV$.

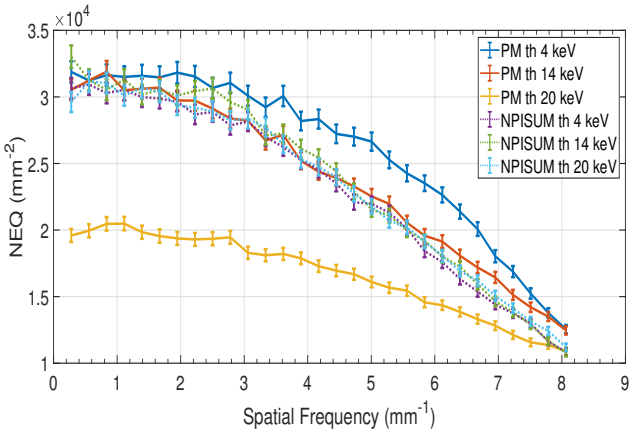

Figure 3.18: $E = 26\ keV$ NEQ response of PM Vs NPISUM mode.

The results can be summarized as follows:

- in the NPISUM mode the NEQ is almost independent from the threshold.
- in the PM mode the NEQ values decrease at all frequencies with the increase of the threshold. In particular, for $thr = 20\ keV$ there is a drop in the NEQ explainable with the loss of detection efficiency.

The plots of NEQ for the beam $E = 33\ keV$ are reported in Figure 3.19.

The behavior of the two modes when using different thresholds can be described in this way:

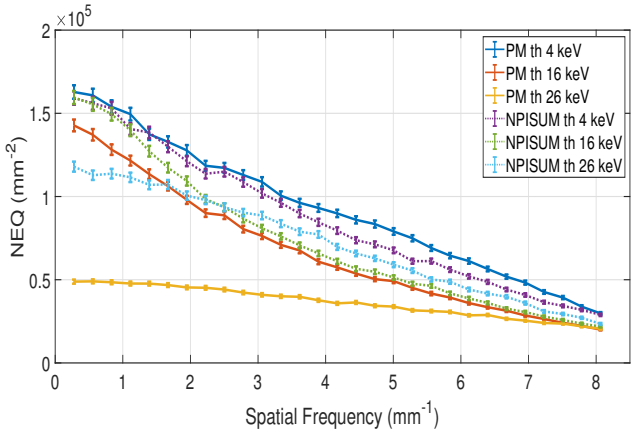

Figure 3.19: $E = 33\ keV$: NEQ response of PM Vs NPISUM mode.

- in the NPISUM mode, for spatial frequencies $< 2.2\ mm^{-1}$, the NEQ always decreases by increasing the threshold. For frequencies $> 2.2\ mm^{-1}$ the NEQ at $thr = 26\ keV$ is higher with respect to that measured for $thr = 16\ keV$. This behavior is due to the fact that fluorescence photons detection (possible for $thr < E_{Cd} = 23.1\ keV$) preserves the efficiency, but increases the noise (i.e. increases the NNPS) and worsens the MTF especially at high frequencies. In terms of NEQ, this means that, by discriminating fluorescence photons $thr = 26\ keV$ is more effective than $thr = 16\ keV$ in resolving spatial frequencies $> 2.2 mm^{-1}$.

- in the PM mode the NEQ response always decreases when increasing the threshold.

For both energies the combination of the PM mode with low thresholds shows the best NEQ response, i.e. the highest NEQ values at all frequencies.

3.4 DISCUSSION AND CONCLUSIONS

A comprehensive characterization of the Pixirad-1/pixie-iii XPCD has been carried out by considering different acquisition modes and threshold values.

The measurement of the linearity for a monochromatic energy $E = 24\ keV$ showed that: the PM mode is linear up to $2.0 \cdot 10^5$ (events/pixel/s) and linearizable up to $1.3 \cdot 10^6$ (events/pixel/s); the NPI mode is linear up to $2.9 \cdot 10^5$ (events/pixel/s) and linearizable up to $4.9 \cdot 10^5$ (events/pixel/s); the NPISUM mode is linear up to $1.0 \cdot 10^5$ (events/pixel/s) and linearizable up to $2.2 \cdot 10^5$ (events/pixel/s). Thus, if compared to the other modes, the PM mode allows imaging at higher fluence rates.

The measurement of the energy resolution demonstrated that only the NPISUM mode allows for a full energy resolution and, in the range

26 keV-50 keV, the energy resolution of NPISUM mode varies from 13% to 8.2%.

The spatial resolution measurements showed that the performance of the detection system strongly depend on the fraction of multiple counts recorded when charge sharing is not corrected: presampling LSF and MTF improve when high threshold values are set. Instead, the NPISUM mode, which fully corrects the charge-sharing effects, allows an almost threshold independent spatial resolution. More in general, for all the acquisition thresholds, the system achieves a LSF with $FWHM < 75\ \mu m$ (at $E \leq 33\ keV$). This feature makes this system suitable for in vivo microtomography [80, 81] and for breast imaging by allowing the resolution of breast micro-calcifications with typical diameters $< 0.5\ mm$ [96].

The analysis of the noise response confirmed that a higher fraction of multiple counts detection decreases the noise by reducing the high frequency components of the NNPS.

It has been observed that the system is always undersampled. However, by acting as a low-pass filter, the detection of multiple counts brings the system close to the condition of optimal sampling as described in sect. 3.3.6 and thus, it reduces aliasing effects on noise.

The overall imaging performance of the system with different acquisition settings and modes have been evaluated through the SNR and the NEQ. The first measures the response of the system in the spatial domain; the latter extents the measure to the frequency domain, thus allowing evaluating the best trade-off between spatial resolution and noise for all the spatial frequencies accessible by the system. In this analysis, the NEQ measurements are in agreement with the SNR and the results can be summarized as follows:

- the highest SNR and NEQ values are achieved by using the PM mode in combination with low thresholds. This means that, when using low thresholds ($thr < E/2$), the response of the system as well as the image quality are improved as more multiple counts are detected.

- for higher thresholds (in particular for $thr > E/2$), the NPISUM mode shows a better (SNR and NEQ) response if compared to the PM mode. In such cases, the NPISUM is expected to achieve the best image quality achievable by the detection system.

From these results it can be concluded that to perform imaging requiring both a sharp energy resolution and the use of high threshold values, which are common condition in spectral imaging, the charge summing algorithm (implemented by the NPISUM mode) has to be preferred to the single pixel mode (implemented by the PM mode).

For other imaging applications, in which a sharp energy resolution is not mandatory, multiple counts from charge sharing and fluorescence can improve the SNR and NEQ response by reducing the global noise

and the aliasing effects. In such cases, the single pixel mode coupled with low threshold values have to be preferred to the charge summing algorithm. This conclusion, here verified for the Pixirad-1/pixie-iii, can be extended to other XPCD devices with similar features.

Concluding, the results here presented show that the choice of the acquisition mode is task driven and not obvious. The evaluation of the image quality through SNR and NEQ measurements can guide the choice of the optimal combination of acquisition mode and operating threshold according to the specific application.

4

KES IMAGING WITH PIXIRAD-1/PIXIE-III SPECTRAL XPCD

As introduced in chapter 2, KES imaging is a spectral technique that requires the acquisition of two images with energies respectively below and above the K-edge of the target contrast medium. Among the available acquisition systems for spectral imaging described in sect. 2.3, the one implementing a spectral XPCD is becoming more and more attractive, especially for *in-vivo* KES imaging thanks to its single shot nature.

In this context, an imaging setup for micro-tomography with a spectral XPCD was implemented within the two year (2017-2019) project K-Edge Spectral μ-Tomography (KEST), funded by the INFN. KEST project used Pixirad-1/pixie-iii, an XPCD featuring high detection efficiency, good spectral resolution and high frame rates; characteristics of particular interest especially for *in vivo* spectral imaging. In particular, a feasibility study of KES micro-CT with the lab spectral setup was carried out for test-objects and *ex-vivo* samples.

Looking towards in *in vivo* X-ray tomographic KES imaging it would be desirable to acquire images with suitable statistics in the shortest time possible. Moreover, to get close to the the ideal application (i.e. two monochromatic energies set to either sides of the absorption edge), KES imaging with polychromatic sources requires the use of a narrow spectrum centered at the K-edge of interest. With an X-ray tube, the polychromatic spectrum can be optimized by properly tuning the kV settings and using thick absorbers to filter the low energies. However, the choice of the thickness and the absorbing power of the filtration is limited by the maximum current available by the X-ray source. Since the new generation of XPCDs allows imaging at reasonable fast frame rates, the bottleneck of the entire acquisition workflow for CT scans can be represented by a low photon fluence rate of the employed source. This limitation can be overcome by using a white synchrotron beam that has a fluence rate many orders of magnitude higher than the one of an X-ray tube. This implies also that it is possible to use absorption filters of different thicknesses and materials to shape an optimal spectrum, but still having a high fluence rate.

In order to further investigate KES imaging with XPCDs, in 2019 the INFN funded the three-year project K-edge Imaging with Synchrotron Sources (KISS). The project carried out two main streams of research, one of them aimed at the implementation of a fast KES-CT scanner suitable for *in-vivo* imaging and for time resolved (dynamic) functional X-ray imaging at synchrotron sources.

This chapter presents the experimental setups, the workflow developed to obtain tomographic KES images and the main results achieved within the KEST and KISS collaborations.

4.1 EXPERIMENTAL SETUP

Two setups were considered: the lab setup using an X-ray tube and the synchrotron setup.

lab-setup

The lab-setup was implemented at the medical physics laboratory of the INFN section of Pisa. The implemented setup, shown in Figure 4.1, operated in cone-beam geometry and it was suitable for both planar and tomographic imaging.

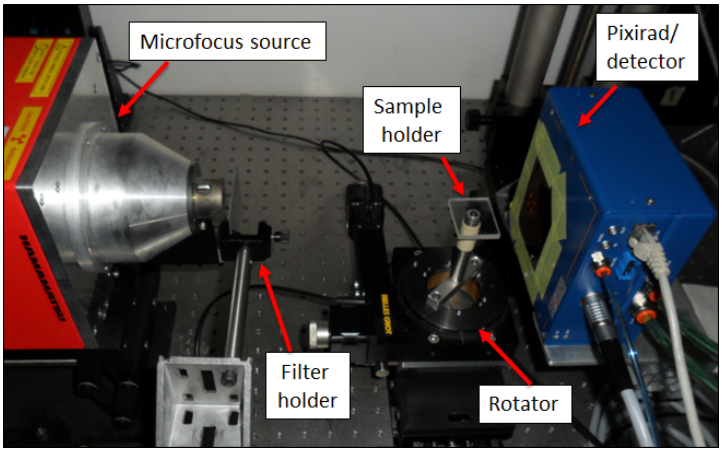

Figure 4.1: Setup for K-edge subtraction imaging implemented at the medical physics lab (INFN sect. of Pisa).

Referring to Figure 4.1, the acquisition setup included (from left to right) an Hamamatsu L9421-022 micro focus X-ray tube (tube voltage: 20-90 kV, tube current: 0-200 μA, maximum output: 8 W, X-ray focal spot size: 5 μm), a filter holder, a motorized rotator stage and the Pixirad-1/pixie-iii XPCD (described in sect. 3.2).

Cone-beam Geometry

By tuning the distances source-detector and source-sample, the cone-beam geometry allowed increasing/reducing the magnification and thus, the voxel size of the reconstructed images.

Synchrotron setup

The synchrotron setup can be implemented by installing the XPCD in the experimental hutch of a beamline. This setup takes advantage of the high fluxes allowed by the synchrotron sources to fully exploit the maximum frame-rate accessible by the XPCD. In particular, the high fluence rates typical of synchrotron sources allow shaping X-ray spectra optimized for target K-edge elements with suitable statistics. A possible solution to shape a polychromatic spectrum centered at the target K-edge energy is that of using absorption filters of different thicknesses and materials to realize an energy band-pass filter. Considering the absorption properties of different materials, a band-pass filter can be assembled as follows:

- low pass filter: a high Z element with a K-edge above the one of the target element.
- high-pass filter: Al or Cu thick absorbers to filter low energies.
- low Z elements (e.g. water, polyethylene) to tune the fluence rate.

In Figure 4.2 is reported the schematic of the acquisition setup based on synchrotron radiation.

Figure 4.2: Schematic of the synchrotron setup for KES imaging. The setup considers a white beam input; a band-pass filter made by absorbers with different thicknesses and materials; and a spectral XPCD.

Parallel-beam Geometry

In general, in the synchrotron setup (Figure 4.2) the most common geometry is the parallel beam, due to the high distance source-sample. In this geometry, no magnification occurs and the voxel size is determined by the pixel pitch of the imaging system employed.

Detector settings

Since the setup was dedicated to spectral imaging, coherently with the findings suggested by the characterization of the Pixirad-1/pixie-iii detection system, the detector was usually configured in NPISUM mode, while the PM mode was used only for comparing the image quality achievable by the two modes.

For KES imaging, the XPCD always operated in two colors mode. In this mode, by properly setting the two thresholds thr_1 and thr_2, it was possible acquiring two simultaneous images of the sample at two different energy bins 'low' and 'high'. The bin 'low' integrated all the photons between the two thresholds thr_1 and thr_2, while the bin 'high' integrated all the photons above thr_2 up to the endpoint of the X-ray spectrum. These two bins ('low' and 'high') were set to have mean energy respectively below and above the target K-edge.

Continuous/step-and-go modes

For CT scans, the system is able to acquire either in continuous mode or in 'step and go' mode. These two modes are commonly employed in experimental CT systems. In the continuous mode the sample rotates while the detector acquires CT projections at a fixed frame rate. In this approach the detector continuously acquires the frames and the CdTe sensor is biased during the whole acquisition. In the step and go mode, as suggested by the name, the sample is rotated of an established angular pitch at regular intervals (1 s in our system) and it is imaged while still. During the rotation, the detector

is inactive and the bias of the CdTe sensor can be restarted for each frame acquisition.

Both modes present pros and cons. If on one hand the continuous mode is faster than the step and go mode, on the other hand the continuous acquisition is prone to motion artifacts [97] and to artifacts arising from long exposure time that required a prolonged biasing of the CdTe sensor.

For the preliminary feasibility studies proposed in the framework of the KEST collaboration, the step and go mode was used without loss of generality. This choice was driven by the limited maximum fluence rate allowed by the source that, at the kVp and beam filtration mostly considered, was about two orders of magnitude below the maximum number of photons/pixel/second allowed by the pixie-iii readout system.

In perspective of *in vivo* applications, that require fast CT scans, the limitations of the continuous mode can be overcame by using the synchrotron setup and tuning the fluence rate just below the maximum fluence rate allowed by the detection system.

4.2 DEDICATED IMAGE PROCESSING PROCEDURE FOR KES IMAGING WITH PIXIRAD/PIXIE-III XPCD

Almost all digital X-ray imaging systems produce raw images that are not 'ready to go'. The imaging process is affected by several factors, for example a non uniform X-ray beam, inhomogeneity of the pixels gain, hot/dead pixels, time-dependent detector response or an unstable source. As result, the raw images show systematic or time-dependent artifacts that must be compensated. To this aim, a set of digital image processing procedures is commonly needed to make the images suitable for further steps, e.g. tomographic reconstruction or image segmentation. The specific image processing operations depend on the imaging hardware as well as the imaging task.

XPCDs potentially offer significant improvements to existing CT scanners where conventional charge integrating imaging devices are included [32, 60]. However, despite their attractiveness, XPCDs still present challenges for clinical applications. In fact, if not properly handled, imaging systems implementing XPCDs produce images affected by several artifacts that can impair their suitability. The most common issue of XPCDs is the inconsistency among detector pixels, which usually leads to structured noise in planar images and streaks and ring artifacts in CT images. Such inconsistencies are actually present in almost all imaging devices, however they are more evident in photon counting detectors due to the demand of high spatial resolution, to the inconsistencies in the energy threshold calibration between adjacent pixels [98, 38] and to polarization effects affecting high-Z sensors [35, 85]. Therefore, the acquired raw images are usually the input of

one or more digital image processing filters with the aim to obtain artifact-free images. However, the techniques employed in the image processing pipeline can strongly impair the spatial resolution of CT images and/or remove small but significant details, thus limiting the potentials of XPCD imaging devices.

In this section, the main steps followed to obtain high quality CT images with the Pixirad-1/pixie-iii XPCD imaging system are presented.

For the proposed experimental setup, a general image processing procedure has been implemented and optimized to achieve artifact-free images while minimizing the impact on the spatial resolution achievable by the system. This optimization work considers experimental images of a suitable test-object featuring circular details, thus to allow an easy quantitative assessment of the spatial resolution of the reconstructed CT images.

4.2.1 *Test-sample and CT geometry*

A multi-purpose simple test object for spectral imaging studies has been employed. The sample includes 5 pipettes, one filled with deionized water, the others filled with different dilutions in water of Iodine (Bayern Ultravist® 370), Barium ($BaCl_2$) and Gadolinium (Bracco MultiHance®) based contrast agents. A sketch of the phantom is reported in Figure 4.3.

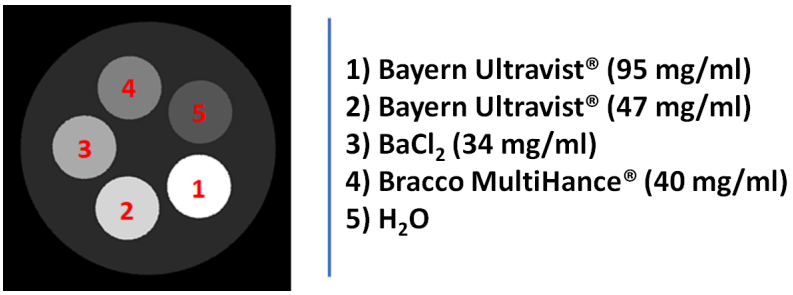

Figure 4.3: Sketch of the sample employed for the optimization of the image processing procedure. The reported dilutions in (mg/ml) refer to concentrations of the contrast elements (i.e. iodine, barium and gadolinium) in the pipettes.

By featuring circular details, this sample was optimal for evaluating the spatial resolution in CT reconstructed images with the circular-edge method [99, 100, 101], a modified version of the slanted edge method described in sect. 3.3.5.

The sample was imaged with the proposed lab-setup for KES imaging. The distances source-to-sample (D_{SO}) and source-to-detector (D_{SD}) were set respectively to 170 mm and 240 mm, resulting in a cone-beam geometry with a magnification factor of $M = D_{SD}/D_{SO} \approx 1.412$. With these settings, considering the nominal pixel size of 62 μm of the Pixirad-1/pixie-iii, a nominal isotropic voxel size of 43.9 μm was

achieved. The tube settings were: voltage = 45 kV, current = 160 μA, 2 mm Al filter. The detector settings were: exposure time of 1 s, 2 color mode, $thr_1 = 27.0$ keV, $thr_2 = 33.2$ keV. With these settings two images were collected in a single shot, denoted as "low" (27.0−33.2 keV) and "high" (from above 33.2 keV). Since thr_2 was set at the K-edge of iodine, the system was optimized for KES imaging of the iodinated contrast agent.

4.2.2 *Preparation of KES projections*

In two colors mode the Pixirad-1/pixie-iii outputs two set of images at two different energy bins ('low' and 'high').

The images 'low' and 'high' can be combined to obtain a KES image. As described in sect 2.2.1, the K-edge subtraction of the images can be easily performed by subtracting the planar (or tomographic) projections 'high' and 'low'. Denoting as $P_{low}(x,y)$ and $P_{high}(x,y)$ the two sets of radiographic projections, the KES projections $P_{KES}(x,y)$ were simply implemented as follows:

$$P_{KES}(x,y) = P_{high}(x,y) - P_{low}(x,y) \tag{4.1}$$

The $P_{KES}(x,y)$ can be then directly reconstructed to obtain KES-CT images segmenting the target K-edge element.

For the sake of completeness it is worth to specify that the projection 'low' and 'high' can be also reconstructed separately to produce CT images in the two energy bins defined by the thresholds (CT_{low}, CT_{high}). Moreover, by summing the images 'low' and 'high' before the flat field correction, the image integrating all the energies above thr_1 can be obtained.

4.2.3 *CT reconstructions*

The CT reconstructions were performed by using TIGRE toolbox [102, 103] . TIGRE is an open source Matlab/Python GPU toolbox featuring flexible CT geometries (e.g. cone beam, parallel beam, fan beam) and a wide variety of iterative reconstruction algorithms (e.g. SIRT, SART, CGLS, MLEM) as well as FBP and FDK.

The key feature of this toolbox is the GPU-implementation that considerably reduces the time required for CT reconstructions if compared to CPU-based implementations.

For the proposed lab-setup implementing a cone-beam geometry, the FDK algorithm was used.

4.2.4 *Custom filter for hot/dead pixels removal*

Due to limitations induced by the charge summing algorithm, the images acquired with the NPISUM mode show some clusters of hot/dead

pixels that do not appear in images acquired with the PM mode. As an example, in Figure 4.4 (a) and (b) are shown two raw images acquired with the NPISUM and the PM modes.

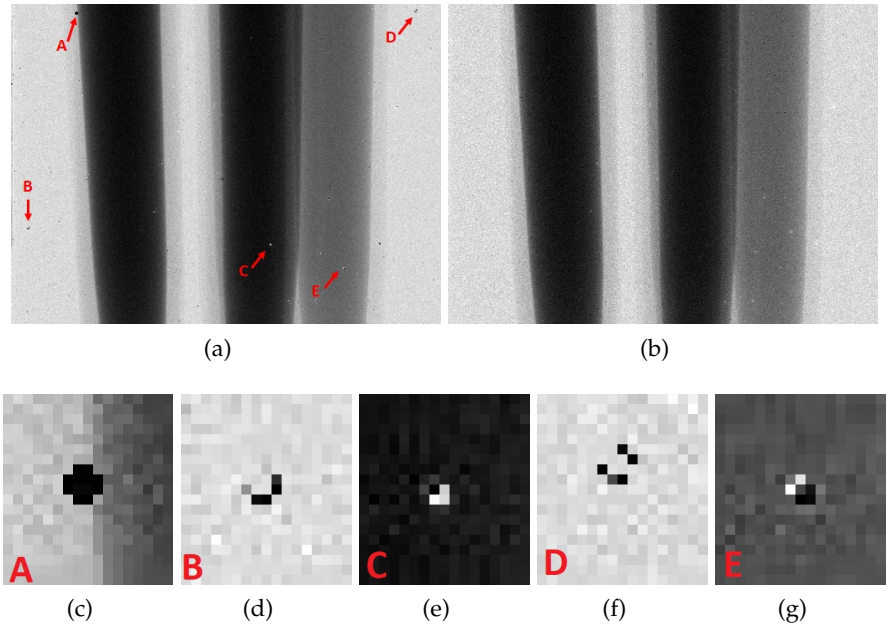

Figure 4.4: Raw images acquired with (a) NPISUM and (b) PM modes; (c-g) zoom on the clusters of hot/dead pixels (A-E) highlighted in (a).

The inhomogeneities highlighted in Figure 4.4 (a) and zoomed in (c-g) were observed to be usually clusters of 2 up to 16 neighboring hot/dead pixels. If not corrected, such clusters of defective pixels can originate streaks and ring artifacts in tomographic reconstructions that severely compromise the suitability of CT images.

The artifacts arising from the charge summing algorithm appear in different and unpredictable positions within the detection area, thus showing a time-dependent behavior. Therefore, since the conventional flat fielding cannot handle this dynamic behaviour, an adaptive solution is required.

Custom filter

To correct these clusters of hot/dead pixels, a custom automatic detection and removal non-linear filter was implemented in the preprocessing procedure (after the flat-field correction and before taking the negative logarithm). This filter belongs to the family of adaptive median filtering [104] and, in contrast with other non-linear filters such as the simple median filtering, it aims at preserving the spatial resolution of the images by operating selectively on the defective pixels thanks to a proper tuning of the parameter δ. The proposed filter considers a 5×5 neighborhood and its median gray value m. If the absolute difference between the gray-level of the central pixel and m is above a user-specified fixed threshold δ (in the range [0-1]), the value of the central pixel is then replaced. The replaced value is not m

but it is the median of the set composed by the pixels that satisfy the previous condition, i.e. having the absolute difference between their gray level and m below the threshold.

Figure 4.5 shows an example of application of the filter with $\delta = 0.1$.

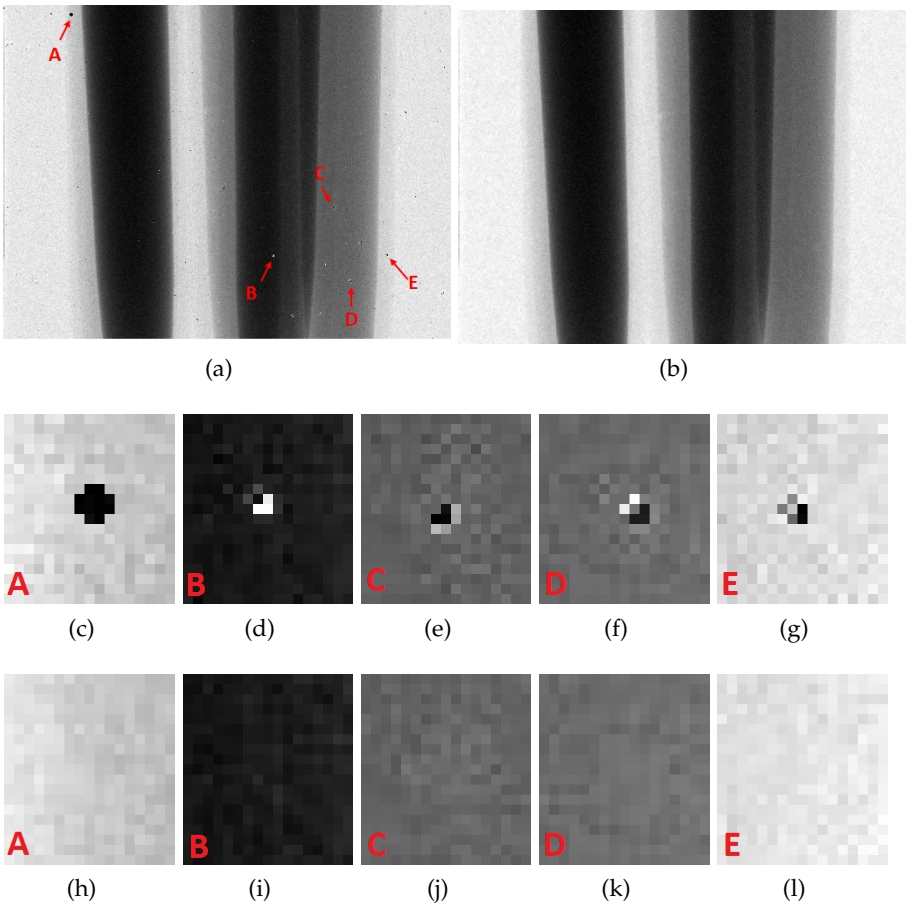

Figure 4.5: (top row) Raw (a) and corrected image (b). (central row) (c-g) ROIs taken from the raw image and centered on the clusters of hot/dead pixels (A-E) highlighted in (a). (bottom row) ROIs taken from the corrected image and centered on the clusters of hot/dead pixels (A-E) highlighted in (a).

Referring to Figure 4.5, the top row shows the same projection, on the (left) the raw image, on the (right) the corrected image with the proposed filter (with threshold $\delta = 0.1$). The central and the bottom rows show the same ROIs (20×20 pixels) zooming some of the defective pixels appearing in raw images and indicated in Figure 4.5 (a) with the letters A-B-C-D-E.

Figure 4.6 shows the same sinogram obtained with and without the proposed correction. The presence of the vertical stripes in the sinogram from uncorrected projections unavoidably leads to streaks and ring artifacts in the reconstructed images.

Optimization of the Custom filter

The key feature of the proposed filter is the threshold $0 \leq \delta \leq 1$, that

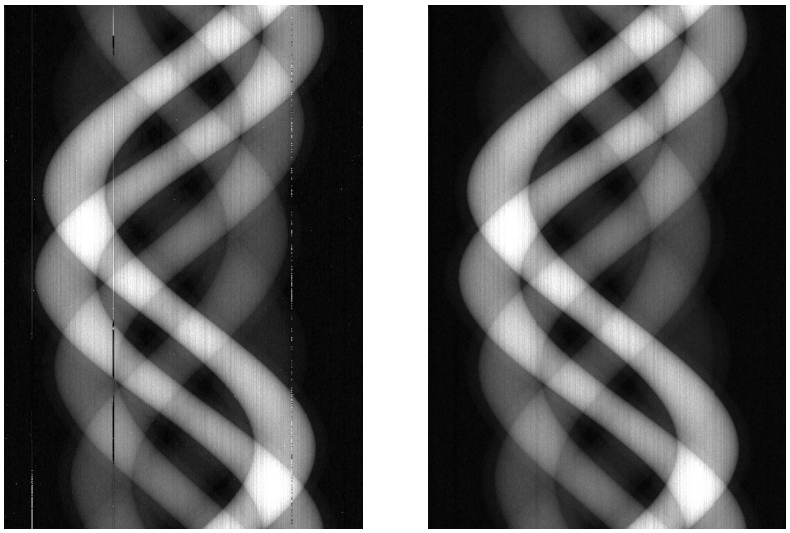

(a) (b)

Figure 4.6: Sinograms obtained from raw (a) and corrected (b) projections.

must be properly tuned to remove selectively the defective pixels in tomographic projections while preserving the spatial resolution in CT reconstructed images. For example, by reducing the threshold to very low values, the correction level (i.e. the number of corrected pixels) of the filter increases, however an increasing number of non defective pixels will be corrected too. As result, a smoothing factor affecting the spatial resolution can be induced. For high thresholds, the filter can become insensitive to the defective pixels and the correction can become ineffective. In this case, the spatial resolution is preserved, but streaks and ring artifacts will impair the image quality. Therefore, this parameter δ must be optimized experimentally to prevent streak artifacts while preserving the spatial resolution achievable by the imaging system.

In order to find the optimal threshold δ, the same set of CT projections was pre-processed by applying the proposed custom filter with different values of δ ($\delta = 0.01$; 0.05; 0.1; 0.2; 0.3; 0.4; 0.5 and 0.6). As reference, also unfiltered projections and projections processed with a median filter with a 3×3 kernel were considered to evaluate the effectiveness of the proposed approach. Then, both the unprocessed projections and the corrected projections were reconstructed via FDK. In CT reconstructions, the unprocessed projections are expected to achieve the highest spatial resolution, since no blurring are introduced by the filter employed in the pre-processing procedure. Therefore, the spatial resolution measured in unprocessed CT images has to be taken into account as reference for all the others pre-processed images.

The spatial resolution has been evaluated directly on CT images not corrected for ring artifacts. This choice has been made to evaluate only the influence of the analyzed filters on the spatial resolution,

thus excluding possible further modulations arising from the ring removal algorithms. For the measurement of the spatial resolution, an algorithm for circular-edge measurement has been been implemented in Matlab code. Since the circular-edge method requires high contrast details, the spatial resolution has been measured in the 'high' images using the detail featuring the highest contrast resolution, i.e. the pipette filled with an iodine concentration of 95 mg/ml (Bayern Ultravist®, pipette 1 in Figure 4.3). The ROIs used for the measurements are shown in Figure 4.7.

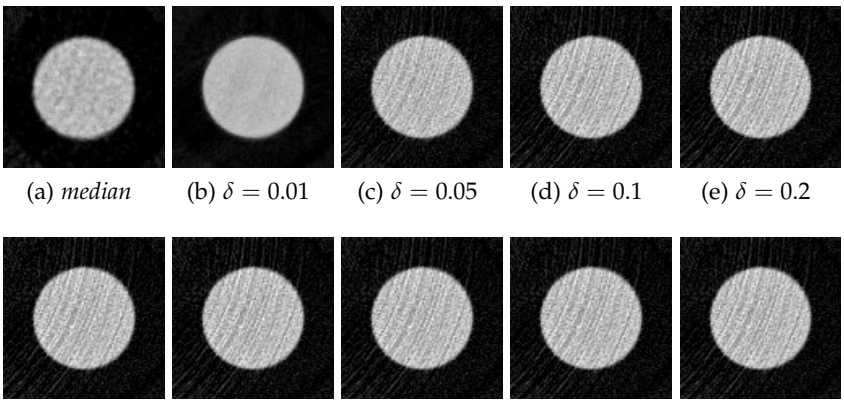

(a) *median* (b) $\delta = 0.01$ (c) $\delta = 0.05$ (d) $\delta = 0.1$ (e) $\delta = 0.2$

(f) $\delta = 0.3$ (g) $\delta = 0.4$ (h) $\delta = 0.5$ (i) $\delta = 0.6$ (j) *unprocessed*

Figure 4.7: Circular detail selected for the measurement of the spatial resolution. The ROIs are extracted from the same CT slice ('high') reconstructed using different pre-processing filters: (a) median filter (3×3) kernel; (b-i) custom filter with increasing values of δ; (l) none (i.e. unprocessed).

From the circular edges in Figure 4.7, the presampling ESF was extracted. The ESF profile was then fitted with the logistic function to have a noise-free profile. The LSF is the derivative of the fitted ESF, while the MTF is the Fourier transform of the LSF. In the spatial domain, the spatial resolution has been evaluated by measuring the average of the measured FWHM of the LSF. In the frequency domain, the spatial resolution has been assessed by measuring the $MTF_{50\%}$, i.e. the spatial frequency for which $MTF = 0.5$. The measure is schematized in Figure 4.8. To increase the statistics of the measurements, for each pre-processing filtration considered, the spatial resolution has been evaluated in five neighboring slices. To properly compare the spatial resolution achievable with both processed and unprocessed images, five slices without streak artifacts and with a reduced number of rings have been selected. For all the pre-processing procedures considered, the selected slices were the same. Finally, to evaluate the spatial resolution the average values of FWHM and $MTF_{50\%}$ were used while their standard deviations were reported as statistical error.

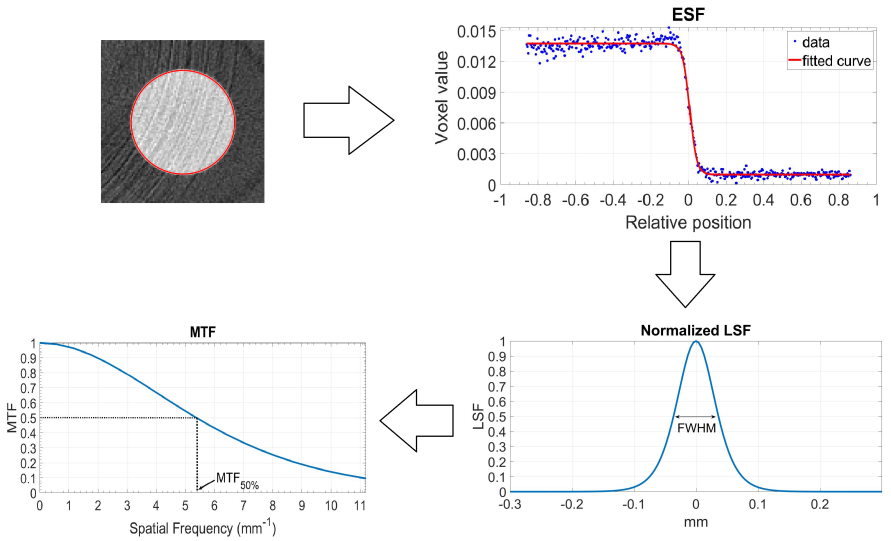

Figure 4.8: Flowchart for the measurement of Line Spread Function (LSF) and Modulation Transfer Function (MTF) with the circular edge method: (i) identification of the circular edge; (ii) the Edge Spread Function (ESF) is the plot of the gray levels against the relative distance from the edge; (iii) the LSF is the derivative of the ESF; (iv) the MTF is the Fourier Transform of the LSF.

4.2.5 *Ring artifacts correction*

Notwithstanding the pre-processing procedure strongly reduced the most of vertical stripes in the sinograms (see Figure 4.6), ring artifacts in the final reconstructed images can still occur. This is a common issue for high resolution micro-CT imaging systems implementing XPCDs. In such systems, in fact, the demand for high spatial resolution is pushed to the extremes and the conventional correction approaches, such as the flat-field correction, usually do not lead to satisfactory results in preventing ring artifacts [105, 106]. Since ring artifacts can impair the image suitability hampering quantitative analyses, ring removal solutions must be considered to improve the quality of the final CT images achievable with the proposed imaging setup.

The techniques for ring artifacts removal are generally divided in two families: pre-processing methods and post-reconstruction methods. The pre-processing methods are performed directly on sinograms (i.e. prior to the CT reconstruction) and operate by correcting the stripe artifacts in projection domain implementing specifically designed destripping filters [107, 108, 109, 110, 111]. The post-reconstruction methods correct ring artifacts after tomographic reconstruction. They take advantage of the observation that ring artifacts become straight vertical lines by transforming the input image into polar coordinates where the center of the ring artifacts is assumed as the center of the Cartesian-to-polar conversion. In this approach, the problem of ring

artifacts compensation can be brought back to a de-striping issue [106, 112, 113, 114, 115].

In the implementation of a general image processing pipeline, both pre- and post- reconstruction techniques were tested and compared. The de-stripping filters tested were: Rivers [116], Raven [117], Münch et al. [110], and Oimoen [107]. The de-stripping filters considered can be tuned by setting proper parameters which regulate their sensitivity and effectiveness in removing ring artifacts. In the proposed analysis, the filters were compared by setting the optimal parameters, i.e. the parameters that have been observed to maximally reduce the presence of rings in the images.

The effectiveness of both pre- and post- processing methods and the de-stripping filters were both qualitatively and quantitatively assessed. The qualitative analysis was simply based in the observation of the images, i.e. the presence, the absence or the reduced presence of ring artifacts were assessed. The quantitative analysis was carried out as follows: (i) thirty slices (the same for all ring removal methods considered) were selected; (ii) two circular ROIs with 30 *pixels* diameter were selected at the center of the two pipettes filled with 95 mg/ml and 47 mg/ml concentrations of iodine (Bayern Ultravist®, pipettes 1 and 2 in Figure 4.3); (iii) for each image processing considered, the SNR ($SNR_{95mg/ml}$ and $SNR_{47mg/ml}$) in the selected ROIs were measured over the selected slices; the standard deviation of the average of the repeated measures, i.e. the σ of the repeated measures divided by the mean root square of the repetitions, was reported as error. As reference for the pre- processing algorithm, the original images were considered, i.e. the images not processed with a de-stripping filter. As reference for the post- processing algorithm, the original images were processed as done in the post processing procedure, i.e. by applying the conversion Cartesian-polar and polar-Cartesian without considering any de-stripping filter. The $SNR_{95mg/ml}$ and $SNR_{47mg/ml}$ were measured both in the 'high' and KES-CT images.

In this analysis, since the presence of ring artifacts is expected to increase the noise on homogeneous regions of the sample by introducing unwanted circular strips, the most effective ring removal algorithm is the one that maximizes the SNR.

Once determined the most effective ring removal approach and the optimal de-stripping algorithm, the effect of such algorithm in the final spatial resolution of CT images was evaluated as described in the previous section.

4.2.6 *Results*

Optimization of the custom filter

Figure 4.9 shows the same CT slice (corresponding to the 'high' energy bin) reconstructed with: (a) projections filtered with the median filter

(3×3) kernel; (b-i) projections filtered with increasing values of δ (0.01; 0.05; 0.1; 0.2; 0.3; 0.4; 0.5 and 0.6); (l) unprocessed projections. To show how the use of a pre-processing filter can improve the image quality, for Figure 4.9 a slice affected by streaks artifacts (in the unprocessed image) has been selected. By comparing all the slices in Figure 4.9, it can be noted that the median filter is effective in removing streak artifacts, while the custom filter effectively prevents streak artifacts only for $\delta \leq 0.2$. For thresholds $\delta > 0.2$, streak artifacts appear in the images. In particular, the number and the intensity of such streak artifacts increase with the increase of the threshold δ set in the custom filter.

In Table 4.1 are reported the measured values of FWHM and the $MTF_{50\%}$ for all the considered pre-processing filters. Since in cone-beam geometry the voxel size is a function of the geometry, the FWHM has been reported also in unit of voxel size to extend the results to the parallel beam geometry, where the voxel size correspond to the nominal pixel size.

filter	δ	$FWHM$ (μm)	$MTF_{50\%}$ (mm^{-1})	$FWHM$ (voxel)
median	none	106 ± 1	3.6 ± 0.1	2.4
custom	0.01	90 ± 1	4.2 ± 0.1	2.0
custom	0.05	70 ± 1	5.2 ± 0.1	1.6
custom	0.1	62 ± 1	6.1 ± 0.1	1.4
custom	≥ 0.2	62 ± 1	6.1 ± 0.1	1.4
none	*none*	62 ± 1	6.2 ± 0.1	1.4

Table 4.1: Quantitative measurements of spatial resolution with different pre-processing filtration.

The results in Table 4.1 show that:

- As expected, the CT images obtained from unprocessed images achieve the best spatial resolution, i.e. the lowest FWHM and the highest $MTF_{50\%}$.
- The custom filter allows achieving the same spatial resolution of unprocessed images for thresholds $\delta \geq 0.1$. Thus, for $\delta \geq 0.1$, the custom filter does not affect the spatial resolution achievable by the imaging system.
- For threshold values $\delta < 0.1$, the custom filter affects the spatial resolution of CT images. In particular, the spatial resolution of CT images worsens by reducing the threshold δ.
- The median filter, by operating indiscriminately in the whole projections introduces a smoothing factor that leads to the worst spatial resolution in CT images.

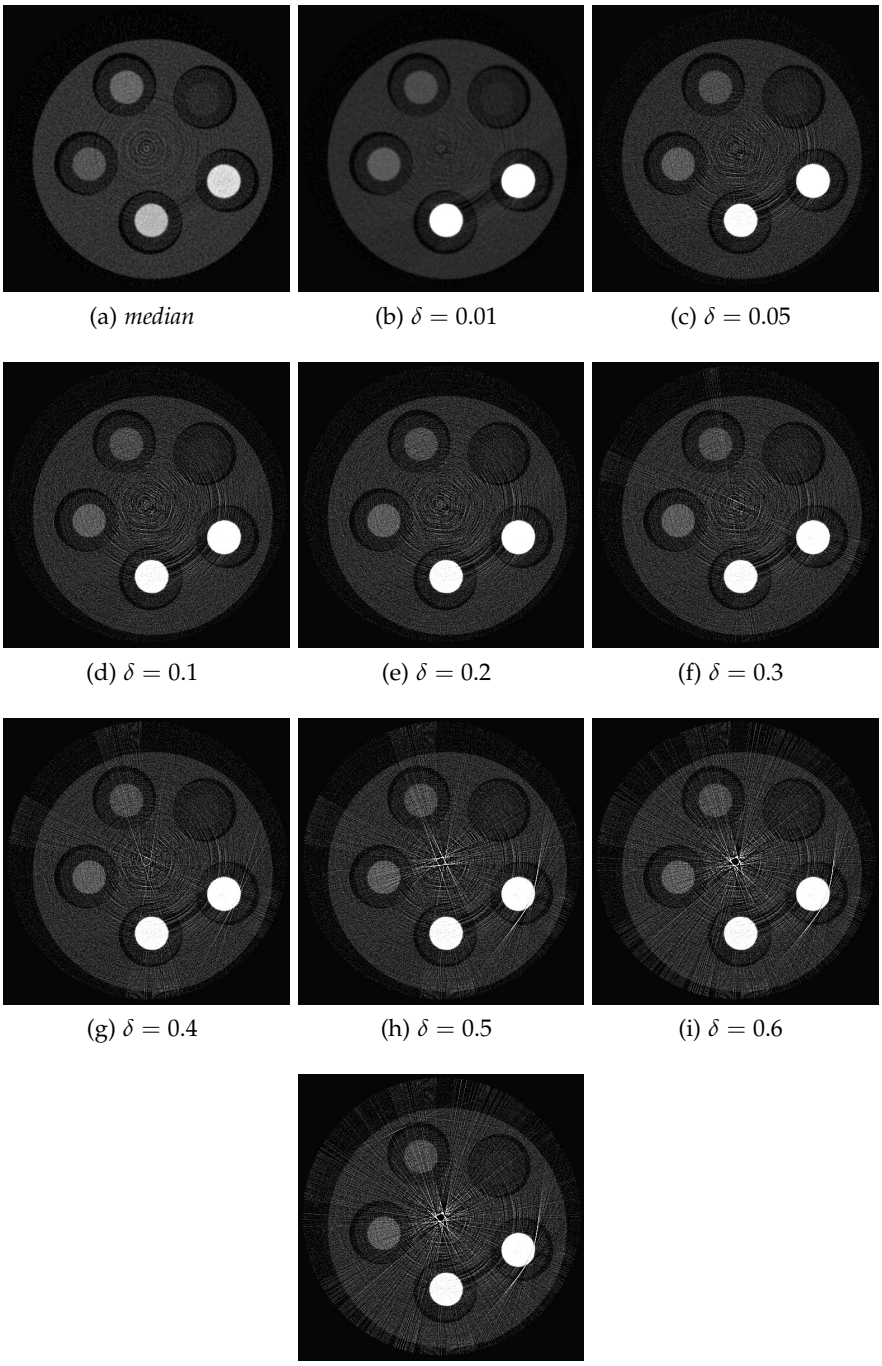

(a) *median* (b) $\delta = 0.01$ (c) $\delta = 0.05$

(d) $\delta = 0.1$ (e) $\delta = 0.2$ (f) $\delta = 0.3$

(g) $\delta = 0.4$ (h) $\delta = 0.5$ (i) $\delta = 0.6$

(j) *unprocessed*

Figure 4.9: Same CT slice ('high') reconstructed using different pre-processing filters: (a) median filter (3×3) kernel; (b-i) custom filter with increasing values of δ; (l) none (i.e. unprocessed).

From the results listed above it follows that even for very low thresholds values (e.g. $\delta = 0.01$), the custom filter outperforms the traditional median filter.

Considering both results in Figure 4.9 and in Table 4.1 it can be concluded that the custom filter: (i) preserves the spatial resolution of CT images for thresholds $\delta \geq 0.1$ (ii) prevents streak artifacts for $\delta \leq 0.2$. Thus, the optimal threshold δ can be found in the range ($0.1 \leq \delta_{opt} \leq 0.2$). However, considering that the ability of the custom filter of preventing streak artifacts increases when low values of threshold δ are set, the optimal threshold should be set to the minimum value of the range, i.e. $\delta_{opt} \approx 0.1$.

Ring artifacts correction

In Figures 4.10 and 4.11 the same CT slice (respectively 'high' and KES) obtained with all the considered ring-removal algorithms are shown.

In Tables 4.2 and 4.3 are reported the $SNR_{95mg/ml}$ and $SNR_{47mg/ml}$ measured on 'high' and KES-CT images processed with different de-stripping filters applied in both pre- and post- processing approaches.

	pre-processing		post-processing	
	$SNR_{95mg/ml}$	$SNR_{47mg/ml}$	$SNR_{95mg/ml}$	$SNR_{47mg/ml}$
unprocessed	8.9 ± 0.1	7.9 ± 0.1	8.8 ± 0.1	7.6 ± 0.1
Münch et al.	10.1 ± 0.1	8.9 ± 0.1	10.8 ± 0.1	9.2 ± 0.1
Oimoen	10.2 ± 0.1	8.6 ± 0.1	11.3 ± 0.1	9.6 ± 0.1
Raven	9.9 ± 0.1	8.6 ± 0.1	10.5 ± 0.1	9.2 ± 0.1
Rivers	9.0 ± 0.1	8.3 ± 0.1	9.7 ± 0.1	8.9 ± 0.1

Table 4.2: $SNR_{95mg/ml}$ and $SNR_{47mg/ml}$ measured on 'high' CT images processed with different de-stripping filters applied in pre- and post-processing approaches.

	pre-processing		post-processing	
	$SNR_{95mg/ml}$	$SNR_{47mg/ml}$	$SNR_{95mg/ml}$	$SNR_{47mg/ml}$
unprocessed	2.39 ± 0.03	1.96 ± 0.02	2.34 ± 0.02	1.88 ± 0.02
Münch et al.	2.65 ± 0.03	2.16 ± 0.03	2.85 ± 0.04	2.29 ± 0.03
Oimoen	2.59 ± 0.03	2.04 ± 0.03	2.92 ± 0.04	2.35 ± 0.03
Raven	2.60 ± 0.03	2.10 ± 0.03	2.81 ± 0.04	2.28 ± 0.03
Rivers	2.50 ± 0.03	2.09 ± 0.02	2.69 ± 0.03	2.25 ± 0.03

Table 4.3: $SNR_{95mg/ml}$ and $SNR_{47mg/ml}$ measured on KES CT images processed with different de-stripping filters applied in pre- and post-processing approaches.

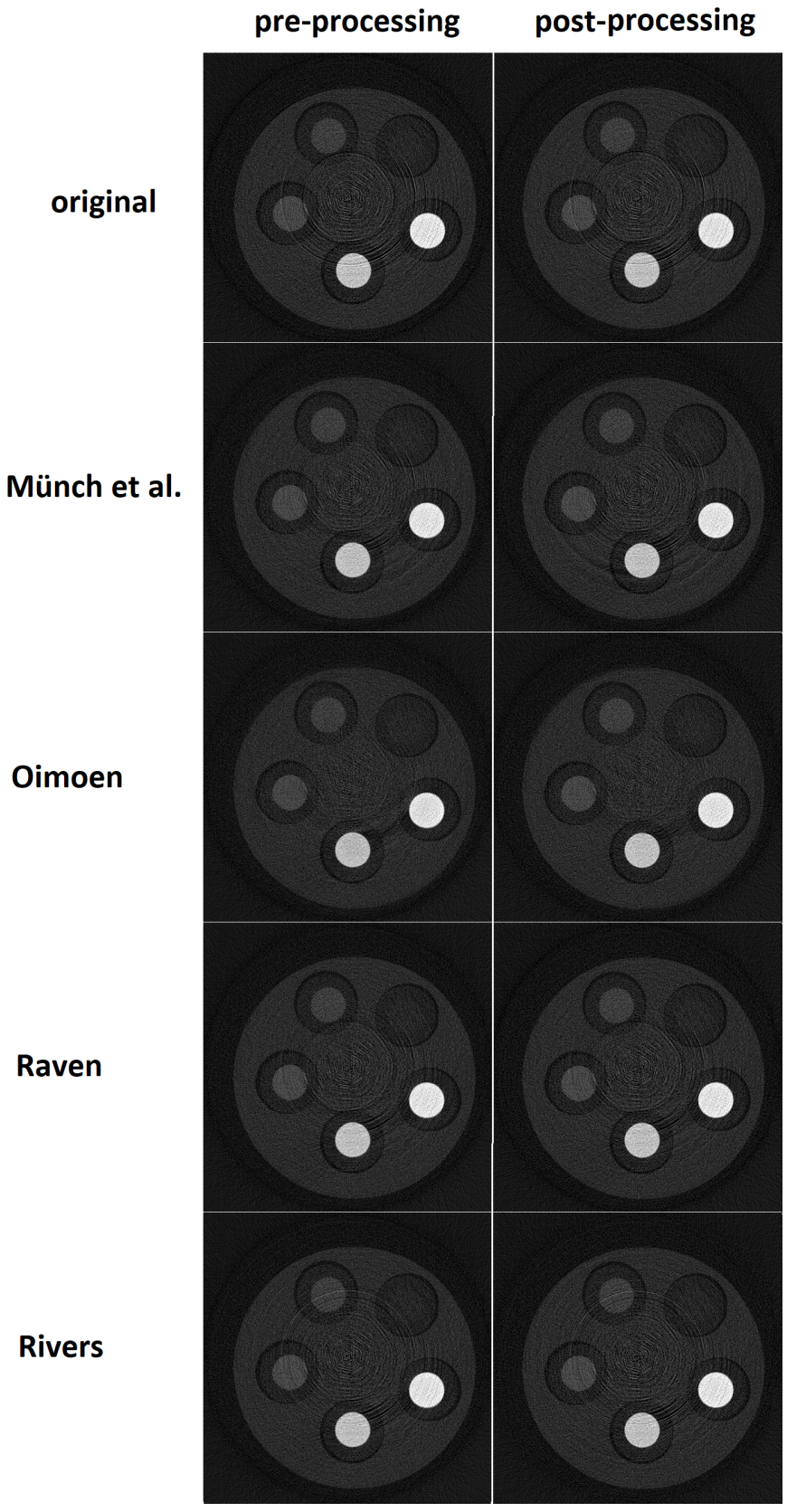

Figure 4.10: Same CT slice ('high') reconstructed using different ring removal algorithms.

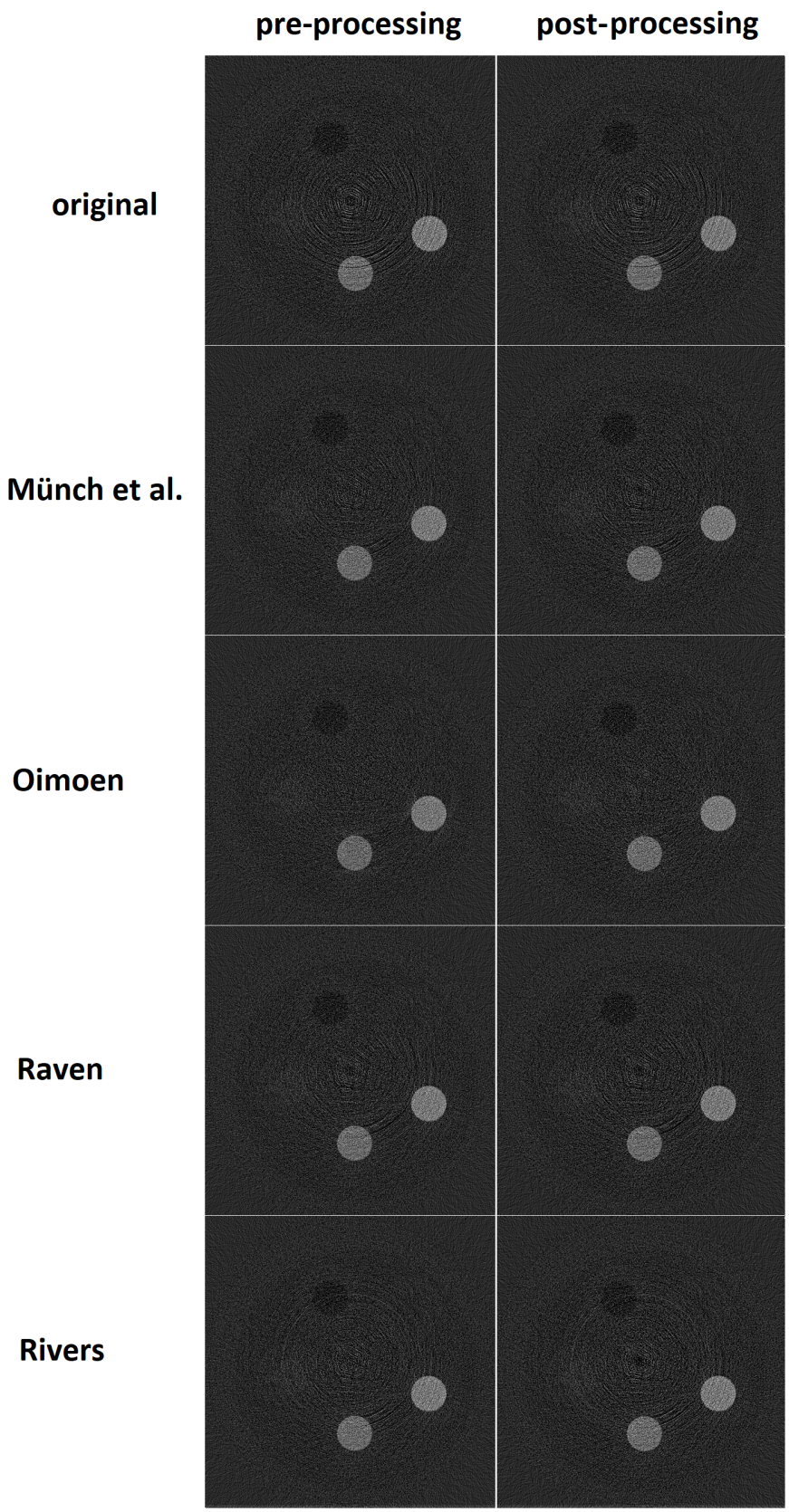

Figure 4.11: Same KES-CT slice reconstructed using different ring removal algorithms.

The results in Tables 4.2 and 4.3 show that, for both 'high' and KES images, the highest SNRs are achieved by the (Oimoen [107]) filter applied in the post processing approach. Thus, since a proper ring removal is expected to maximize the SNR measured on homegeneous regions by removing artificial circular features, the quantitative results suggest that the post processing approach combined with the (Oimoen [107]) de-stripping filter is the most effective among the considered algorithms. This result can be confirmed also by the qualitative observation and comparison of the actual CT images shown in Figures 4.10 and 4.11.

Of note, in the unprocessed images (i.e. in the images obtained without applying a de-stripping filter) the conversion Cartesian-polar-Cartesian slightly reduces the measured SNRs. This means that the Cartesian-polar-Cartesian transform does not intrinsically reduce the image noise by introducing unwanted smoothing factors in the final CT images. Therefore, the improvements in the SNR observed in the post-processing ring removal can be related only to the fact that the considered de-stripping filters are: (i) more effective if applied directly in reconstructed CT images in polar coordinates; (ii) less effective if applied on sinograms.

Figure 4.12 shows a CT slice of a test sample ('low', 'high' and KES) before and after the ring removal with the optimal settings, i.e. (Oimoen [107]) filter applied in the post-processing procedure.

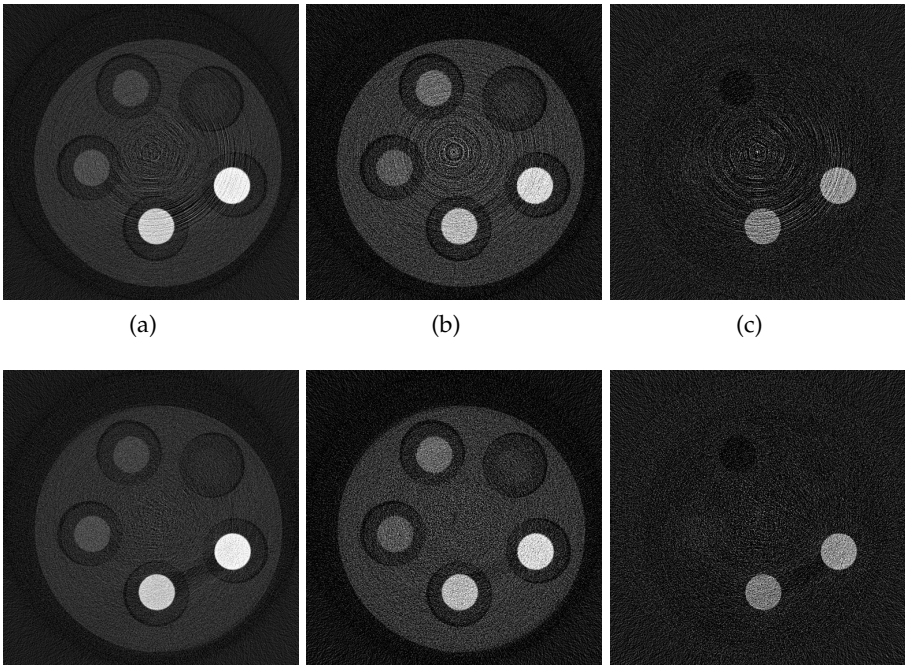

(a) (b) (c)

(d) (e) (f)

Figure 4.12: 'low' (a,d), 'high' (b,e), and KES (c,d) CT slices of a test sample before (top row) and after the ring removal (bottom row).

To evaluate if the optimal ring removal algorithm affects the image quality, the spatial resolution has been measured in the same circular detail both before and after the ring removal correction. The measured FWHM (of the LSF) and the $MTF_{50\%}$ are listed in table 4.4.

	FWHM (μm)	$MTF_{50\%}$	FWHM (voxel)
before ring removal	62 ± 1	6.1 ± 0.1	1.4
after ring removal	58 ± 1	6.6 ± 0.1	1.3

Table 4.4: FWHM (of LSF) and $MTF_{50\%}$ measured on CT images before and after the ring removal.

The results in Table 4.4 show that that after the ring removal correction, the spatial resolution slightly improves. This behavior can be explained considering that the presence of ring artifacts can modify the contours of details. In particular, sharp and smooth edges can become knurled in the presence of ring artifacts. As consequence, the spatial resolution can be deteriorated by ring artifacts. To give a feeling of the described behavior, a zoom of the circular detail employed for the measurement of the spatial resolution (before and after the ring removal) is shown in Figure 4.13.

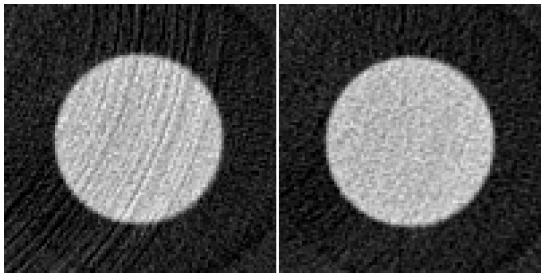

Figure 4.13: Zoom of the same circular detail before (left) and after (right) ring removal.

By observing Figure 4.13 it can be qualitatively noted how the visibility of the circular detail is improved in the image corrected for ring artifacts. In particular, the detail in the corrected image (Figure 4.13 (right)) appears to be sharpened if compared to the detail in the image not corrected for ring artifacts (Figure 4.13 (left)).

4.2.7 *Conclusions*

A pre-processing procedure tailored for CT imaging with the Pixirad-1/pixie-iii XPCD has been developed and optimized to achieve suitable artifact-free images. In the design and optimization of the whole procedure, particular effort has been put to preserve the high spatial resolution allowed by the use of a direct detection XPCD. This choice has been motivated by the idea that a standard image processing

procedure is intended to be the least invasive possible. Further improvements in CT images, such as additional image de-noise or SNR enhancing, are application-specific..

The source of artifacts in CT images with the pixie-iii detection module were mainly two: (i) the presence of peculiar clusters of dead/hot pixels appearing in planar images acquired with the NPISUM mode, i.e. the mode implementing the charge summing algorithm of particular interest for spectral imaging applications; (ii) the inconsistencies between the detector's pixels. In CT images, the first issue was source of several streaks and clearly visible ring artifacts; the second issue (common to the most of imaging systems) induced several subtle ring artifacts.

The peculiar artifacts induced by the NPISUM mode have been handled by implementing a custom threshold based non linear filter. The threshold ($0 \leq \delta \leq 1$) of the implemented filter has been optimized to selectively removing the clusters of dead/hot pixels with the aim of preventing artifacts in CT images while preserving the overall spatial resolution. In achieving this result, the specifically designed custom filter outperformed the median filter usually employed to correct speckles in the images. The optimal threshold for the custom filter was found to be $\delta_{opt} \approx 0.1$.

The ring artifacts appearing in CT images were approached with both pre- and post processing techniques, using four ring removal algorithms. The performance of these ring removal algorithms were tested and compared with both quantitative and qualitative evaluations. The result of this analysis showed that the (Oimoen [107]) ring removal filter applied in the post- processing procedure was the most effective. Moreover, as general result, the post- processing approach was shown to outperform the pre- processing technique. Establishing which of the two approaches (pre- or post- processing) is more effective in correcting ring artifacts was beyond the goals of this work. However, if generalized, this result can be of particular interest in defining a general approach to ring artifacts correction.

Concluding, CT imaging with XPCDs is mainly hampered by the inconsistencies between the detector pixels. This issue is further enhanced by the high spatial resolution allowed by direct detection XPCD such as the Pixirad-1/pixie-iii. The procedure here reported allows achieving artifact-free CT images by properly addressing all the issues presented by the pixie-iii detection module. The methods here presented can be extended to other imaging devices presenting similar characteristics to the Pixirad-1/Pixie-III imaging system.

4.3 EFFECTS OF CHARGE SHARING-CORRECTION ON KES IMAGE QUALITY

This section presents a comparison of KES-CT images acquired with the CdTe Pixirad-1/pixie-iii XPCD with and without the application of the charge summing algorithm.

In principle, as demonstrated by the characterization of the pixie-iii acquisition system (see chapter 3), the acquisition mode implementing the charge summing algorithm (NPISUM) achieves a threshold-independent spatial resolution and an energy resolution suitable for spectral imaging. Therefore, the NPISUM mode is expected to outperform the basic single pixel mode (PM) in achieving accurate KES-CT images. However, as shown in sect 3.1, the charge summing algorithm introduces characteristic artifacts that, if not properly corrected, can totally impair the quality of CT reconstructions.

The issues induced by the charge summing algorithm can represent a potential limitation to the theoretical advantages of the NPISUM mode over the PM mode. Moreover, the strategies implemented to correct for artifacts can affect the frequency contents of the noise response of the imaging system.

The goal of this section is to verify that, for KES-CT imaging, the theoretical advantages of the NPISUM mode over the PM mode actually translate into a better image quality, also considering the dedicated processing procedures described in sect. 4.2 to correct for artifacts arising from the charge summing algorithm.

The analysis here presented aims at comparing the image quality of the CT images acquired with the two modes NPISUM and PM. For the two modes, the image quality has been assessed by evaluating the Contrast to Noise Ratio (CNR), the spatial resolution and the noise response. The spatial resolution has been assessed in both the spatial and the frequency domain by measuring respectively the LSF and the MTF. The noise response has been evaluated in the frequency domain by measuring the Noise Power Spectrum (NPS) of KES-CT images. By combining the MTF and the NPS measurements, the NEQ assessing the trade-offs between noise and spatial resolution has been determined. The NEQ response of the two modes were finally compared, thus assessing the suitability of the NPISUM mode for spectral CT applications.

4.3.1 *Test objects and acquisition settings*

A simple test object made by 5 pipettes (in air) has been prepared. As shown in Figure 4.14, four pipettes were filled with different dilutions of an iodine-based contrast agent (Bayern Ultravist® 370); deionized water was used in the fifth pipette as a reference. The different dilutions of iodine in water were: 95 mg/ml, 47 mg/ml, 24 mg/ml,

19 mg/ml. Iodine was considered because it is a widely exploited contrast agent having a K-edge at 33.2 keV.

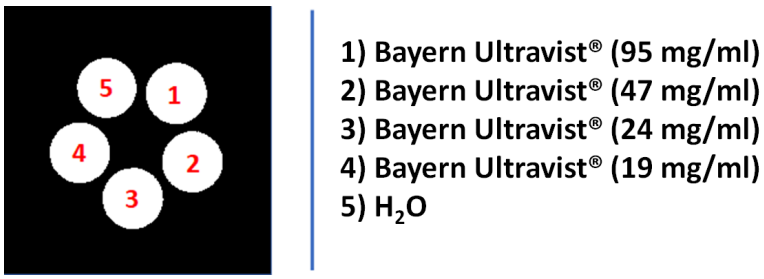

Figure 4.14: Sketch of the test-sample.

A source-to sample distance $D_{SO} = 170\ mm$ and a source-to-detector distance $D_{SD} = 240\ mm$ were considered. With these settings setup a magnification factor of 1.41 was achieved, resulting in a nominal isotropic voxel size of 43 μm. The tube settings were: voltage = 50 kV, current = 160μA, 1 $mmAl$ filter. The detector settings were: exposure time of 1 s, 2 color mode, threshold $thr_1 = 27.0\ keV$, threshold $thr_2 = 33.2\ keV$. With these settings the detector outputs two images in a single shot, denoted as 'low' (27.0 – 33.2 keV) and 'high' (from 33.2 keV).

4.3.2 *Image processing*

The CT projections acquired with the NPISUM mode were processed with the optimized non-linear custom filter presented in sect 4.2; CT projections acquired with the PM mode did not require particular pre-processing procedures.

Regarding CT reconstructions, for both the acquisition modes (PM and NPISUM) a ring artifacts correction was necessary. Therefore, independently from the acquisition mode, all CT images were processed with the same ring removal algorithm consisting in the (Oimoen [107]) de-stripping filter applied in polar coordinates.

4.3.3 *Image quality analysis*

To evaluate the image quality of CT reconstructions, the CNR was measured. Moreover, the spatial resolution and the noise response of CT images were assessed. Finally, by combining the measured MTF and NPS, the NEQ was measured for the two acquisition modes.

The measure of CNR was carried out in KES images by selecting 5 circular ROIs with diameter 70 *pixels* at the center of the pipettes. The selected ROIs are shown in Figure 4.15. Of note, to allow a proper visualization of all the features of the sample and of the actual position of the ROIs, the image shown in Figure 4.15 is a 'low' CT slice, while the measurements were performed in KES CT slices. Four ROIs refer

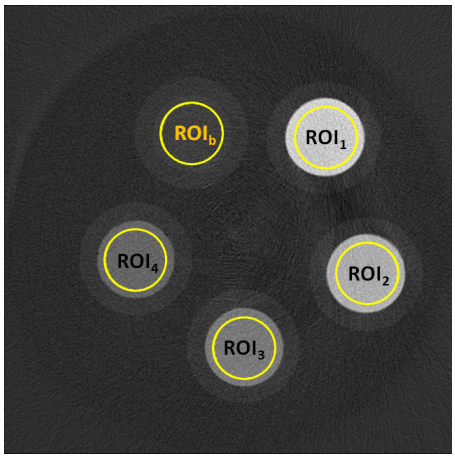

Figure 4.15: Example of ROIs selected for CNR measurements.

to different concentrations of the contrast agent, while the fifth ROI (ROI_b) refers to the pipette filled with de-ionized water, here assumed as background signal (μ_b). For each iodine dilution, the CNR has been evaluated as follows:

$$CNR_i = \frac{|\mu_i - \mu_b|}{\sqrt{\frac{\sigma_i^2 + \sigma_b^2}{2}}} \tag{4.2}$$

where μ and σ are the average and standard deviation of gray levels within a selected ROI_i and the background (ROI_b). For each iodine dilution, the CNR was measured over 10 slices, the average of the repeated measures were used, while their standard deviation were reported as statistical error.

The spatial resolution has been evaluated with the circular edge method in the most contrasted circular detail. In particular, for the measurement of the LSF and the MTF, the pipette filled with the 95 mg/ml solution in the 'high' image was selected. The FWHM of the LSF and the $MTF_{50\%}$ were reported as measures of the spatial resolution. The measure was repeated over 10 slices. The average of the FWHM and the $MTF_{50\%}$ of the repeated measures were reported; their standard deviation were reported as statistical error.

The noise response has been assessed by measuring the 3D, 2D and 1D NPS. For this measurement, a set of flat field images has been acquired and reconstructed with the same acquisition settings set for the acquisition of the actual sample (see Figure 4.16 (a)). Then, the 3D NPS has been measured in KES CT images with the following formula ([86, 87, 88]):

$$NPS(u,v,w) = \frac{\Delta x \Delta y \Delta z}{N_x N_y N_z M} \sum_{i=1}^{M} |FFT_{3D}(ROI_i(x,y,z) - \overline{ROI_i})|^2 \tag{4.3}$$

where u, v and w are the axes of the frequency domain, $ROI_i(x,y,z)$ is the *i-th* ROI, $\overline{ROI_i}$ the average signal of the *i-th* ROI, M the total

number of ROIs, Δx, Δy Δz the voxel sides and N_x, N_y, N_z the number of voxels in the selected ROI along the three directions. The measure of 3D NPS has been carried out by selecting a set of 22 ROIs with size $100 \times 100 \times 382$, selected as described in Figure 4.16. The 1D NPS was

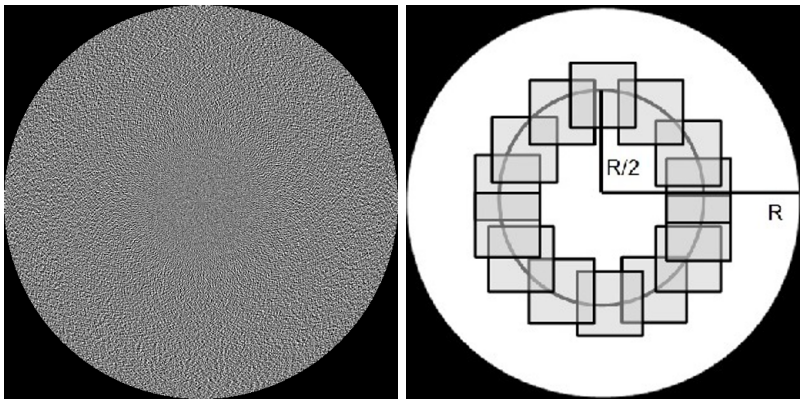

(a) (b)

Figure 4.16: (a) Example of CT reconstruction of flat field projections. (b) Example of ROI selection for NPS measurements: in the CT volume, ROIs overlapping for $> 50\%$ of their area were selected along a circumference with radius $R/2$, where R is the half size of the CT slice; with these settings 22 3D ROIs can be extracted.

calculated as follows:

- the $NPS(u, v, w)$ was integrated along the w frequency, thus obtaining a 2D $NPS(u, v)$.
- for images reconstructed with the FDK algorithm the $NPS(u, v)$ is expected to have a radial symmetry, thus the 1D NPS profile has been obtained by computing the radial average profile of $NPS(u, v)$ in polar coordinates.
- in polar coordinates the NPS can be written as a function of the radial frequency k (with $k = \sqrt{u^2 + v^2}$), i.e. $NPS(k)$.
- the 1D NPS profile was rebinned in frequency bins of width 0.233 mm^{-1} to obtain a smooth $NPS(k)$ plot.

The NEQ describes the square of the SNR in the frequency domain. As already described in sect 3.3.8 for planar images, the NEQ quantifies the trade-off between spatial resolution and noise and stands as the optimal metric to assess and compare two different systems or acquisition modes. For CT images, the NEQ is defined as follows [118, 119, 120]:

$$NEQ(u, v, w) = \pi k \cdot \frac{MTF^2(k)}{NPS(k)}; \tag{4.4}$$

Equivalently to the planar case, the NEQ can be interpreted as the number quanta that would produce the same SNR given an ideal

detector and reconstruction system [86]. Finally, the NEQ achieved by the two modes (NPISUM and PM) were compared.

4.3.4 *Results*

Figure 4.17 reports both 'low' and 'high' planar projections acquired by the detector in PM and NPISUM modes. The SNR of the flat-corrected

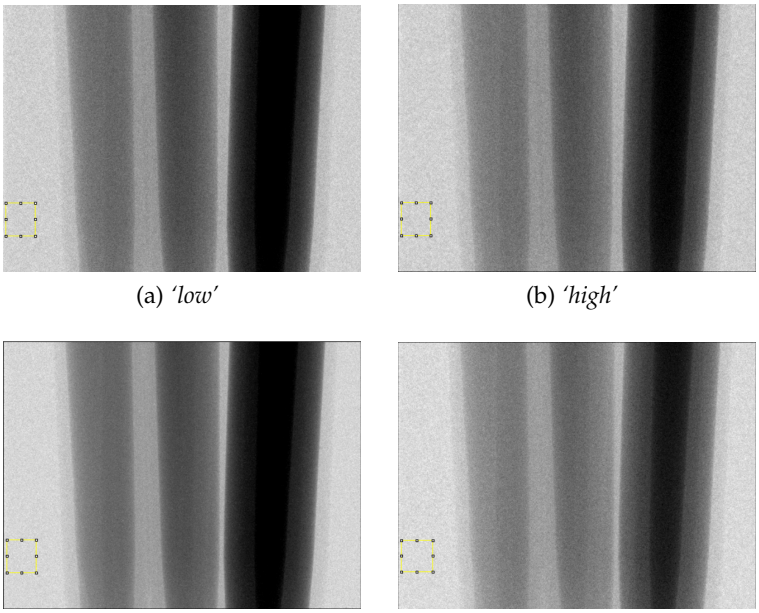

(a) *'low'* (b) *'high'*

(c) *'low'* (d) *'high'*

Figure 4.17: A projection in PM mode (top row) and NPISUM mode (bottom row). The selected ROI (45×45) pixels was set for the SNR measurement.

images evaluated in the highlighted ROI in Figure 4.17 was used to compare the planar projections. The measured SNR were respectively $SNR_{low} = 30.8$ - $SNR_{high} = 26.2$ for the NPISUM mode and $SNR_{low} = 23.0$ - $SNR_{high} = 21.8$ for the PM mode. As shown also in chapter 3, the higher SNR achieved by the NPISUM mode is mainly due to the preservation of the detection efficiency when using thresholds set to high energies, as typically required for spectral imaging.

Figure 4.18 reports the same ('low', 'high' and KES) CT slice for both PM and NPISUM modes. To allow a proper visualization of the differences between the signals reconstructed with both the PM and the NPISUM modes, Figure 4.19 shows the plot profile along the dashed line highlighted in Figure 4.18. To increase the visibility of contrast differences, the plot in Figure 4.19 has been smoothed with the Savitzky-Golay filter [121]. The value of the CNR measured for each iodine concentration for both acquisition modes are reported in Table 4.5. The last column of Table 4.5 reports the ratio CNR_{NPISUM}/CNR_{PM}

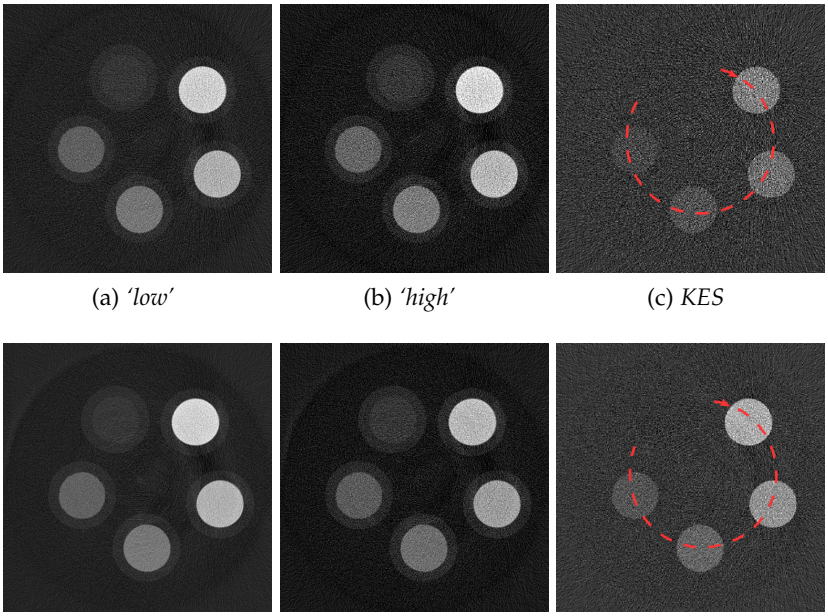

(a) *'low'* (b) *'high'* (c) *KES*

(d) *'low'* (e) *'high'* (f) *KES*

Figure 4.18: "low" (left column), "high" (middle column) and KES (right column) CT slice for the PM mode (top row) and NPISUM mode (bottom row).

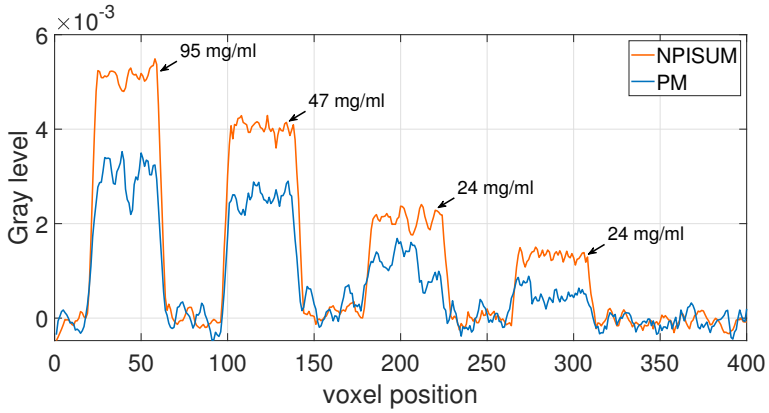

Figure 4.19: Line profile of the dashed segments highlighted in Fig. 4.18. The arrows indicate the dilutions of iodine in water.

to evaluate the increment in CNR achieved by the NPISUM mode if compared to the PM mode.

Dilution	CNR_{PM}	CNR_{NPISUM}	CNR_{NPISUM}/CNR_{PM}
95 mg/ml	2.24 ± 0.02	7.4 ± 0.1	3.3 ± 0.1
47 mg/ml	1.99 ± 0.02	6.7 ± 0.1	3.4 ± 0.1
24 mg/ml	1.78 ± 0.04	5.5 ± 0.1	3.1 ± 0.1
19 mg/ml	1.39 ± 0.04	4.4 ± 0.2	3.1 ± 0.2

Table 4.5: CNR measured for PM and NPISUM modes. The last column quantifies the increment in CNR achieved by the NPISUM mode over the PM mode.

From the results in Table 4.5 it can be noticed that the NPISUM mode achieves a noticeable increment (a factor 3) in CNR if compared to the PM mode. This increment does not depend on the concentration of the contrast agent, thus it is a general property of the imaging system that can be related to the increased efficiency and energy resolution achieved by the NPISUM mode.

In Figure 4.20 are plotted the MTF and the LSF measured for both PM and NPISUM modes. The values of the FWHM (of the LSF) and the $MTF_{50\%}$ are reported in the plots. The results in Figure 4.20 show

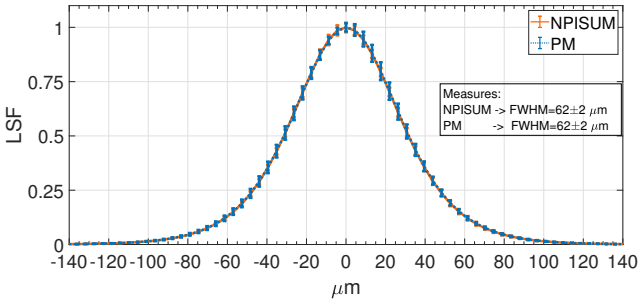

(a)

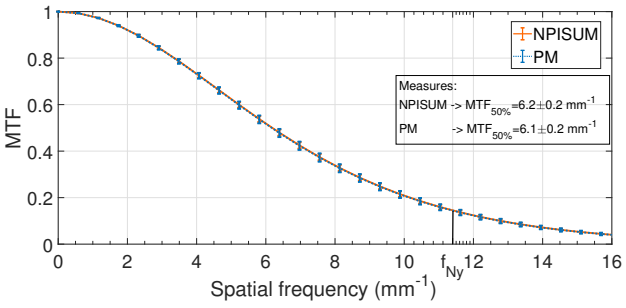

(b)

Figure 4.20: Plots of LSF (a) and MTF (b) for CT images in PM and NPISUM modes.

that for CT reconstructions, the NPISUM and the PM modes achieve

the same spatial resolution since both the LSF and MTF are practically superimposed. This is an expected result, since, as demonstrated in sect. 3.3.5, for high thresholds the spatial resolution in PM mode increases. In particular, for $thr \geq E/2$ (where E is the energy of the incoming radiation) the PM mode achieves a comparable or better spatial resolution than the one achieved by the NPISUM mode. As reference, in Figure 4.20 (b), the Nyquist frequency f_{Ny} is indicated. Of note, if compared with the planar case reported in chapter 3, in CT images the effects of Aliasing are noticeably reduced. This is due to the fact that both the interpolations needed for tomographic reconstructions and the increasing of the Nyquist frequency induced by the magnification of the lab-setup contribute in reducing the components of MTF above f_{Ny}, thus preventing aliasing effects.

Figure 4.21 shows the axial (plane $w = 0$), the coronal (plane $v = 0$) and the sagittal (plane $u = 0$) planes of the 3D NPS measured in CT slices acquired with NPISUM and PM modes. The representative planes

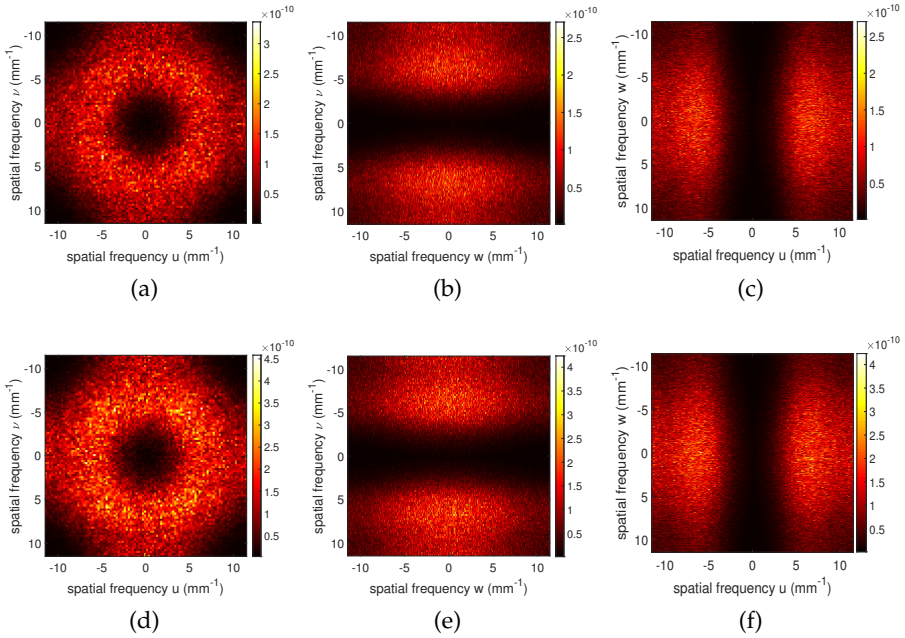

Figure 4.21: axial (left column), coronal (middle column) and sagittal (right column) planes of the 3D NPS measured for CT images acquired with the NPISUM (top row) and NPI (bottom row) modes.

of the 3D NPS reported in Figure 4.21 show the characteristic cylindrical symmetry (radial symmetry along the axial pane $w = 0$) induced by the ramp-filter (Ram-Lak) used in FDK algorithm. In both the axial NPS referring to NPISUM and PM modes (respectively Figure 4.21 (a) and (d)), small effects of aliasing can be observed. The presence of aliasing can be appreciated by observing the slight break in the axial symmetry in proximity of the edges of the plots of the axial NPS. In CT images these small effects of aliasing do not represent a limitation,

since they can be prevented by using some additional filtration to the ramp-filter in the FDK algorithm, such as e.g. Shepp-Logan, Hamming, Hann or other apodization filters.

To directly compare the noise response of the two modes, the radially averaged 1D NPS profiles are shown in Figure 4.22.

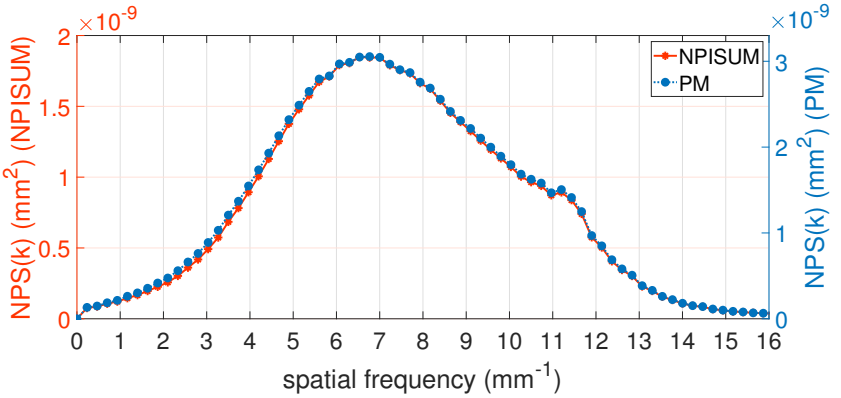

Figure 4.22: 1D NPS for NPISUM and PM modes.

Figure 4.22 clearly shows that, apart for a scale factor, the NPS curves have the same shape reaching their maximum for spatial frequencies around 6.8 mm^{-1}. Therefore, the two modes lead to the same noise texture of CT images. More interestingly, for the NPISUM mode the NPS magnitude is reduced of a factor (1.7) if compared to the PM mode. This means that the NPISUM mode allows for a noise reduction while maintaining the same noise texture of the PM mode.

Finally, the NEQ response of the two modes is shown in Figure 4.23.

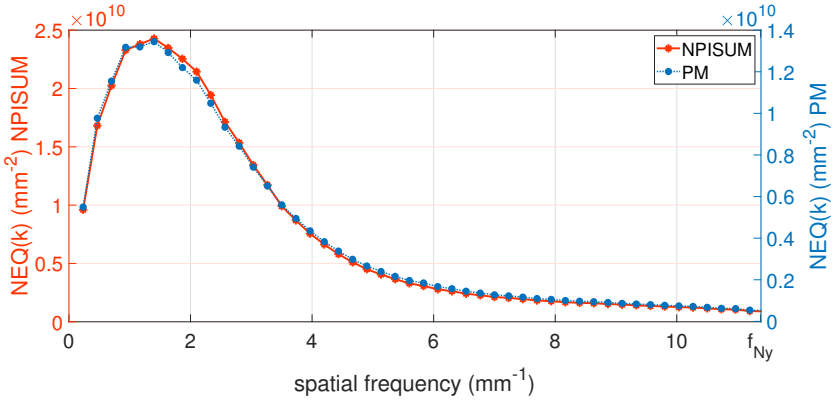

Figure 4.23: $NEQ(k)$ for NPISUM and PM modes.

By comparing the NEQ plots in Figure 4.23, it can be concluded that for KES imaging, the NPISUM definitively outperforms the PM mode in the whole range of accessible frequencies. Considering that the two modes achieve the same spatial resolution, the main advantage of the NPISUM mode over the PM mode is the noise reduction shown in Figure 4.22. As observed for the NPS, the two NEQ curves show the same shape,

differing only for a scale factor. This scale factor has been quantified as follows $NEQ_{NPISUM}(k)/NEQ_{PM}(k) = 1.7$. Recalling the meaning of NEQ as the number of photons per mm^2 that actually contribute to the image formation [86], it can be concluded that with the acquisition settings typical of KES imaging, the NPISUM mode allows imaging with an increased number of photons per mm^2 if compared to the PM mode. This means that by being more efficient than the PM mode, the NPISUM mode leads to a considerable improvement in the KES image quality.

4.3.5 *Conclusions*

The KES-CT image quality achieved by the two modes (PM and NPISUM) implemented in the Pixirad-1/pixie-iii were directly compared by using objective metrics in both the spatial and the frequency domain.

The measurements showed that, for KES-CT applications, the NPISUM mode outperforms the PM mode by achieving higher CNR (increase factor ≈ 3.2) and NEQ response (increase factor 1.7).

The analysis of the image quality in the frequency domain demonstrated that, apart from a scale factor, the behavior of the $NPS(k)$ and the $NEQ(K)$ against the frequency is the same for both modes. This result confirms that the procedures adopted to correct for the typical artifact arising from the charge summing algorithm do not affect the frequency content of CT images, thus maintaining unaltered the noise texture and the spatial resolution of the system. Therefore, the NPISUM mode achieves an improved KES image quality while maintaining the same frequency content of noise and spatial resolution achieved by the PM mode.

4.4 DEVELOPMENT AND VALIDATION OF A SIMULATOR FOR X-RAY IMAGING WITH SPECTRAL XPCDS

The experimental activity related to reproducible phenomena usually requires the use of specific instrumentation or poorly accessible lab-facilities. In such cases, the development of a reliable model-based simulator that allows emulating the physical phenomenon under investigation can represent a valuable solution. As an example, a simulation tool able to reproduce with accuracy an actual phenomenon can be adopted to properly plan the experimental activity, to simulate a great number of events not always experimentally collectible, to perform time-consuming optimization studies and so on.

Since the underlying physics of X-ray imaging concerning the interactions radiation-matter and the statistical behavior of a photon distribution is a well known matter, the imaging process can be the ideal subject for simulations.

This section presents the development and the validation of a simulator able to reproduce the formation of X-ray images for the specific

case of KES imaging with a spectral XPCD implementing two thresholds (thr_1 and thr_2).

The simulator has been developed in Matlab code and it is essentially a modified version of the one developed and validated for the case of breast CT with monochromatic radiation [122, 123]. The simulator here presented has been extended to the polychromatic case and it includes a modeling for the spectral separation of the detected photons operated by the energy thresholds implemented in the XPCD with given characteristics. In addition, to consider also the physics underlying the CdTe sensor, a simplified Monte Carlo model has been implemented to simulate the spectroscopic performance of the Pixirad/pixie-iii XPCD.

The simulator takes as input the X-ray spectrum, the acquisition geometry, the sample geometry and composition, the characteristics of the XPCD (i.e. detection efficiency, energy resolution, pixel size), and the settings of the energy thresholds. As output of the simulation process two images, referring to the energy bins 'low' ($thr_1 \leq E \leq thr_2$) and 'high' ($E > thr_2$), are produced.

The simulator has been validated by considering experimental images of a test sample made by two pipettes filled with two solutions of an iodinated contrast agent in water acquired with the Pixirad-1/Pixie-iii in the lab-setup. Then, by reproducing the experimental conditions in the simulator, the simulated images were compared with the experimental ones. The quantitative comparison between experimental and simulated images has been carried out via measurements of contrast, noise and CNR.

In addition to the simulator, an analytical formula to calculate the contrast, the noise and the CNR of a KES image has been derived from theoretical considerations. The analytical formula is intended to calculate the ground truth of the imaging process since it is not affected by fluctuations typical of random stochastic processes, including the presence of infinite values and Nan induced by photon starvation in radiographic projections.

The results showed a good agreement between simulations, analytical derivations and the experimental images.

4.4.1 *Simulator description*

The simulation of the processes involved in the formation of X-ray images with spectral XPCDs are hereafter explained step by step.

X-ray source

The shape of an X-ray spectrum $W(E)$ is a characteristics of the source. In principle, the model here discussed can take as input a custom spectrum that can be either monochromatic or polychromatic. Since this work focuses on a setup for KES imaging with a polychromatic

X-ray source, the spectra generated by an ideal X-ray tube have been simulated with Spektr 3.0 [124], a computational toolkit developed in Matlab. This toolkit is based on the model developed by (Hernandez and Boone [125]) named Tungsten Anode Spectral Model using Interpolating Cubic Splines (TASMICS). Spektr 3.0 toolkit allows to tune the kVp in the range 20-150 (kV) and it outputs a spectrum at 100 cm from a point-source in unit of $photons/mm^2/mAs$.

The distance source-detector can be easily adjusted considering that the intensity of a point-source follows the inverse-square law.

The simulated spectra can be further shaped by considering an additional filtration. In particular, Spektr 3.0 allows adding filters from a wide set of elements and compounds of settable thicknesses.

The spectrum W generated by Spektr 3.0 is a sampled function of the energies $W(E_i)$ with steps of 1 keV (i.e. $E_{i+1} - E_i = 1\ keV$). For the scope of this work the spectra were rebinned considering energy bins of 0.1 keV.

Sample acquisition geometry and X-ray attenuation through the sample

The simulator handles each energy bin of the spectrum $W_{in}(E_i)$ as a monochromatic beam with energy E_i.

The geometry and the composition of the sample are defined by a mathematical phantom made by a 3D spatial distribution of attenuation coefficients $\mu(E_i)$. The X-ray detector is modeled as a 2D matrix of pixels with a defined pixel pitch. The transmitted spectrum $W_{out}(E_i)$ in input to the XPCD pixel matrix is calculated by computing the forward projection.

The forward projection was performed by using the functions implemented in the All Scales Tomographic Reconstruction Antwerp (ASTRA) toolbox. Thanks to the flexible geometries implemented by the ASTRA toolbox, the simulations can be performed in different geometries: parallel-beam; fan-beam and cone-beam.

Photon counting detector

The simulated CdTe XPCD is an ideal counter implementing two energy thresholds and the charge summing algorithm.

Spectroscopic Performance of CdTe XPCD

The spectroscopic performance of an XPCD are potentially affected both by the charge-sharing issue and by secondary fluorescence photons induced within the semiconductor sensor. This means that the spectrum $W_{det}(E)$ observed by the XPCD is different from the spectrum $W_{out}(E)$ in input. To consider this aspect in the simulation procedure a Monte Carlo (MC) model has been implemented as described in Appendix C. By considering the physics underlying CdTe sensors, the model computes the spectrum $w_{det}(E)$ from a given spectrum $W(E)$ in input to the XPCD.

Acquisition thresholds model

A realistic XPCD model has to consider also the limited energy resolution featured by the energy thresholds. For an XPCD the main sources of fluctuations leading to an imperfect energy resolution are: (i) the random electronic noise due to the signal processing chain; (ii) the statistical noise arising from the discrete nature of the measured signal [4]. As reported in literature, the fluctuations concurring in the energy resolution degradation are reasonably Gaussian distributed around the energy of the detected photon [4, 38, 35]. The FWHM of the resulting distribution ($FWHM \approx 2.35 \cdot \sigma$) is adopted to measure the energy resolution (En_{res}) of a spectral detector. The overall FWHM can be written as the quadrature sum of the FWHM of the electronic noise $FWHM_{el}$ and the statistical noise $FWHM_{stat}$:

$$FWHM^2_{overall} = FWHM^2_{el} + FWHM^2_{stat} \tag{4.5}$$

For an XPCD, the electronic noise is the dominant factor affecting the energy resolution [35]. However, the statistical noise is of particular interest since it determines the minimum theoretical limit in the energy resolution achievable by a perfect XPCD mounting a given semiconductor sensor.

From theoretical considerations, the $FWHM_{stat}$ can be defined as follows [4]:

$$FWHM_{stat} = 2.35 \cdot \sqrt{F \cdot \frac{E}{\omega_p}} \tag{4.6}$$

where F is the Fano factor, E the energy of the incoming X-ray photon and ω_p the average pair (hole-electron) creation energy. As an example, for a CdTe sensor assuming a Fano factor of 0.15 [126] and $\omega_p = 4.43\ eV$ [127], the minimum energy resolution achievable for photons with energy 33 keV is $FWHM_{stat} \approx 79\ eV$.

From the considerations described above, in the simulator the acquisition threshold has been modeled as a Gaussian distribution of the energies with mean $\mu = thr$ and σ that depends on the characteristics of the acquisition system. In this description, the probability of detecting/discriminating a photon with energy E by setting a threshold thr can be described as follows:

$$\phi(E, thr) = \frac{1}{2} \cdot \left(1 + erf\left(\frac{E - thr}{\sigma\sqrt{2}}\right)\right) \tag{4.7}$$

where 'erf' is the error function, i.e. the cumulative distribution of the Gaussian distribution describing, in this case, the response of the energy threshold thr.

The cumulative distribution $\phi(E, thr)$ in eq. 4.7 is a probability function with values in the range (0-1) that describes the probability of detecting/discriminating photons with energy E once set a threshold thr. As an example, for an XPCD with 100% detection efficiency and for a fixed threshold thr: if $\phi(E, thr) = 0$, no photons with energy E are detected; if $\phi(E, thr) = 1$, all the photons with energy E are detected;

if $\phi(E, thr) = 0.4$, the 40% of the interacting photons with energy E are detected and the remaining 60% are discriminated.

Energy bins

For an XPCD implementing two thresholds, the detected photons are allocated into two energy bins according to their energy. In particular, the energy bins ΔE_1 and ΔE_2 selected by the two thresholds implemented by the XPCD can be described by the following expressions:

$$\begin{cases} (\Delta E_1) & W_{det}(E) \cdot \phi(E, thr_1) - W_{det}(E) \cdot \phi(E, thr_2) \\ (\Delta E_2) & W_{det}(E) \cdot \phi(E, thr_2) \end{cases} \tag{4.8}$$

In Figure 4.24, for different XPCDs with different En_{res}, are reported few examples of the formation of the bins ΔE_1 and ΔE_2, considering an input spectrum generated by an X-ray tube (voltage: 40 kV; filtration:0.253 μmCu).

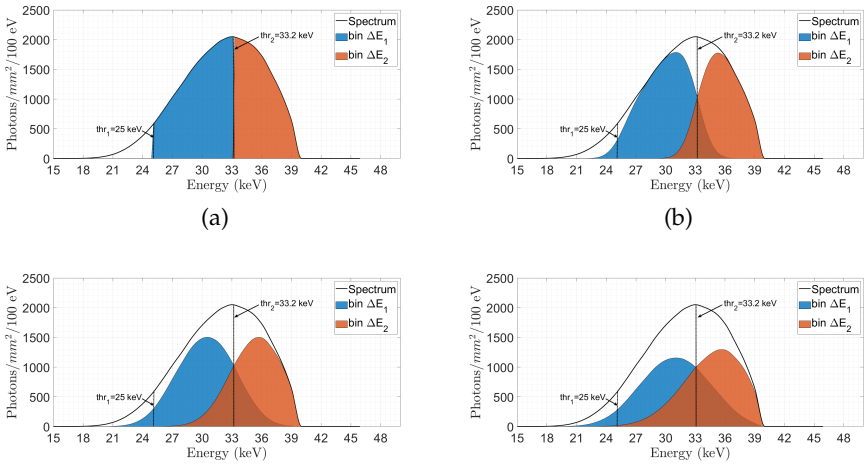

Figure 4.24: Example of energy bins formation with $thr1 = 25\ keV$ and $thr_2 = 33.2\ keV$. (a) $En_{res} = 0.079\ keV$, (b) $En_{res} = 3\ keV$, (c) $En_{res} = 6\ keV$, (d) $En_{res} = 10\ keV$.

Energy resolution and overlaps between the energy bins

Referring to Figure 4.24 it can be observed how the worsening of the energy resolution induces an increasing overlap between the energy bins. For the scope of KES imaging, an increasing overlap between the two energy bins is expected to reduce the KES signals. Therefore, the use of an XPCD featuring a good energy resolution is an essential requirement for the technique.

Image formation

The final output of the simulation process are two 2D images. For the particular application of KES imaging, these images are called 'low' and 'high'. In particular, for each pixel located in a position (x, y), the

image $I_{low}(x,y)$ integrates all the photons in the bin ΔE_1, the image $I_{high}(x,y)$ integrates all the photons in the bin ΔE_2:

$$\begin{cases} I_{low}(x,y) = \int_E W_{det}(E,x,y)\ (\phi(E,thr_1) - \phi(E,thr_2))\ dE \\ I_{high}(x,y) = \int_E W_{det}(E,x,y)\ \phi(E,thr_2)\ dE \end{cases} \tag{4.9}$$

Referring to eq. 4.9, the thr_2 should be set above thr_1. In the simulation program, to remove the ambiguity when $thr_1 > thr_2$ eq. 4.9 is rephrased as follows:

$$\begin{cases} I_{low}(x,y) = 0 \\ I_{high}(x,y) = \int_E W_{det}(E,x,y) \cdot \phi(E,thr_1)\ dE \end{cases} \tag{4.10}$$

Finally, considering that an XPCD discriminates the thermal noise, for an ideal imaging system the only source of noise is represented by the quantic nature of photons that obeys to the Poisson statistics. Therefore, as final stage, the simulator adds a Poissonian noise to the images $I_{low}(x,y)$ and $I_{high}(x,y)$.

To produce the radiographic projections (eq. 1.8), the simulator outputs also flat field images. The statistics of the flat field images can be selected by the user. The KES projections P_{KES} are, finally, obtained by subtracting the projections 'high' (P_{high}) and 'low' (P_{low}): $P_{KES}(x,y) = P_{high}(x,y) - P_{low}(x,y)$

4.4.2 *Analytical formula for KES imaging*

The simulator described above reproduces the formation of X-ray images. However, the stochastic nature of the image formation implies also that fluctuation in the measurable quantities (e.g. SNR, KES signal etc.) in the images can occur. To have a reference, in addition to the simulator, an analytical formula to calculate the KES signal and the ideal noise along a single line integral in the forward projection has been derived. The analytical calculations are intended to be the background truth of the simulation process. However, it is worth to note that this approach does not reproduce the effects due to photon starvation such as the possible occurrence of NaN and Infinite values in the actual images.

KES signal and noise

The analytical formula calculates the KES signal and the ideal noise detected by a single pixel of the XPCD along a defined line integral ξ.

The processes taken into account by the analytical formula are very similar to those employed in the simulator and are hereafter summarized.

Given an input spectrum $W_{in}(E)$, the output spectrum $W_{out}(E)$ along a line integral ξ is defined by the Lambert Beer's law (eq. 1.5).

The spectrum detected by the CdTe sensor $W_{det}(E)$ is calculated by the MC model.

Once set the two acquisition thresholds (thr_1, thr_2), the number of photons detected in each bin is calculated with eq. 4.9, here rewritten as follows:

$$\begin{cases} N^{\xi}_{low} = \int_E W_{det}(E,x,y)\ (\phi(E,thr_1) - \phi(E,thr_2))\ dE \\ N^{\xi}_{high} = \int_E W_{det}(E,x,y)\ \phi(E,thr_2)\ dE \end{cases} \tag{4.11}$$

where N^{ξ}_{low} and N^{ξ}_{high} are the number of photons along the line integral ξ detected by the XPCD in the two energy bins.

The KES signal along the line integral ξ is therefore calculated by combining eq. 1.8 and eq. 4.11 as follows:

$$KES_{\xi} = -log\left(\frac{N^{\xi}_{high}}{N^{0}_{high}}\right) + log\left(\frac{N^{\xi}_{low}}{N^{0}_{low}}\right) \tag{4.12}$$

where the the apex 0 refers to the non-attenuated beam and index ξ refers to a specific line integral across the sample.

Taking into account the Poisson nature of photons, the noise associated to each pixel of the image recording N photons is simply described by the Poisson statistics with $\sigma = \sqrt{N}$. Referring to eq. 4.12 the noise associated to the KES signal recorded in a homogeneous region of the image follows from the noise propagation rule:

$$\sigma_{KES_{\xi}} = \sqrt{\frac{1}{N^{\xi}_{high}} + \frac{1}{N^{0}_{high}} + \frac{1}{N^{\xi}_{low}} + \frac{1}{N^{0}_{low}}} \tag{4.13}$$

4.4.3 *Experimental setup, geometry, simulations and data acquisition*

To validate the simulation program, actual images of a test sample were acquired with the lab-setup.

The test sample was made by two pipettes filled two solution in water of the iodine-based contrast agent Bayern Ultravist®. One pipette was filled with a solution 50 mg/ml (iodine in water), the other with a solution 10 mg/ml (iodine in water). The pipettes were made by polypropylene with a measured thickness of 0.16 cm. The internal maximum diameter of the pipette to be filled with the solution was of 0.89 cm.

The settings of the X-ray source were the following: Voltage 40 kV, current 200 μA, filter 0.253 $mmCu$. The distance Source-Detector (D_{SD}) and Source-Object (D_{SO}) were respectively $D_{SD} = 30.5$ cm and $D_{SO} = 27$ cm, resulting in a magnification factor of about 1.13. The Pixirad-1/Pixie-iii was configured in NPISUM mode. The images were acquired with an exposure time of 4.5 s. In Figure 4.25 is reported a picture of the experimental setup.

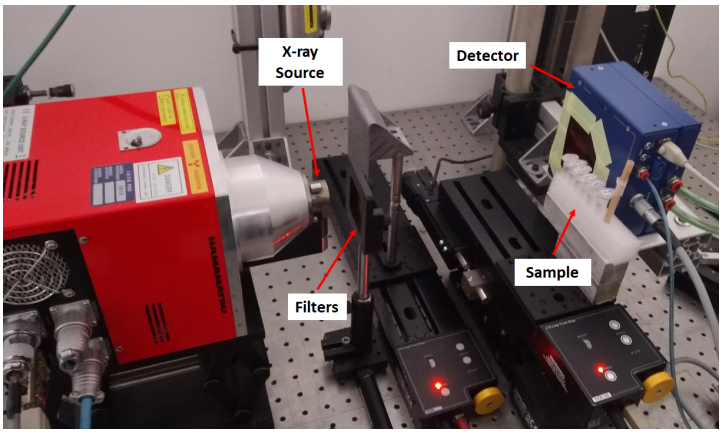

Figure 4.25: Experimental setup for planar imaging.

The experimental conditions described above were reproduced in the simulator. The performance of the Pixirad-1/Pixie-iii in terms of energy resolution at different energies were simulated by exploiting the characterization of the pixie-iii carried out in chapter 3. Of note, where not directly measured, the energy resolution of the simulated XPCD was estimated by performing a second order polynomial fit (as a function of the energy) of the energy resolutions reported in Table 3.2.

To validate the simulator, different sets of planar images were acquired/simulated for different threshold configurations. In particular, by fixing the thr_1, a threshold scan was performed by varying thr_2 at fixed steps. The threshold scan was repeated for different values of thr_1. The grid of threshold combinations used for the acquisitions is displayed in Figure 4.26

keV →

thr1 \ thr2	30	30.5	31	31.5	32	32.5	33	33.5	34	34.5	35	35.5	36	36.5	37	37.5	38
26.5	✓	✓	✓	✓	✓	✓	✓	✓	✓	✓	✓	✓	✓	✓	✓	✓	✓
27.5	✓	✓	✓	✓	✓	✓	✓	✓	✓	✓	✓	✓	✓	✓	✓	✓	✓
28.8	×	×	✓	✓	✓	✓	✓	✓	✓	✓	✓	✓	✓	✓	✓	✓	✓
30.5	×	×	✓	✓	✓	✓	✓	✓	✓	✓	✓	✓	✓	✓	✓	✓	✓
31.5	×	×	×	×	✓	✓	✓	✓	✓	✓	✓	✓	✓	✓	✓	✓	✓
31.5	×	×	×	×	×	×	✓	✓	✓	✓	✓	✓	✓	✓	✓	✓	✓

Figure 4.26: Grid of threshold combinations used for the acquisitions. The green ticks correspond to the performed acquisitions.

The threshold scans were performed to test the simulator response under different acquisition settings and, in particular, to test the ability of reproducing KES images with contrast, signal and CNR comparable with the experimental acquisitions using different threshold settings.

For each image of the sample, a flat field image with the same input statistics was acquired to produce radiographic projections.

To minimize the impact of the image processing in the resulting measurements, no image processing was performed for both the experimental and simulated images. Where necessary, the NaN and the infinity values present in the selected ROIs were ignored.

4.4.4 *Results*

In Figure 4.27 is reported an experimental KES image obtained with the thresholds $thr_1 = 26.5\ keV$, $thr_2 = 33\ keV$. For comparisons with the

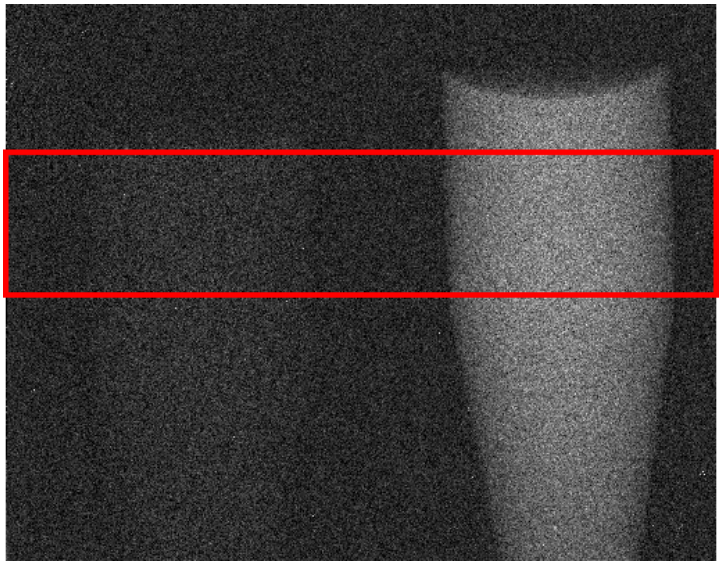

Figure 4.27: Experimental image acquired for $thr_1 = 26.5\ keV$, $thr_2 = 33\ keV$.

simulations, in the experimental images only the ROI (size 512×100), red box in figure 4.27, was considered. In fact, by isolating the region in which the pipettes have a cylindrical shape, the selected ROI allowed to simplify the simulation geometry.

For the same threshold settings, a comparison between the simulated image and the experimental one is shown in Figure 4.28: (a) experimental image; (b) simulated image; (c) plot of the horizontal profiles highlighted in the images for both simulated and experimental images. The results in Figure 4.28 show a good agreement in the signals of both the simulated and the experimental images. Of note, the profiles in Figure 4.28 (c) have been smoothed with the Savitzky-Golay filter [121] to better compare horizontal profiles.

To objectively evaluate the accuracy of the simulation program, measurements of the KES signal, noise and CNR were carried out for all the threshold combinations. By observing the plot of the horizontal profiles in Figure 4.28 it is also possible to note that only the highest contrast-agent concentration shows a clearly distinguishable signal. Therefore, the measurements were carried out considering only the pipette on the right filled with the 50 mg/ml solution.

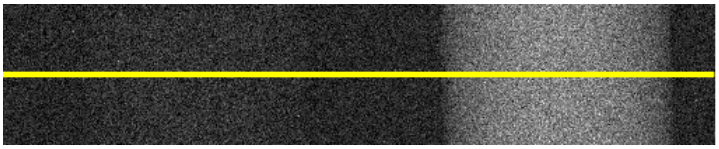

(a)

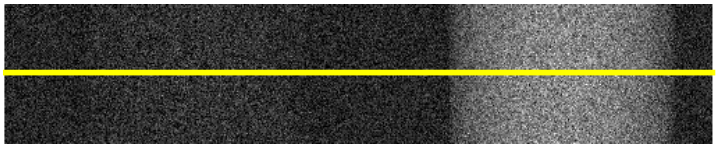

(b)

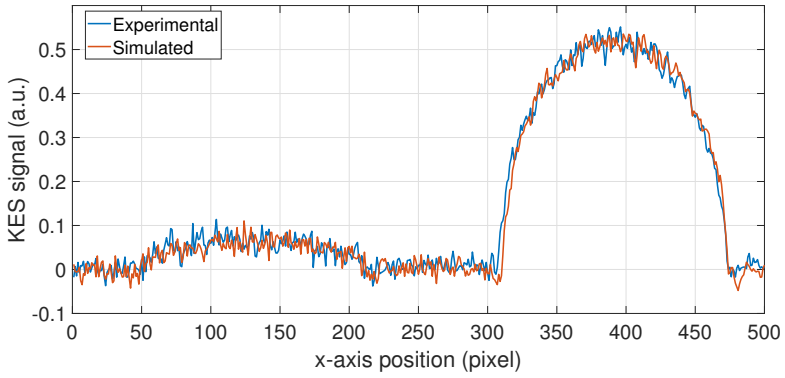

(c)

Figure 4.28: Comparison between experimental and simulated KES images for $thr_1 = 26.5\ keV$, $thr_2 = 33\ keV$: (a) experimental image; (b) simulated image; (c) plot of the horizontal profiles highlighted in the images for both simulated and experimental images.

To measure the CNR, 10 couples of ROIs (10×10) were selected respectively at the center of the pipette (ROI_p) and in a background region (ROI_b) as shown in Figure 4.29. Of note, the small size of the ROIs was set in order to minimize the effects of the circular shape of the pipette in the measure of the average and the noise of the signals. For each couple of ROIs the CNR was calculated as follows:

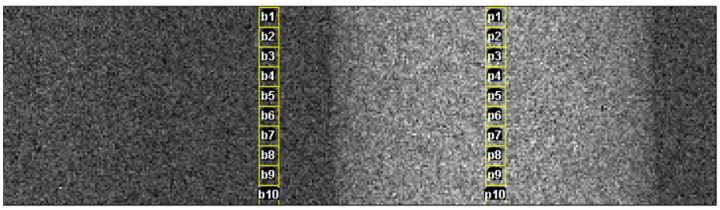

Figure 4.29: ROIs selection for CNR, contrast and noise measurements.

$$CNR = \frac{m_p - m_b}{\sqrt{\sigma_p^2 + \sigma_b^2}} \tag{4.14}$$

where m and σ are respectively the mean signals and the standard deviations recorded in ROI_p and ROI_b. To better compare the behaviors of the experimental images against the simulated ones, the contrast $C = \mu_p - \mu_b$ and the noise $\sigma = \sqrt{\sigma_p^2 + \sigma_b^2}$ were measured also separately. Finally, the average of 10 repeated measures of CNR, contrast (C) and noise (σ) were used; the standard deviations of the 10 repetitions were reported as statistical error.

In Figures 4.30, 4.31 and 4.32 are shown the plots of the CNR, the noise and the contrast measured on experimental/simulated images and with the analytical formula as a function of thr_2 for few fixed thr_1.

From the results in Figures 4.30, 4.31 and 4.31 it can be observed that the plots of the simulated CNR, contrast and the noise are in good agreement with the experimental data. This means that the simulator well reproduces the behavior of the experimental system. Slight deviations of CNR and noise from the experimental case are instead observed for the analytical formula. The deviations from the actual images become to be noticeable when thr_2 gets close to the endpoint of the spectrum (40 keV), or for high values of both thr_1 and thr_2 (e.g. Figure 4.31 (c)). Under these conditions, the energy bin 'high' is affected by a poor statistics that induces photon starvation in the actual images. The origin of deviations between the experimental/simulated case and the analytical formula can be, therefore, identified in the presence of NaN and infinity values (excluded from the measurements) occurring in both the experimental and simulated images when photon starvation occurs. As consequence of the underestimation of the noise, the CNR from the analytical formula is slightly increased if compared to the experimental case. Apart from the necessary clarification, it can

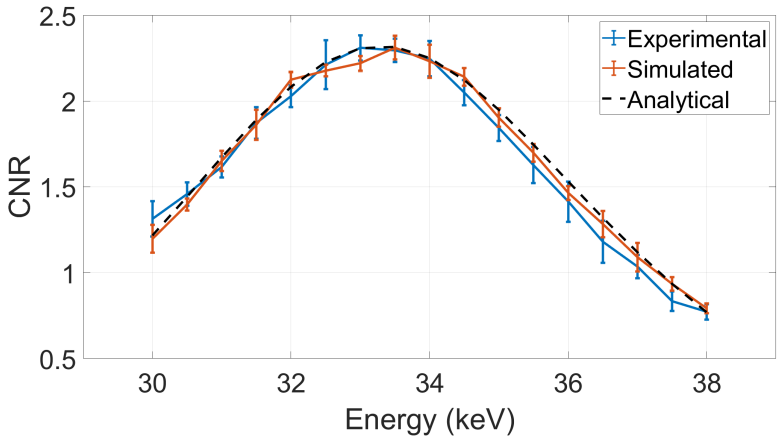

(a)

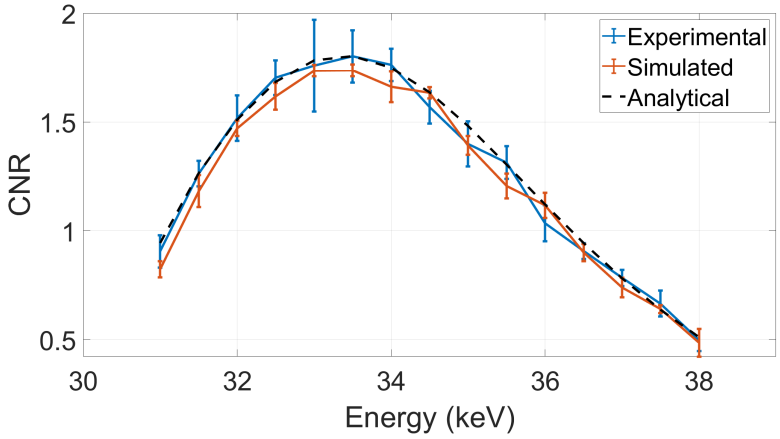

(b)

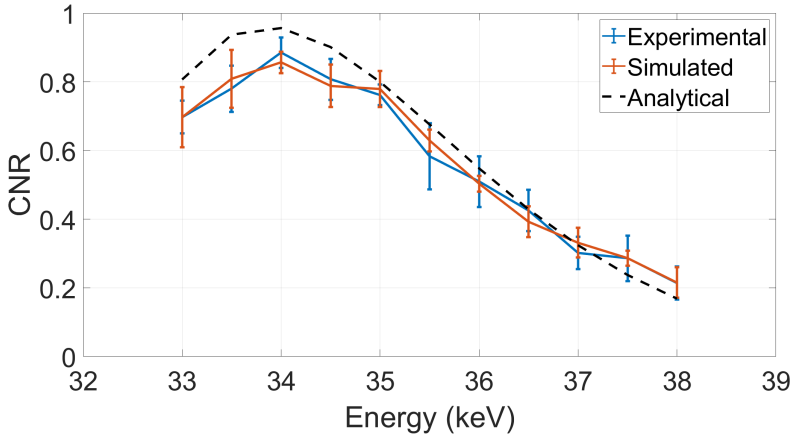

(c)

Figure 4.30: Plot of CNR as a function of thr_2 for few fixed thr_1: (a) $thr1 = 26.5\ keV$; (b) $thr1 = 30.5\ keV$; (c) $thr1 = 32.5\ keV$.

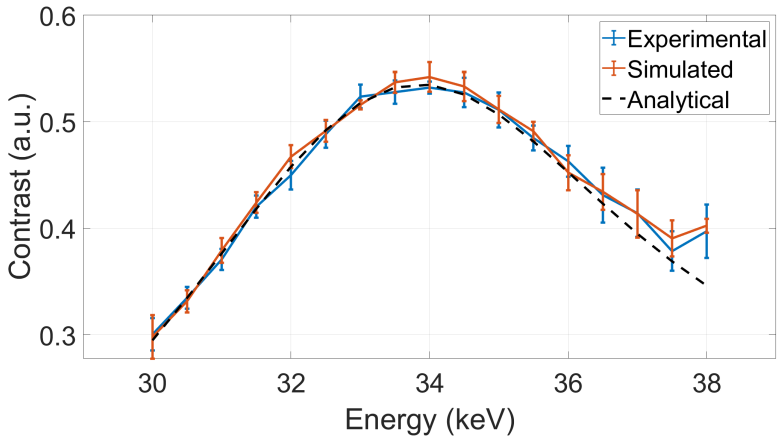

(a)

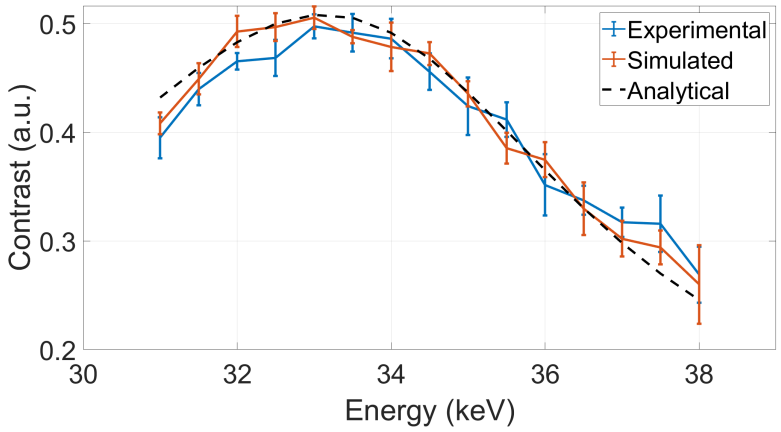

(b)

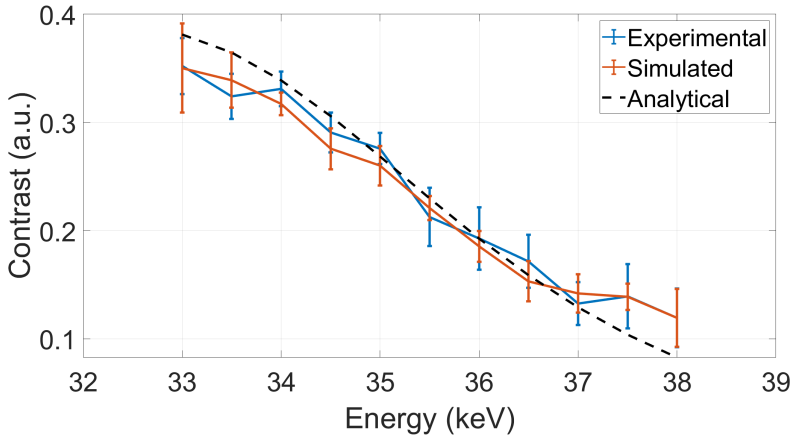

(c)

Figure 4.31: Plot of measured contrast as a function of thr_2 for few fixed thr_1: (a) $thr1 = 26.5\ keV$; (b) $thr1 = 30.5\ keV$; (c) $thr1 = 32.5\ keV$.

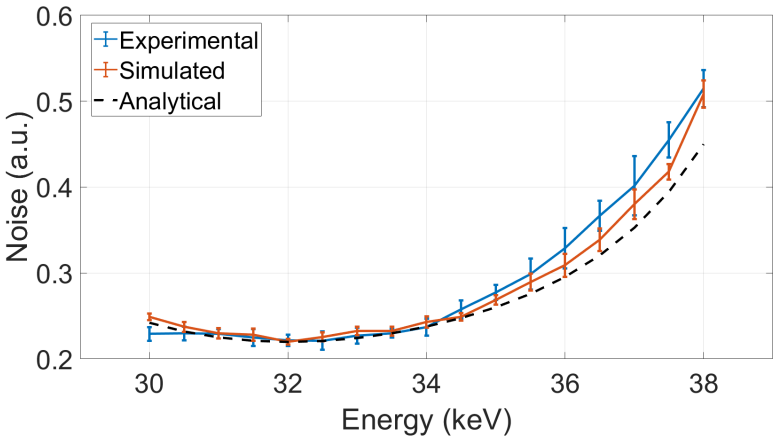

(a)

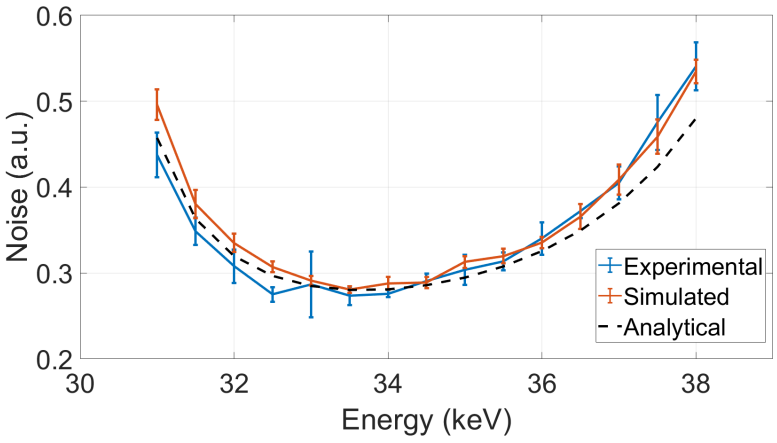

(b)

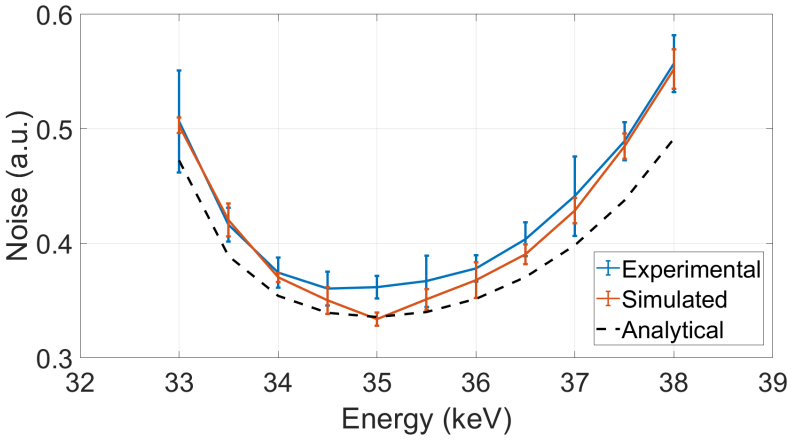

(c)

Figure 4.32: Plot of measured noise as a function of thr_2 for few fixed thr_1: (a) $thr1 = 26.5\ keV$; (b) $thr1 = 30.5\ keV$; (c) $thr1 = 32.5\ keV$.

however be concluded that in optimal experimental conditions (i.e. in the absence of photon starvation) both the analytical formula and the simulator are able to faithfully reproduce the experimental results.

For the sake of completness, in Figure 4.33 is shown the grid of the measured CNR for each threshold combination for both the experimental and the simulated images. More interestingly, the heatmaps

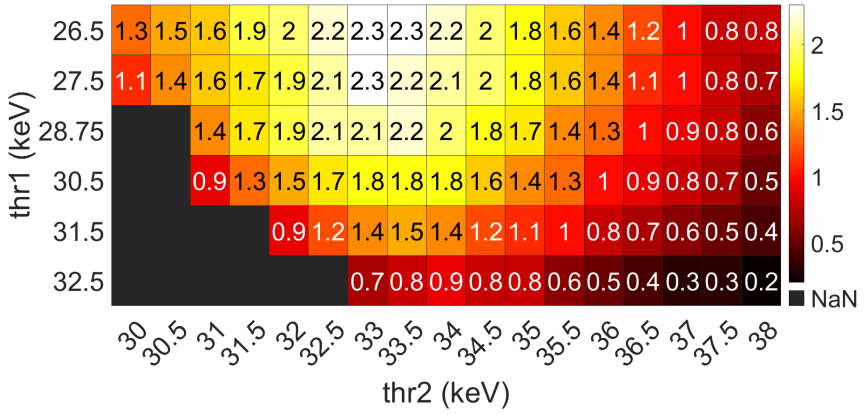

(a)

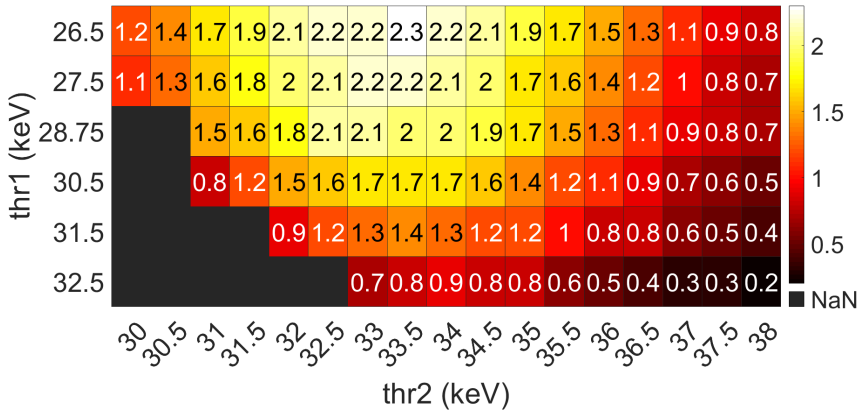

(b)

Figure 4.33: Grid of the measured CNR for each threshold combination: (a) experimental; (b) simulated.

in Figure 4.33 can be also used to identify the threshold settings that maximize the CNR in KES images. In particular, the brightest regions of the maps show the optimal thresholds. This implies that the simulator can be a valuable tool especially for optimization studies.

4.4.5 *Conclusions*

A simulator for reproducing the experimental images achievable with the lab-setup using the Pixirad-1/pixie-iii spectral XPCD has been implemented and validated.

The results showed that simulations and experimental images are in good agreement.

The simulation tool here developed can be employed for optimization studies. As an example, the simulator can be employed to find the settings for both the X-ray source (i.e. kV, filtration, current) and the XPCD (i.e. thr_1, thr_2) that maximize the CNR in KES images for a given contrast agent concentration.

The flexibility of the simulation tool allows also simulating extreme experimental conditions not always reproducible with the instrumentation available in lab. As an example, though the code has been limited to simulate an XPCD implementing two thresholds, it can be easily extended to the case of N thresholds. Alternatively, the performance of XPCDs with different spectroscopic capabilities and energy resolution can be compared.

4.5 TOWARDS 'IN VIVO' LOW DOSE KES IMAGING WITH POLYCHROMATIC SOURCE AND SPECTRAL XPCDS

When applying the image subtraction algorithm described in sect. 2.2.1, KES images feature positive signals in correspondence of structures filled with a contrast agent (embedding a K-edge element); negative or negligible signals in correspondence of other anatomical structures. For these images, image segmentation becomes therefore trivial and automatized, because a global gray level thresholding with a threshold t slightly above the background noise, such as e.g. $t > 3 \cdot \sigma$ where σ is the standard deviation of the gray levels in a background region-of-interest ROI, gives adequate results.

In medical imaging the KES technique is meant mainly to ease segmentation and further morphological quantification. This is beneficial for example in the 3D visualization of the vascular system of small animals [128, 129, 130]. For a detailed morphological quantitative analysis of the vascular tree, it is necessary to reconstruct the vascular network in its entirety and a binary segmented volume is required to quantify e.g. the vessel length and caliber in order to characterize a small artery occlusion and compression [129]. When considering the CT case, due to the inherent amount of noise and artifacts of XPCDs, it might be hard to segment the KES image if a conventional gray-level tomographic reconstruction with subsequent thresholding is applied. In this case and especially for low dose applications, discrete tomography could be beneficial as it focuses on the reconstruction of objects that consist of only a few different materials. Ideally, a CT reconstruction of such a sample should contain only one gray level for each of its components. By exploiting this property within the reconstruction algorithm, the produced images typically contain fewer artifacts since gray levels are concentrated towards a limited number of values or strictly enforced towards only two gray values, so to ease the separation of the back-

ground from the features of interest. Thanks to this, a limited number of projections is usually enough to produce adequate images and this in principle favors a reduction of the delivered radiation dose or the acquisition time.

This section presents the potentials of discrete reconstruction technique looking toward low dose single-shot KES-CT imaging with spectral XPCDs. The state-of-the-art discrete tomography [131, 132] reconstruction algorithm named total variation regularized-discrete algebraic reconstruction technique (TVR-DART) [133] was employed. In order to verify the performance of the lab-setup implemented within the KEST collaboration, the localization of clusters of barium nanoparticles in a breast cancer mouse model was considered. Breast cancer is the most common cancer in women worldwide and nanoparticles can enhance the contrast for further imaging. In addition, it is speculated that nanoparticles might enhance the efficiency of radiation therapy, due to their x-ray absorbing characteristics, which can increase the local radiation dose while lowering undesired dose deposition [134].

The quantification of *Ba* nanoparticles in a breast cancer mouse model here reported was validated against a reference image acquired at a synchrotron radiation source. The final result was an effective lab-based technology for an automated 3D mapping of a specific element.

4.5.1 *Samples*

In this optimization work, three samples were employed: two test-samples and one biological sample.

test-sample

Three different polypropylene 350 μl small tubes were prepared: one filled with an Iodine-based solution (Bayern Ultravist-93 $mg\ ml^{-1}$), a second one filled with a $BaCl_2$ (Carlo Erba Reagents- 122 $mg\ ml^{-1}$) solution and another one filled with de-ionized water. The K-edge value for I is 33.2 keV and for Ba is 37.4 keV. This simple test object was first considered to optimize the values of the detector energy thresholds by analyzing simple planar radiographic images. A sketch of this test object is reported in figure 4.34. Then a second test object composed of polypropylene 350 μl small tubes filled with different dilutions of $BaCl_2$ (Carlo Erba Reagents) and de-ionized water was prepared. It was designed to be considered for CT imaging in order to assess the minimum detectable concentration of Ba. A sketch of this second test object with the considered dilutions of $BaCl_2$ with water is reported in figure 4.35

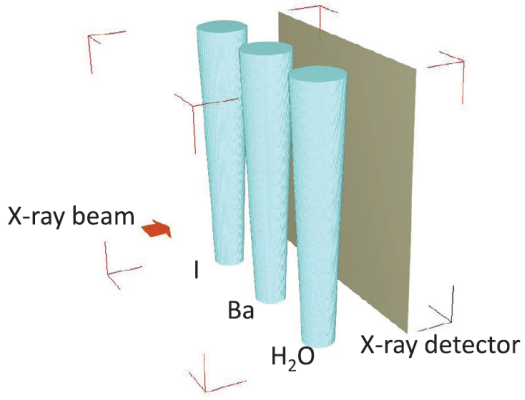

Figure 4.34: Sketch of the test object used to optimize the settings of the detector energy thresholds by considering planar radiographs. It is composed of three pipettes filled with: an I-based (Bayern Ultravist-93 $mg\ ml^{-1}$) solution; a $BaCl_2$ (Carlo Erba Reagents-122 $mg\ ml^{-1}$) solution and a reference small tube filled with deionized water. (Ba K-edge = 37.4 keV, I K-edge = 33.2 keV).

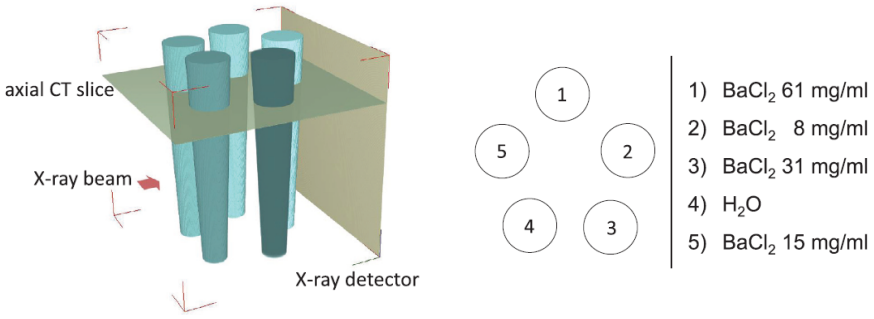

(a) (b)

Figure 4.35: (a) Sketch of the test object prepared for CT imaging and used to assess the minimum detectable concentration of Ba. (b) Order and composition of the considered pipettes as will result from an axial CT slice.

biological-sample

The biological sample employed in this work was a mouse model of breast cancer prepared by dr. Christian Dullin and his group at the Institute for Diagnostic and Interventional Radiology, University of Göttingen. The tumor growth was induced by the injection of 1×106 H8N8 breast cancer cells directly into the breast tissue of a female WAP-T mouse [135]. The mouse has been sacrificed 4 weeks after injection of the tumor cells. Barium nanoparticles were injected directly into the tumor one day before sacrificing the mouse. The tumor and the surrounding tissue were excised, fixated and embedded in a standard paraffin block commonly used for histological analysis. All animal procedures were performed in accordance with European guidelines (2010/63/ EU) and approved by the corresponding ethics institutions (administration of Lower Saxony, Germany, license No. 33.9-42502-04-18/3022).

4.5.2 *Synchrotron radiation μ-CT acquisition and reconstruction*

Synchrotron radiation (SR) imaging was performed at ID17 beamline of the European Synchrotron Radiation Facility (ESRF, Grenoble—France) in order to take advantage of a high flux X-ray beam monochromatized thanks to a double Si(1,1,1) Laue monochromator [89]. Monochromatic settings at 36.5 keV and 38.5 keV, respectively were applied for the KES-CT image acquisition. A CMOS PCO-edge 5.5 camera (detector pixel size = 6.5×6.5 μm^2), suitable for quantitative imaging [136], was used in combination with a 1:1 optics [137]. The exposure time was 50 ms and 2.000 projections were collected. Parallel beam filtered back projection reconstruction was applied to get the reconstructed volume at a voxel size of $6.5 \times 6.5 \times 6.5 \mu m^3$. The high-resolution volume will be further used in future studies where a comparison with histology will be performed. In this application, it was downscaled with averaging to produce a high-quality reference image having a nominal voxel size of $52 \times 52 \times 52 \mu m^3$, ready to further registration and comparison with the lab-based image. A ROI of the registered image is reported in Figure 4.36 together with its segmentation by thresholding.

4.5.3 *KES-CT laboratory imaging: geometry, pre-processing and reconstruction*

With the lab-setup, the parameters used in the cone-beam CT geometry were: distance source-to-object $D_{SO} = 200$ mm, distance source-to-detector $D_{SD} = 250$ mm, 720 projections over 360 degrees in 'step and go' mode with 10 repetitions per angle. The inherent magnification

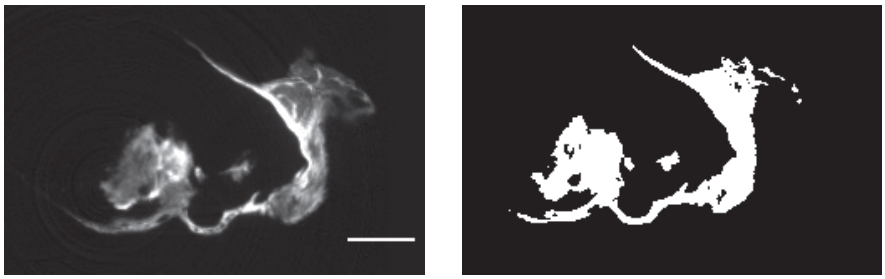

(a) (b)

Figure 4.36: ROI of the (a) registered SR-KES reference image and (b) its segmentation. The considered gray level threshold was computed as the $t = 5\sigma$ where σ was the standard deviation of the gray levels in the background. (Scale bar 2 mm).

of the cone beam geometry resulted in a nominal voxel size of the reconstructed images of approximately $50 \times 50 \times 50 \mu m^3$.

Since 10 repetitions were collected, three different datasets were derived in order to simulate different acquisition statistics. In a first case, the 10 repeated images were averaged. In the second case, only 5 images were considered for the averaging. A single image (no averaging) was also considered for a third 'low statistics' dataset. Similarly, to simulate different angular sampling, projections were decimated to a factor 4 (i.e. 180 projections) and 12 (i.e. 60 projections), respectively. Thus, in total, 9 different acquisition protocols were considered.

For each dataset, the images were processed and reconstructed as described in sect 4.2.

4.5.4 *Image comparison*

The SR reference image (having nominal voxel size of $52 \times 52 \times 52 \mu m^3$) has been co-registered (affine registration) with respect to the proposed lab-based CT volume reconstructed with FDK having nominal voxel size of $50 \times 50 \times 50 \mu m^3$, in order to propose a voxel-by-voxel quantitative comparison. As mentioned in the introduction, the global gray level threshold has been set to $t = 3\sigma$ where σ is the standard deviation of the gray levels in a background ROI. Figure 4.36 reports this reference image. After that the segmentation error has been evaluated by assessing the number of true positives (TP), false positives (FP) and false negatives (FN) with respect to the SR reference thresholded image. These values were combined in the Jaccard index:

$$\epsilon = \frac{TP}{TP + FP + FN} \tag{4.15}$$

Referring to eq. 4.15, it is worth noticing that, by definition, the Jaccard index is limited in the range $0 \leq \epsilon \leq 1$. In particular, $\epsilon = 1$ for an

ideal case where no FP and FN occur. Conversely, with the increase of FP and/or FN, ϵ decreases towards zero.

4.5.5 *Discrete reconstruction*

Discrete reconstruction is a technique that solves the reconstruction problem of sample that consist of a limited number of materials, each of them producing a constant gray value in the reconstruction. Discrete approaches are particularly useful for low dose applications, where only a few noisy projections are available for CT reconstruction [133]. However, since the most of biological samples feature complex details and do not simply contain a few homogeneous regions, discrete reconstructions can be effectively applied only to a limited number of specific applications. One of these applications is the KES imaging technique, where the sample can be assumed to be made of two homogeneous materials, i.e. the contrast agent and the background [132].

In this work, discrete reconstruction with the TVR-DART (Zhuge et al 2016) algorithm was applied to the proposed lab-based KES image. The code publicly available here: `https://github.com/astra-toolbox/ContributedTools` was used. TVR-DART is capable of providing more accurate reconstruction than existing algorithms under noisy conditions from a small number of projection images and/or from a small angular range [133]. Non-negativity constraints were added in order to get at the end a reconstructed volume where non-zero voxels represent the map of Barium in the considered sample.

As done for the conventional reconstruction, 9 different acquisition protocols were considered. The amount of non-zero voxels has been quantified and a segmentation error was determined against the thresholded SR reference image for each of the considered datasets. Again, the the number of TP, FP, and FN, as well as ϵ were determined.

4.5.6 *Results*

Figure 4.37 reports two different planar KES images of the test object used for the optimization of the values for the detector energy thresholds. It can be easily noticed that different detector settings produce different KES images with the same input X-ray spectrum.

In this work, the maximization of the KES signal was used as the criterion for the selection of the energy thresholds. The following settings result in a reasonable trade-off for the detection of Ba: X-ray tube voltage $V = 50\ kV$, current = $160 \mu A$, 1 $mmAl$ filter, exposure time = 1 s, detector energy thresholds $thr_1 = 28.0\ keV$, $thr_2 = 38.0\ keV$. The X-ray spectrum as produced by the considered X-ray tube was first simulated via SpekCalc [138, 139, 140]. An experimental measure was performed by means of a CdTe Amptek X-ray spectrometer in order

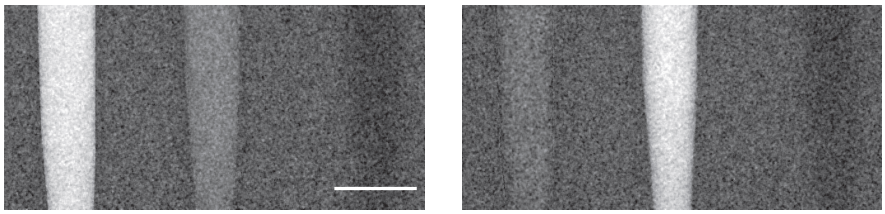

(a) (b)

Figure 4.37: KES (flat-corrected) projections of the considered test object composed of small tubes filled with a solution of I, Ba and H_2O (see figure 4.34). For both images the X-ray source settings were the same, i.e. voltage = 50 kV and 1 mm of Al filter. The detector energy thresholds were: (a) $thr_1 = 28.0\ keV$, $thr_2 = 33.5\ keV$; (b) $thr_1 = 28.0\ keV$, $thr_2 = 38.0\ keV$. (Scale bar 5 mm)

to validate the simulation. Unlike the simulated one, the recorded spectrum is affected by the Cd and Te K-edges, thus better representing the expected behaviour of Pixie-iii. Results are reported in Figure 4.38 (a). The simulation gives an estimated entrance dose of 0.176 mGy at the sample per collected radiograph with the considered setup.

The value for thr_1 should be, in principle, close enough to the value of thr_2 but an adequate photon statistics is required in the 'low' image and therefore it has to be shifted towards lower energies. In this work $thr_1 = 28\ keV$ was assumed as set. Its position was not fine tuned, being less critical than thr_2. The values for thr_2 result from the optimization presented in Figure 4.38 based on a so-called threshold scan, i.e. different acquisitions with the same thr_1 value and increasing thr_2 values. The resulting KES images were analyzed by considering a ROI within the Ba small tube. The thr_2 value for which the ROI average value resulted maximum was chosen as optimal value. Due to the finite energy resolution of the detector, different criteria for the positioning of thr_2 might be adopted. Instead of maximizing the KES signal, a slight shift of thr_2 towards higher (or lower) energies might be preferred in order to avoid contamination with materials having a K-edge lower than (or higher than) the target material.

Figure 4.39 reports an axial slice of the test object used for CT imaging and to assess the minimum detectable concentration of Ba. The images result from the acquisition protocol with the highest statistics (projection averaging over 10 image and 720 projections). The advantages for further image segmentation and quantification are visible in the KES image where only Ba contents give a positive gray-value and all the other elements become indistinguishable from the background (the latter having ideally gray level 0). Although a fine assessment of the minimum detectable concentration of Ba goes beyond the purposes of this work, it is implicit that a localization of Ba contents above a certain concentration is feasible with the proposed

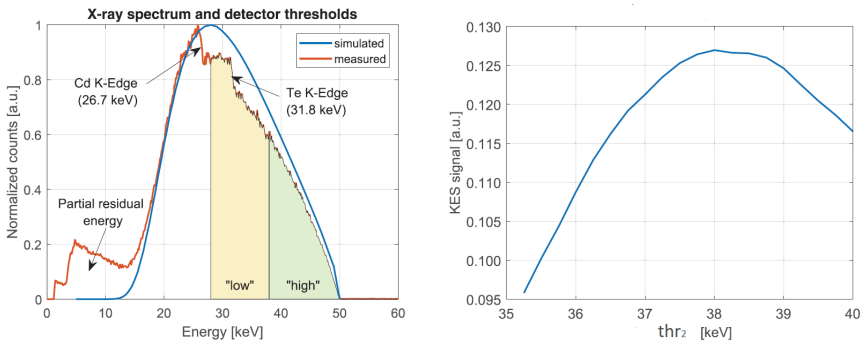

(a) (b)

Figure 4.38: (a) Plot of the considered X-ray spectrum with superposition of the adopted detector energy thresholds. (b) Plot of the CNR of the different planar KES images by considering different values for the detector thr_2 energy threshold. A ROI within the *Ba* small tube and a ROI within the background have been considered for the computation of the CNR.

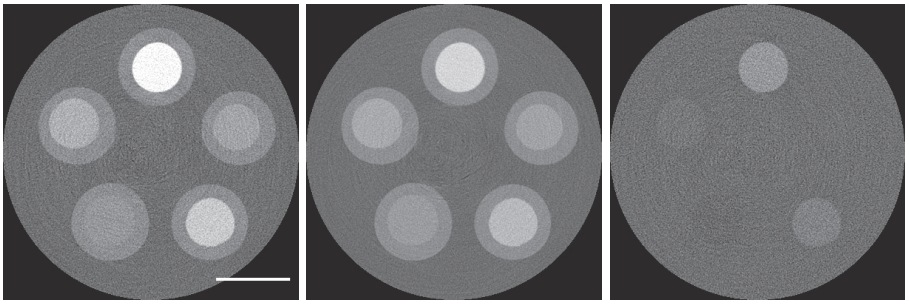

(a) (b) (c)

Figure 4.39: Tomographic axial slice (512×512 pixels) of the considered test object for CT (see Figure 4.35): (a) low-energy image; (b) high-energy image; (c) resulting KES image where only the *Ba* content within the small tubes results highlighted. Resulting isotropic voxel size is $50 \times 50 \times 50 \mu m^3$. The same window/level gray-value settings are used for the three images. (Scale bar 5 *mm*).

settings. It is also reasonable to infer that with higher photon statistics also much lower concentrations of *Ba* can be identified.

Figure 4.40 shows a ROI of an axial slice of the lab-based KES images by considering different acquisition statistics. These gray level images can be visually compared with Figure 4.36 (a) where the reference SR (downscaled and registered) KES image is presented. Although a good agreement with the reference image can be visually noticed, a quantitative comparison is required to better comment the differences. The images reported in figure 4.40 have been segmented via thresholding with threshold $t = 3\sigma$ where σ is the standard deviation of the gray levels in a background ROI. Then, a segmentation error has been evaluated.

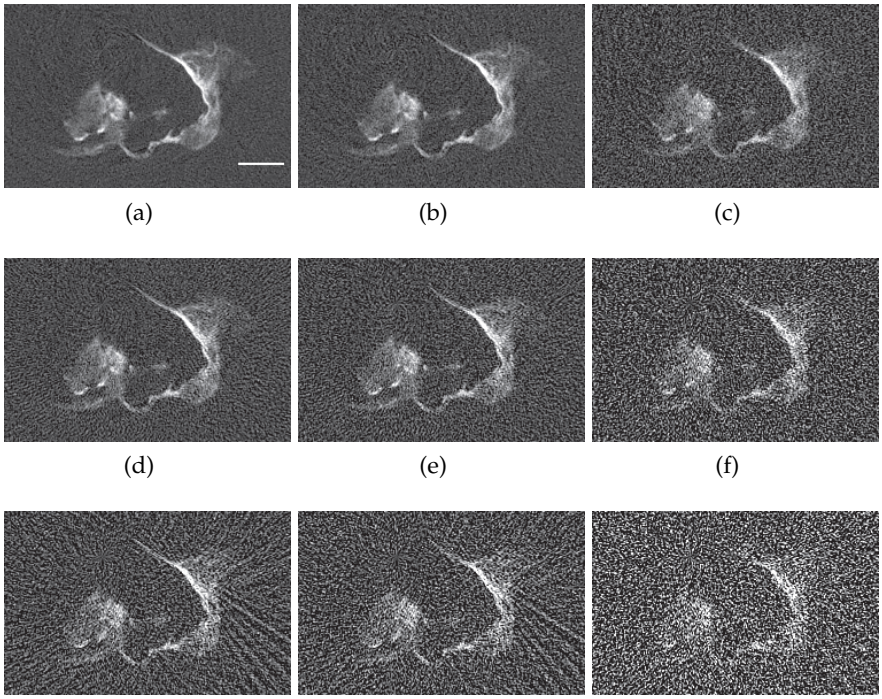

(a) (b) (c)

(d) (e) (f)

(g) (h) (i)

Figure 4.40: ROI of an axial slice of the KES image of the considered biomedical sample reconstructed with conventional FDK when using: (first row—(a)–(c)) 720 projections; (second row—(d)–(f)) 180 projections; (third row—(g)–(i)) 60 projections and (first column—(a), (d), (g)) projection averaging with 10 images; (second column—(b), (e), (h)) projection averaging with 5 images; (third column—(c), (f), (i)) no projection averaging. The reduction factor of the total photon flux with respect to the dataset with highest statistics is reported in each subcaption. (Scale bar 2 *mm*).

Figure 4.41 reports the segmented images and Table 4.6 presents the results of the quantitative comparison with the reference SR image (Figure 4.36 (b)).

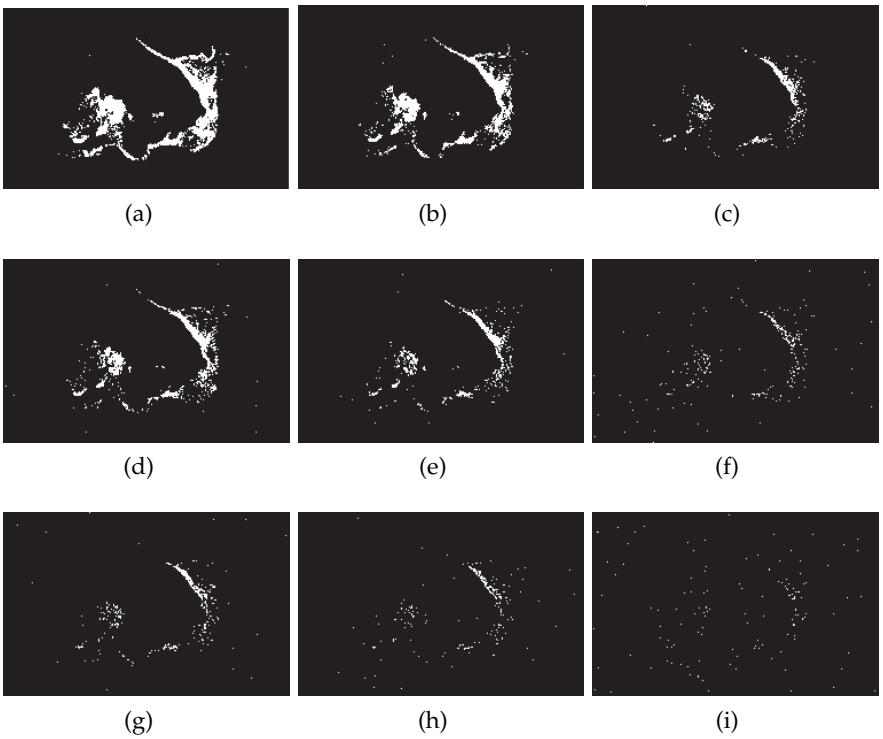

Figure 4.41: ROI of an axial slice of the KES image of the considered biomedical sample after conventional FDK reconstruction and thresholding with threshold $t = 3\sigma$ where σ is the standard deviation of the gray levels in a background ROI. The segmentation was performed on the FDK reconstructed images when using: (first row—(a)–(c)) 720 projections; (second row—(d)–(f)) 180 projections; (third row—(g)–(i)) 60 projections and (first column—(a), (d), (g)) projection averaging with 10 images; (second column—(b), (e), (h)) projection averaging with 5 images; (third column—(c), (f), (i)) no projection averaging.

	TP (%)	FP (%)	FN (%)	ϵ
Averaging over 10				
720 proj.	7.08	0.47	4.34	0.60
180 proj.	3.68	0.23	7.75	0.32
60 proj.	0.80	0.03	10.62	0.07
Averaging over 5				
720 proj.	4.45	0.15	6.97	0.38
180 proj.	1.98	0.09	9.44	0.17
60 proj.	0.36	0.01	11.06	0.03
No averaging				
720 proj.	1.72	0.06	9.70	0.15
180 proj.	0.28	0.02	11.14	0.02
60 proj.	0.02	0.01	11.41	0.01

Table 4.6: Quantitative analysis of the FDK plus thresholding images compared (Figure 4.41) to the SR reference image (Figure 4.36 (b)).

The results presented in Table 4.6 show the difficulties of an automated segmentation with threshold $t = 3\sigma$ (where σ is the standard deviation of the gray levels in a background ROI) when reducing the acquisition statistics.

The values for the Jaccard index (eq. 4.15) decrease coherently with the reduction of the statistics. It is worth noticing that these values are far from 1 even for the highest statistic image. This is due to the fact that subtle concentrations of Ba are identified in the ground truth SR image thanks to its extremely high spatial, contrast and energy resolution. These concentrations are hidden by the background noise in the lab-based images. Moreover, the quantitative values are worsened by the unavoidable image registration process required by this voxel-by-voxel quantitative comparison. It is implicit that other reconstruction algorithms such as iterative approaches might have been considered since they are widely recognized as beneficial in the case of high noise and sparse views. However, many of these require the fine tuning of one or more regularization parameters and/or a proper assessment of the number of iterations. These aspects are in general application-dependent.

In order to go towards a low-dose localization of a specific element, the TVR-DART algorithm has been applied to the considered datasets. Figure 4.42 reports the same ROI for a reconstructed image (direct binary reconstruction) when considering the different acquisition protocols. The results of the quantitative comparison with the reference

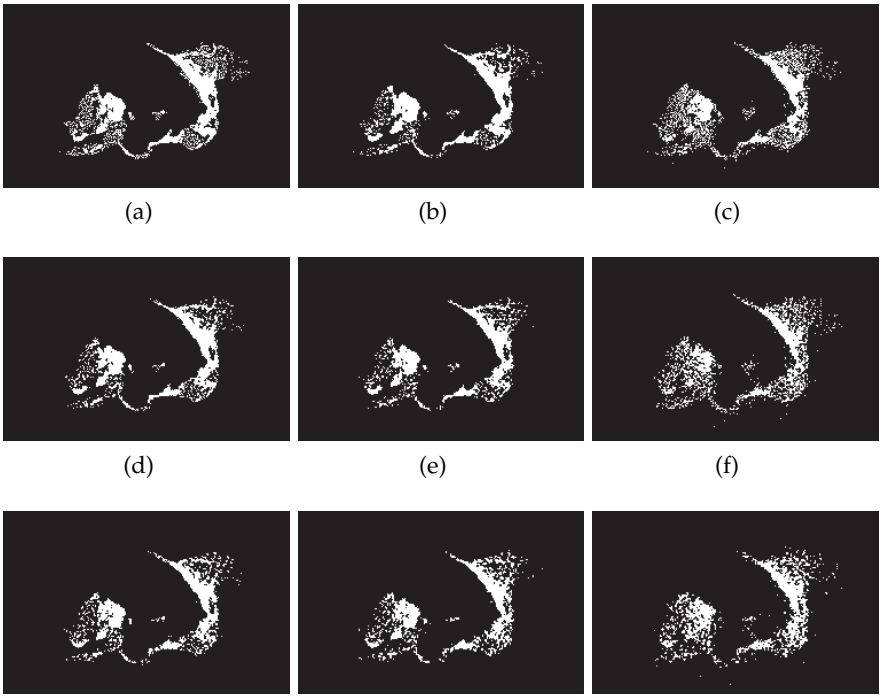

Figure 4.42: ROI of an axial slice of the KES dataset reconstructed with TVR-DART (direct binary reconstruction) when considering: (first row—(a)–(c)) 720 projections; (second row—(d)–(f)) 180 projections; (third row—(g)–(i)) 60 projections and (first column—(a), (d), (g)) projection averaging with 10 images; (second column—(b), (e), (h)) projection averaging with 5 images; (third column—(c), (f), (i)) no projection averaging.

SR image (Figure 4.36 (b)) are presented in table 4.7.

	TP (%)	FP (%)	FN (%)	ϵ
Averaging over 10				
720 proj.	6.67	1.62	4.75	0.51
180 proj.	6.98	2.16	4.44	0.51
60 proj.	6.15	0.76	5.28	0.50
Averaging over 5				
720 proj.	6.81	1.89	4.62	0.51
180 proj.	6.07	0.47	5.35	0.51
60 proj.	7.59	1.08	3.84	0.61
No averaging				
720 proj.	6.41	1.38	5.02	0.50
180 proj.	6.06	1.21	5.36	0.48
60 proj.	6.77	1.46	4.66	0.53

Table 4.7: Quantitative analysis of the TVR-DART images (Figure 4.42) compared to the SR reference image (Figure 4.36 (b)).

It can be noticed that the values for the Jaccard index fluctuates around an average value when considering all the TVR-DART cases from 720 projections with averaging to the volume reconstructed with 60 angles and without projection averaging. This confirms that TVR-DART is a robust discrete tomography reconstruction method and it performs adequately also when a reduced number of projections is considered.

With the proposed laboratory system based on a conventional X-ray source and the Pixie-iii detector, KES imaging is possible and, above a certain concentration, a reliable localization and quantification of a contrast medium is feasible. The performances of the polychromatic KES approach are inferior to those of synchrotron radiation imaging, but the single-shot lab-based nature of the proposed system is a key advantage for all the practical applications where motion artifacts and radiation dose are a concern. When the final goal is a binary map where only the contrast agent results highlighted, lab-based KES imaging combined with discrete tomography is a promising valuable tool. Among the others, TVR-DART was chosen for its automatic parameter estimation property. The only parameter that has to be specified is the number of materials to identify which is always 2 (element and background) for the case of KES imaging. This state-of-the-art parameter-free discrete reconstruction algorithm allows for a significant reduction of the number of acquired projections. This,

in addition to the single-shot approach, suggests that a low-dose 3D mapping of a contrast agent is in principle possible. In this work, considering the simulated entrance dose per projection, a total of 10.6 *mGy* was estimated for the case of the dataset with lowest statistics (60 projections). Therefore, it is reasonable to state that 'in vivo' applications could be conceived.

4.5.7 *Conclusions*

K-Edge Subtraction (KES) tomographic imaging using lab-based polychromatic sources and photon counting detectors is attractive, since conventional x-ray tubes can be considered instead of e.g. synchrotron sources.

Provided that an XPCD with at least two counters (or thresholds) is available, a single-shot low-dose approach is feasible. This leads to perfectly co-registered images and potential in vivo applications without motion artifacts and the need of image registration.

The energy resolution of the Pixie-iii detector was found to be adequate for practical applications such as the volume quantification of clusters of Ba-nanoparticles in a breast cancer mouse model. Although limitations in image quality of CdTe photon-counting detectors still remain, a fundamental contribution comes from refined image preprocessing and discrete reconstruction. An easy-to-access lab-based technology for a routine 3D elemental mapping of a contrast medium ready for further morphological quantification is therefore available.

5

SPECTRAL IMAGING WITH BENT-LAUE MONOCHROMATOR CRYSTALS

As introduced in sect 2.3.3, by exploiting the focusing properties of asymmetrically cut bent-Laue crystals it is possible to prepare a polychromatic spectrum with energy dispersion ΔE focused at the sample. This setup is suitable for spectral imaging applications with one or more contrast agents. In this context, the KISS collaboration aims at implementing different crystal setups optimized for a wide range of elements with K-edges within the diagnostic energy window used in medical imaging; from the conventional xenon, iodine, barium, gadolinium based contrasts agent to non-conventional contrast agents based on silver or gold nanoparticles of particular interest for theranostics purposes [134, 141].

For a given energy range of interest, the focusing and energy dispersive properties of bent-Laue crystals depend on the physical characteristics of the crystal employed. Therefore, for each task a properly cut crystal needs to be employed in the imaging setup.

After introducing the physics underlying the bent-Laue crystal optics, this chapter presents the acquisition setup for spectral imaging with bent-Laue crystals developed within the KISS collaboration. In particular, preliminary results of a bent-Laue setup optimized for K-edge imaging at the K-edge energies of Niobium and Molybdenum are presented.

5.1 PHYSICS OF CRYSTAL OPTICS

A crystal is a solid where the atoms or molecules are arranged in a repetitive periodic lattice. The smallest portion of the crystal lattice that characterizes the three dimensional pattern of the whole crystal is called unit cell.

The crystalline lattice is a mathematical abstraction essentially described by three basis vectors called primitive translation vectors. In this mathematical formulation, the characteristics of interest for a crystal can be described by the orientation of the crystalline planes and the spacing (d) between the planes. The direction of the planes in an unit cell are identified by a 3D vector (h, k, l), where h, k and l are called Miller indices. In this notation, for a cubic cell with side a_0, the distance between the crystalline planes (d_{hkl}) is defined as follows:

$$d_{h,l} = \frac{a_0}{\sqrt{h^2 + k^2 + l^2}} \tag{5.1}$$

As an example, in Figure 5.1 are shown few planes identifiable in a cubic unit cell.

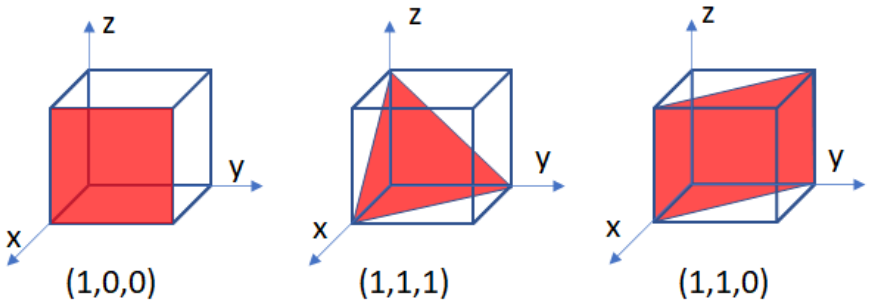

Figure 5.1: Examples of the planes in a cubic cell identified by (1,0,0); (1,1,1) and (1,1,0) vectors.

Thanks to their periodically organized structure, crystals can be exploited as X-ray optics. In particular, when the X-ray radiation has a wavelength λ comparable to the atomic spacing of a given crystalline structure, the radiation scattered by the atoms of the crystalline system undergoes destructive and constructive interference. The Bragg's law describes the particular condition for which the constructive interference occurs and it is mathematically described by the following expression:

$$n \cdot \lambda = 2d_{h,k,l} \sin\theta_B \tag{5.2}$$

where θ_B (Bragg's angle) is the angle for which the constructive interference occurs. The physical meaning of eq. 5.2 can be explained as follows: given an X-ray beam incident to a crystal, the diffused radiation by a crystalline lattice interfere constructively only if the difference of the optical path is an integer number of wavelength λ. A schematic of Bragg's law is reported in Figure 5.2.

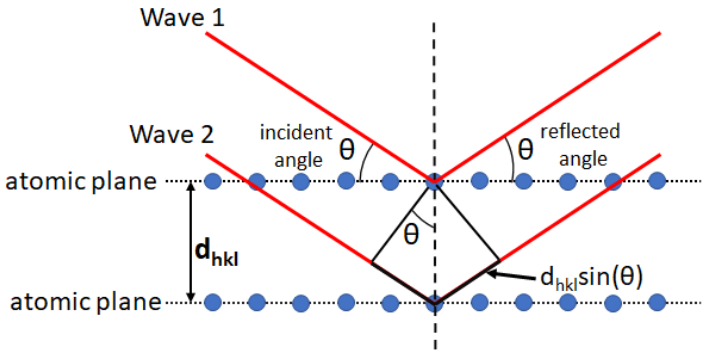

Figure 5.2: Schematic of Bragg's law: incident X-rays are elastically scattered by the crystalline lattice. The difference of the optical path of two scattered rays by two contiguous planes is $2d_{hkl}\sin(\theta)$, where d_{hkl} is the lattice spacing and θ is the angle of incidence on the crystalline planes.

Thanks to their good mechanical and thermal properties as well as their availability and accessible costs, Si crystals are commonly employed as X-ray optical elements. The unit cell of Si crystals is the so-called diamond cubic face centered shown in Figure 5.3, with side $a_0 = 5.431$ Å.

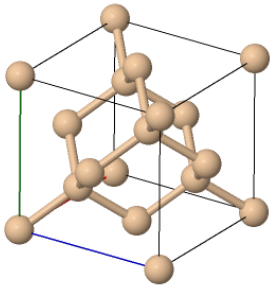

Figure 5.3: Diamond cubic face centered crystalline structure. Source http://lampx.tugraz.at/~hadley/memm/materials/silicon/silicon.php

Crystal optics are employed in two main geometries: Bragg and Laue. In the first geometry, the diffracted X-ray beam exits from the same surface of incidence; in the latter geometry, the diffracted X-ray beam is transmitted through the crystal surfaces. The two geometries are shown in Figure 5.4.

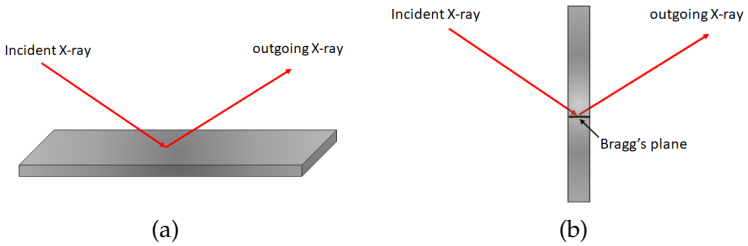

Figure 5.4: Crystal optics geometries: (a) Bragg; (b) Laue.

In both Laue and Bragg geometries, the crystal can be flat or bent according to the specific task. As an example, flat crystals are usually employed to produce monochromator systems with high energy resolution, such as e.g. double crystal monochromator systems. On the other hand, bent crystals are usually preferred for applications that require high reflectivity and homogeneous response, or when the energy dispersion of the crystal needs to be adjusted [142].

5.1.1 *Bent-Laue geometry*

A thorough mathematical description of bent-Laue crystal properties can be found in literature [143, 51, 144, 145, 54, 146, 59, 55, 56, 147, 148].

In this section, the main properties of bent-Laue crystals described in the cited literature are briefly introduced.

The physics of a bent crystal in the focusing geometry is well described by the lamellar model [144]. In this model, a bent crystal is idealized as a stack of crystal lamellae which have a gradually changing orientation corresponding to the curvature of the crystal [144]. With this model two foci can be identified: the single ray (polycromatic) focus (f_p) and the geometrical (monochromatic) focus (f_g). The single ray focus is the point where the diffracted rays from a single polychromatic beam are focused (Figure 5.5 a); the geometrical focus (f_g) is the point in which the monochromatic rays, diffracted according to the Bragg's law, are focused (Figure 5.5 b).

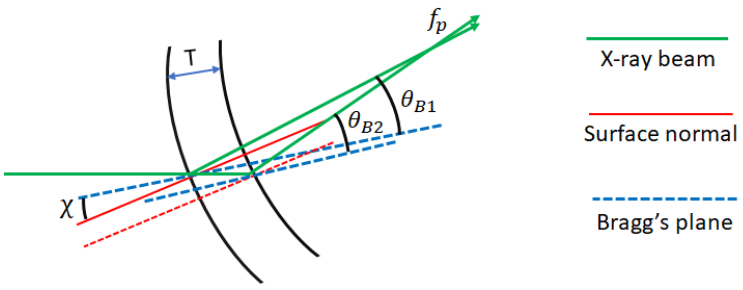

(a)

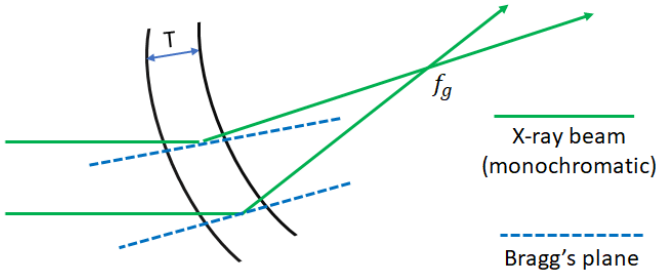

(b)

Figure 5.5: (a) single ray focus (polychromatic); (b) geometrical focus (monochromatic).

The two foci can be described by the following mathematical expressions:

$$f_g = \frac{F_1 R cos(\chi - \theta_B)}{2F_1 + R\cos(\chi + \theta_B)} \tag{5.3}$$

$$f_p = \frac{R\sin(2\theta_B)}{2\sin(\chi + \theta_B) + (1+\nu)\sin(2\chi)cos(\chi + \theta_B)} \tag{5.4}$$

where ν is the Poisson's ratio, which is a characteristic of the crystal composition, orientation (h,k,l) and mechanical stress [149, 150]; F_1 is the distance from the source; R is the bending radius; and χ, called

asymmetry angle, is the angle between the Bragg's plane and the normal to the input surface of the crystal.

In common conditions, the two foci do not coincide. Actually, three cases can be considered $f_p < f_g$; $f_p = f_g$ and $f_p > f_g$ (see Figure 5.6). Referring to Figure 5.6, it is clear how, for the specific task of spectral imaging application that require a polychromatic beam perfectly focused at the sample, the condition $f_p \approx f_g$ is the ideal condition to be realized [59, 56].

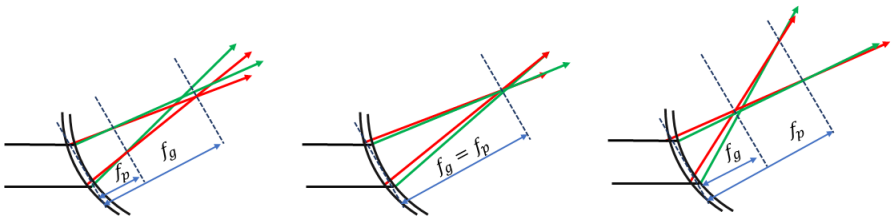

(a)

Figure 5.6: Possible focusing properties: (from left to right) $f_p < f_g$; $f_p = f_g$ and $f_p > f_g$. [59]

Thanks to its particular importance, the condition $f_p \approx f_g$ is better known as 'magic condition'. Usually the magic condition can be solved numerically. The solution is independent from the bending radius and allows determining the optimal asymmetry angle (characteristic of the cut of a crystal) to prepare a focused polychromatic beam once selected the optimal reflection plane (h, k, l) and the energy of interest selected by θ_B (as determined by eq. 5.2). For the simple case of high energies ($\theta_B << 1$) and $F_1 >> R$ it is possible to find the following analytical solution for the magic condition [56]:

$$\chi \approx \frac{\theta_B}{2+\nu} \tag{5.5}$$

Eq. 5.5 means that the magic condition is met for small asymmetry angles.

The focusing properties of bent Laue crystals have been thoroughly investigated by Qi et al. [148]. In the cited work, assuming a point source, the authors derived the following mathematical expression for the focal size:

$$S_f = \frac{f_p - f_g}{f_p} \cdot \frac{sin(2\theta_B)}{cos(\chi + \theta_B)} \cdot \frac{2R}{\nu} \cdot \sinh\left(\frac{\nu T_0}{2R}\right) \tag{5.6}$$

where T_0 is the thickness of the flat-crystal.

Another important feature of the bent-Laue crystal configuration is the ability to set the energy dispersion (i.e. the energy bandwidth) described by the following expression:

$$\frac{\Delta E}{E} = cot(\theta_B) \cdot h\left(\frac{1}{F_1} + \frac{1}{R\cos(\chi + \theta_B)}\right) \tag{5.7}$$

where h is the height of the beam incident to the crystal surface. When the magic condition is met, the entire energy bandwidth is focused at the sample. As described by eq. 5.7, once selected the reference energy (i.e. θ_B) the functional dependence of the energy bandwidth achievable with a bent crystal can be tuned by properly setting the beam height, the bending radius and the asymmetry angle. Of note, for flat crystals (i.e. $R \to \infty$) eq. 5.7 can be rewritten as follows:

$$\frac{\Delta E}{E} = \Delta\theta \cdot cot(\theta_B) \tag{5.8}$$

where $\Delta\theta = h/F_1$ is the angular divergence of the beam incident to the crystal.

5.2 PREPARATION OF A SETUP FOR K-EDGE IMAGING WITH BENT-LAUE CRYSTALS

In this section the first preliminary results achieved within the KISS collaboration are presented. The acquisition setup, implemented at the SYRMEP beamline of Elettra synchrotron (Trieste), was optimized for spectral imaging around 20 keV.

5.2.1 *Acquisition setup*

Practical implementation of bent-Laue crystals

The practical implementation of the bent-Laue geometry involves the use of an external device (called bender or bending frame) to curve the crystal with a specified bending radius. The bender developed at the INFN of Trieste consists of two metallic frames with an opening to allow the passage of X-rays. The designed bender works as follows: the first frame is curved by a specified radius, after placing the crystal on the first frame, the second frame is applied on top of the crystal. This latter frame includes two horizontal bars at the extremities that apply a mechanical pressure to the ends of the crystal, thus making it adhere to the curved surface of the first frame.

In the framework of the KISS collaboration, bending frames with different bending radii are in preparation. The one used for the preliminary setup with a radius of $R = 0.5\ m$ is shown in Figure 5.7.

The crystal employed in the setup was a 762 μm thick $Si(1,1,2)$ wafer with a Poisson's ratio of $\nu = 0.182$. The crystal was cut with an asymmetry angle $\chi = 3°$ to approximately meet the magic condition in around 20 keV (Bragg's angle $\theta_B = 5.673°$), when selecting the reflection $(1,1,-1)$.

At the SYRMEP beamline, the source is a bending magnet. Considering a distance source-crystal of $d_{SC} \approx 22\ m$ and the characteristics of the bent-crystal, the polychromatic and monochromatic foci were respectively $f_p = 24.7\ cm$ and $f_g = 23.2\ cm$ (eq. 5.4 and 5.3). Under

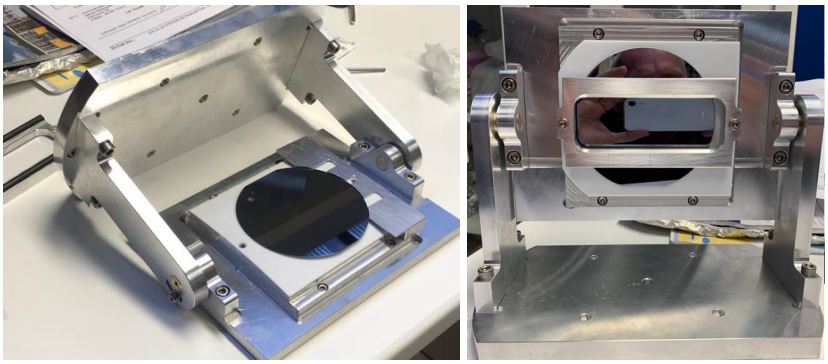

(a) (b)

Figure 5.7: Bender with bending radius $R = 0.5\ m$ employed in the experimental setup for KES imaging with a bent-Laue Si crystal.

these conditions, the magic condition $f_p \approx f_g$ is approximately met by achieving a suitable focus size of $S_f \approx 10\ \mu m$ (eq. 5.6).

Acquisition geometry and sample description

A schematic of the acquisition setup is shown in Figure 5.8.

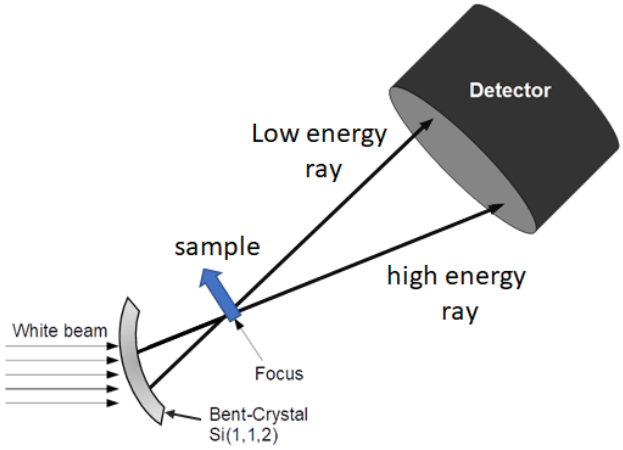

Figure 5.8: Sketch of the acquisition setup for KES imaging with a bent-Laue crystal.

The detector was a CCD imager with GadOx scintillator and a nominal pixel side of 33 μm, displaced 75 cm far from the focus and along the line determined by the Bragg's angle. The sample was placed in between the two foci, approximately 24 cm distant from the crystal, along the direction identified by the selected Bragg's reflection.

A sketch of the samples employed is shown in Figure 5.9. In order to test the suitability of the acquisition system for K-edge imaging, the sample was essentially made by two 50 μm thick foils of Mo (K-edge energy $\approx 20\ keV$) and Nb (K-edge energy $\approx 19\ keV$) placed as shown in Figure 5.9. To test a more complex sample geometry with more

than two materials, first a bee and then a bone were placed in close proximity to the Mo foil.

The bone was imaged to evaluate also the effects of the so-called crossover artifact which, as described in sect. 2.3.3, typically occurs when imaging thick absorbers with high attenuation coefficients. This artifact, generated by the slightly different paths that the focused beam takes through the sample, introduces in KES (or BMD) images artificial shadows with dark/bright derivative profiles along the scan's direction.

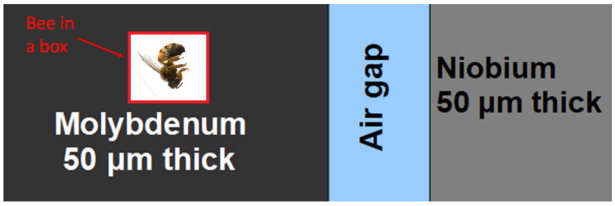

(a)

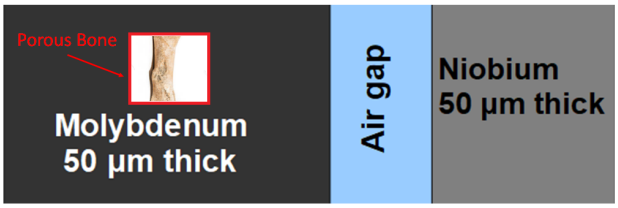

(b)

Figure 5.9: Description of the samples. During the acquisition the samples are on the focus so that the beam enters the sample focusing in an ideal row and then exits towards the detector position (see also Figure 5.8).

5.2.2 *First images*

The sample was placed at the focus and scanned along the direction normal to the line focus-detector. In this setup, each image acquires the same row of the sample at different energies displaced along the vertical direction of the detector. By scanning the sample at the focus, the data collected result in a stack of images where the horizontal direction refers to the sample width, the vertical direction refers to the energies and the third direction refers to the sample height (Figure 5.10).

In the acquired images the suitable beam covered an area of 1278×512 pixel ($38.3 \times 15.4\ mm^2$). Moreover, an energy dispersion of $\Delta E \approx 1.9\ keV$ was measured.

The images of the whole scan of the sample at the focus were reshaped to achieve a set of 2D images of the sample at different energies (Figure 5.11).

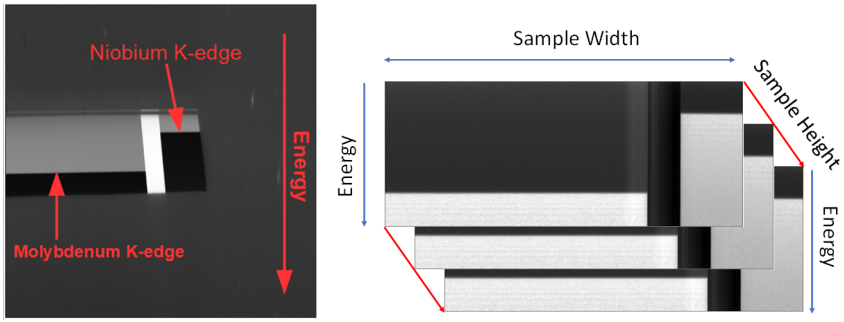

(a) (b)

Figure 5.10: (a) Single image acquired with the bent-Laue setup: each horizontal row is the image of an ideal row of the sample at different energies displaced along the vertical axis. (b) Images collected in a complete scan of the sample, the horizontal and the vertical axes are as described in (a), the third axis (red arrow) refers to the vertical size of the sample.

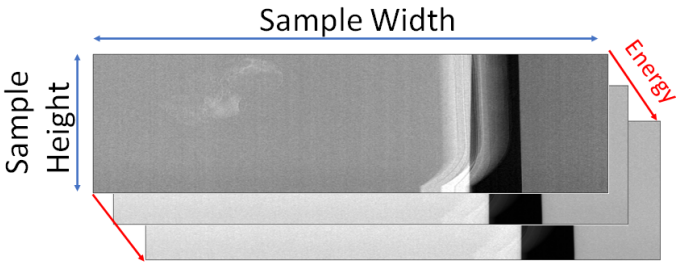

Figure 5.11: Set of 2D images at different energies obtained by reshaping the original dataset.

Since the scan at the focus requires the acquisition of the sample at different vertical positions, the vertical pixel side is a function of the speed and the exposure time; i.e. $p_y = v \cdot t$. With the presented setup, the samples were scanned in continuous motion with a constant speed of $v = 0.05\ mm/s$ and with an exposure time $t = 1.2\ s$, resulting in a vertical pixel side $p_y = 60\ \mu m$. The horizontal pixel side, instead, was equal to the nominal pixel side $p_x = 33\ \mu m$.

Finally, the images were processed with the BMD algorithm with three bases: Mo, Nb and C (for the bee) or Bone cortical (for the bone). If compared to other imaging setups for spectral imaging, this setup allows the sampling of multiple energies, thus potentially enabling the use of more than two bases. Figure 5.12 shows the plots of the signals measured on two ROIs respectively in correspondence with the foils *Mo* and *Nb*; the fits of $(\mu/\rho) \cdot \rho\xi$ in output from the BMD algorithm are also shown. Referring to the figure, it can be also argued

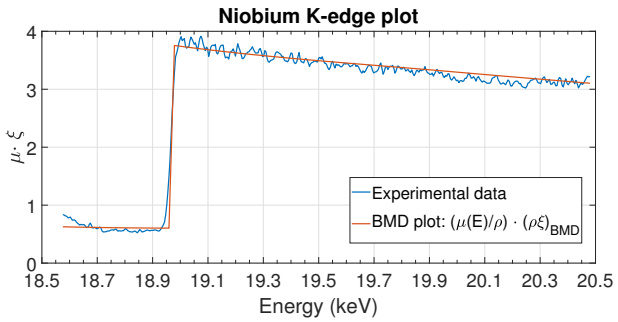

(a)

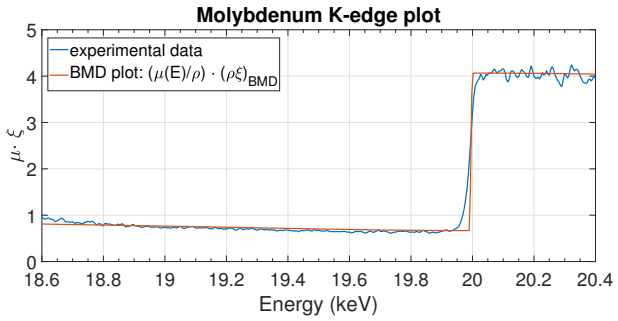

(b)

Figure 5.12: Plots of the signals measured on two ROIs respectively in correspondence with the foils *Nb* (a) and *Mo* (b); the fits of $(\mu/\rho) \cdot \rho\xi$ in output from the BMD algorithm are also shown.

that the bent-crystal system allows a more robust application of the BMD decomposition if compared to dual energy systems. In particular, due to the extended energy range sampled with quasi-monochromatic energies, more than two energy contents can be exploited in the BMD algorithm.

In Figure 5.13 are reported the resulting images for the bee.

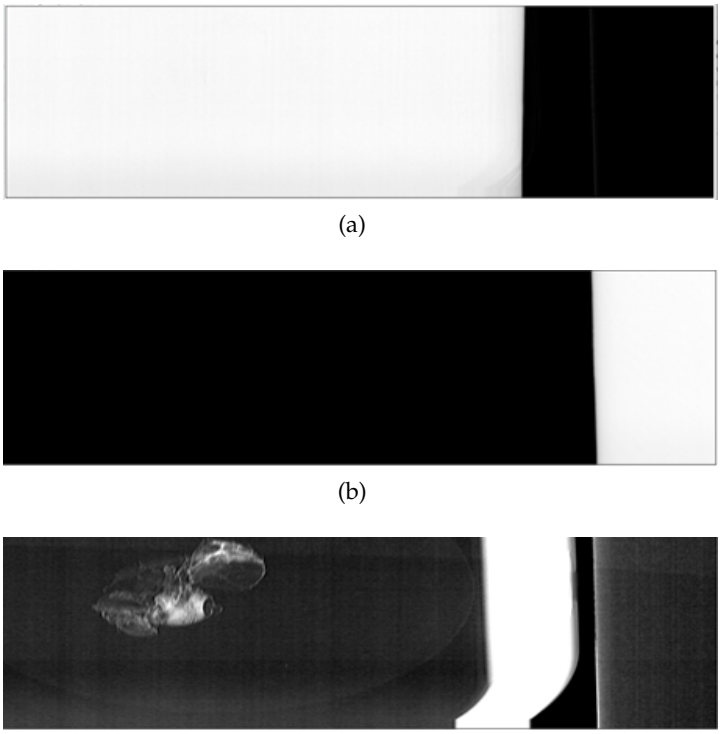

(a)

(b)

(c)

Figure 5.13: BMD of the bee sample: (a) Mo; (b) Nb; (c) C.

Referring to Figure 5.13, the BMD algorithm correctly separates the bee and the two foils of Mo and Nb respectively in the carbon, molybdenum and niobium bases.

In Figure 5.14 the basis material decomposition for the bone is shown.

For this case, the three elements composing the sample (bone, niobium and molybdenum) are well separated. However, the cross-over artifact is present in both the Mo and Nb images in correspondence of the the thickest features of the bone. Therefore, this issue has to be taken into account when imaging with bent-Laue crystals. Algorithmic solutions to reduce the cross-over artifacts have been proposed in [55]. Ideally, the crossover artifact can be totally removed by scanning the sample out from the focus. This option has been recently considered by the Author; a dedicated reconstruction algorithm to retrieve spectral information from images collected out from the focus is the subject of an original work in preparation.

5.3 CONCLUSIONS

A prototype setup for spectral imaging with bent-Laue crystal has been implemented at the SYRMEP beamline. Results showed that by reproducing the the magic condition it is possible imaging multiple K-edge elements with an adequate spectral separation between mul-

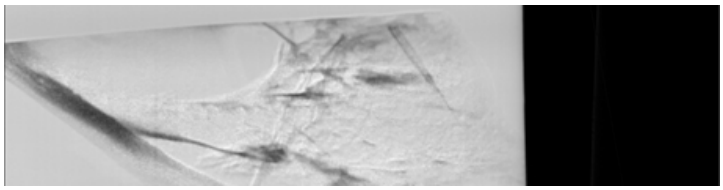

(a)

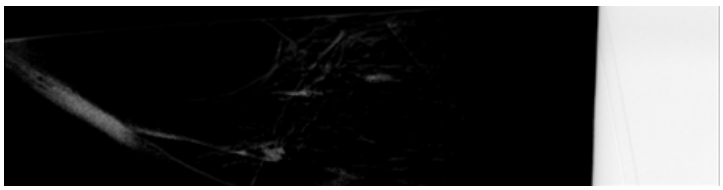

(b)

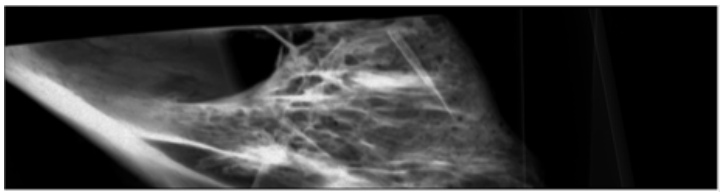

(c)

Figure 5.14: BMD of the bone sample: (a) Mo; (b) Nb; (c) Bone cortical. The crossover artifact can be observed in both Mo (a) and Nb (b) images as dark/bright shadows in correspondence of the most absorbing features of the bone.

tiple materials. Moreover, the portability of the bent-Laue system (crystal+bender) allows the implementation of the setup at different synchrotron sources.

At this early stage, a suitable setup for spectral imaging was set at low energies, i.e. around 20 keV with a measured energy dispersion of $\Delta E = 1.9\ keV$. The main challenges of the KISS collaboration are represented by the optimization of different crystals and bending radii to allow KES imaging of the contrast agents of interest. Other studies are currently underway to select and buy properly cut crystals for preparing multiple setups optimized for KES imaging of the most common contrast agents (e.g. I, Ba, Gd) as well as non-conventional contrast media such as, e.g. Ag and Au nanoparticles with potential clinical applications.

6 CONCLUSIONS

The increasing interest on X-ray spectral imaging among the physician community is mainly due to the recent development and widespread of dedicated acquisition systems. In order to allow a proper application of spectral algorithms, a system dedicated to spectral imaging must achieve the main goal of acquiring X-ray projections at different energies in the same time. An ideal system for spectral imaging should be able to: (i) acquire perfectly co-registered projections with different energy contents in a single shot (ii) allow a proper setting of the energies collectible according to the specific task. Though the acquisition systems commercially available (sect 2.3) present adequate solutions for medical applications, none of them meet the ideal conditions above mentioned.

The work presented in this thesis concerned the realization and optimization of two state-of-the-art acquisition setups for spectral imaging in the framework of the two INFN collaborations; KEST and KISS. The main goal of these two spectral imaging setups was that of allowing the acquisition of multi-energy projections in a single-shot with the additional possibility to tune the energy contents of such images.

The first setup was mainly developed within the KEST collaboration. The project aimed at the implementation of an imaging system for KES-CT by coupling a polychromatic X-ray source with an energy resolving CdTe XPCD implementing two energy thresholds and an acquisition mode (NPISUM) specifically designed to cope with the charge-sharing issue with beneficial effects on the energy resolution. The implementation of this setup required first a refined characterization of the XPCD to evaluate its suitability for spectral applications and to get a complete picture of the achievable imaging performance (chapter 3). Then, a lab. setup for spectral micro-CT was actually implemented and optimized.

The first step in the optimization of the acquisition system was the development of a specifically designed image processing procedure able to achieve high quality (artifact-free) CT images (sect 4.2). Considering this procedure, the actual advantages of the NPISUM mode over the basic counting mode were assessed by directly comparing the CT images achieved with the two modes. The outcomes of this analysis showed that, for KES-CT applications, the charge-sharing correction implemented by the NPISUM mode leads to a considerable improvement in the image quality by preserving the detection efficiency of the XPCD (sect 4.3).

With the aim of allowing an easy planning of future experimental activities and further optimization studies, a simulator for X-ray imaging with energy resolving XPCDs has been conceived, developed and finally validated with actual images acquired with the experimental setup (sect 4.4). The result was a simulation tool able to faithfully reproduce the imaging performance of the implemented acquisition system. More generally, by allowing to simulate the performance of XPCDs with different characteristics (even ideal), the developed simulator can be a valuable tool to compare different setups and to explore the limits that can be reached with existing and future XPCD technology.

Finally, an automated routine for 3D mapping of a specific element has been developed to achieve the ultimate goal of a setup for KES-CT, i.e. the localization of the distribution of a contrast agent within a sample. This routine involved the use of a state-of-the art algorithm for discrete reconstruction (TVR-DART) that, combined to the specifically designed image processing procedure, demonstrated good KES-CT imaging performance even considering low doses (sect 4.5).

The final outcome of the KEST project was a lab-setup for KES-CT imaging developed and optimized to be suitable for *in vivo* applications. The main limitations to this setup are related to the technological limits of the employed XPCD. As an example, by implementing only two energy thresholds the XPCD employed in this setup was mainly limited to dual energy applications, e.g. KES imaging or decomposition in two materials by exploiting the BMD algorithm. The use of XPCDs implementing more than two energy thresholds would extend the range of spectral applications by allowing e.g. multi-material decomposition or multi K-edge imaging with a single acquisition. Moreover, even if it is clear that the small area featured by the employed XPCD limited the suitability of the implemented system to the imaging of small animals, upcoming generations of XPCDs with increased detection areas will make possible the actual implementation of acquisition systems for spectral imaging suitable for the clinical practice.

The second setup presented in this thesis work was developed within the KISS collaboration at the SYRMEP beamline of Elettra synchrotron (Trieste). The ongoing project aims at developing a customizable setup for KES imaging at synchrotron sources by providing a set of bent-Laue crystals, each of them suitable for one or more target K-edge materials including also non conventional contrast agents such as gold and silver nanoparticles. At its early stage, the project produced a crystal setup suitable for energies around 20 keV (chapter 5). The first images achieved with this setup, here reported and discussed, showed that a proper design of asymmetrically cut Si crystal allows extending spectral imaging at more than two materials with a single acquisition. This feature is of particular interest in further develop-

ment of multi-purpose spectral techniques with potential applications in medical research but also in material science.

In conclusion, whether looking at clinical practice or at pure research, it is the Author's opinion that by extending the degree of knowledge achievable with a single acquisition, spectral imaging will become an increasingly widespread technique. The development of increasingly accurate acquisition systems will be the key to extending the technique to new research fields, also allowing the development of new diagnostic tools.

A

LINEAR RADON APPROXIMATION

In monocrhomatic case an X-ray projection is directly linked with the linear attenuation coefficient of the sample as described by eq. 1.9. For a polychromatic spectrum $w(E)$, the physical interpretation of the X-ray projection, defined by eq. 1.12, is hampered by the energy dependence of the linear attenuation coefficient $\mu(E)$. In this case, a mathematical relationship between a planar projection and the attenuation coefficients $\mu(E,\bar{r})$ can be defined considering the approximations hereafter explained.

In the case of of small-absorbing object, the argument of the exponential function in eq. 1.12 can be approximated as follows:

$$\int_{\bar{\xi}} \mu(E,\bar{r})\, d\bar{r} \approx 0 \tag{A.1}$$

This approximation, called linear Radon approximation, is reasonable for small objects made of low Z absorbers, such as e.g. small water objects. By considering the Taylor expansion for $\exp(x) \approx 1 - x + \frac{1}{2} \cdot x^2 + o(x^2)$, in the linear Radon approximation eq. 1.12 can be rewritten as follows:

$$P(x,y) \approx -log\left(1 - \int_E \int_{\bar{\xi}} w(E)\, \mu(E,\bar{r})\, d\bar{r}\, dE + \right. \\ \left. + \frac{1}{2} \int_E w(E) \left(\int_{\bar{\xi}} \mu(E,\bar{r})\, d\bar{r} \right)^2 d\bar{r}\, dE - ... \right) \tag{A.2}$$

In the same approximation, the logarithm in eq. A.2 can be Taylor expanded as a function $log(1-x) \approx x,\ for\ x \to 0$:

$$P(x,y) \approx \int_E \int_{\bar{\xi}} w(E)\, \mu(E,\bar{r})\, d\bar{r}\, dE - \frac{1}{2} \int_E w(E) \left(\int_{\bar{\xi}} \mu(E,\bar{r})\, d\bar{r} \right)^2 dE \tag{A.3}$$

In eq. A.3, the quadratic term is a second order infinitesimal, therefore in the first order approximation:

$$P(x,y) \approx \int_{\bar{\xi}} \int_E w(E)\, \mu(E,\bar{r})\, d\bar{r}\, dE \tag{A.4}$$

Finally, eq. A.4 can be rewritten as follows:

$$P(x,y) \approx \int_{\bar{\xi}} \bar{\mu}(\bar{r})\, d\bar{r} \tag{A.5}$$

where:

$$\bar{\mu}(\bar{r}) = \int_E w(E)\, \mu(E,\bar{r})\, dE \tag{A.6}$$

is called spectral weighted attenuation coefficient.

Eq. A.5 is formally identical to eq. 1.9. This means also that, the linear Radon approximation allows handling the equations of X-ray projections with a polychromatic spectrum in analogy with the monochromatic case. In the polychromatic case, eq. A.5 is of fundamental importance especially for all the model-based reconstruction algorithms, such as the BMD technique.

B

KES-CT SIGNAL AS A FUNCTION OF THE CONCENTRATION OF A K-EDGE ELEMENT

This section presents the derivation of an analytical formula that make explicit the relationship between the KES-CT image and the concentration α of the K-edge element in the sample. In this derivation, the contrast agent is modeled as a mixture of water and a K-edge element such as Iodine, Barium or Gadolinium.

B.0.1 *Polychromatic case*

In polychromatic CT, each voxel reconstructs the weighted attenuation $\bar{\mu}$. This signal can be derived by coupling eq. 2.2 with eq. 2.3:

$$\bar{\mu} = \left[\alpha \cdot \frac{\bar{\mu}_k}{\rho_k} + (1-\alpha)\frac{\bar{\mu}_s}{\rho_s}\right] \cdot \rho \tag{B.1}$$

To simplify the calculations, the density in eq. 2.3 is here rewritten in the following way:

$$\rho = \frac{\rho_s}{1-\alpha\cdot(1-r)};\ with\ r = \frac{\rho_s}{\rho_k} \tag{B.2}$$

For high Z K-edge elements diluted in water $r < 1$. Moreover, in the clinical practice the concentrations of the diluted K-edge elements are around 100 ml/mg that correspond to a relative weight in water $\alpha \approx 10^{-1}$ or lower. Under these conditions, the approximation $\alpha \cdot (1-r) \approx 0$ is reasonable, thus eq. (B.2) can be Taylor expanded as follows:

$$\rho \approx \rho_s \cdot [1 + \alpha \cdot (1-r)] \tag{B.3}$$

By substituting (B.3) in (B.1), omitting some easy mathematical calculations the following expression for the reconstructed $\bar{\mu}$ can be derived:

$$\bar{\mu} = \bar{\mu}_s + \alpha r \cdot (\bar{\mu}_k - \bar{\mu}_s) + \alpha^2(1-r)(\bar{\mu}_k \cdot r - \bar{\mu}_s) \tag{B.4}$$

The KES signal is obtained by subtracting the 'low' image to the 'high' image:

$$KES_{CT} = \bar{\mu}_{high} - \bar{\mu}_{low} = \Delta\bar{\mu} \tag{B.5}$$

From eq. (B.4) follows the mathematical formula for KES imaging with polychromatic sources:

$$KES_{CT} = \Delta\bar{\mu}_s + \alpha r \cdot (\Delta\bar{\mu}_k - \Delta\bar{\mu}_s) + \alpha^2(1-r)(\Delta\bar{\mu}_k \cdot r - \Delta\bar{\mu}_s) \tag{B.6}$$

Eq. B.6 describes the behavior of the KES signal as a function of the relative weight of the K-edge element in the contrast agent. It is worth

to underline that, for a determined K-edge element, in eq. B.6 r is a constant and the attenuation coefficients refer to the pure elements in the solution, e.g. iodine in water.

B.0.2 *KES signal in monochromatic case*

KES imaging can be ideally performed with two consecutive scans using two monochromatic energies infinitesimally below and above the target K-edge. In this case, the spectral weighted $\bar{\mu}$ is a monochromatic μ. Moreover, for two close energies $\Delta\mu_s \approx 0$ and $\Delta\mu_k$ is the K-edge jump of the attenuation coefficient. In the same approximation of $\alpha << 1$, for the monochromatic case eq. B.6 can be rewritten as follows:

$$KES_{CT} = \alpha \cdot r(\Delta\mu_k) + \alpha^2 \cdot (1 - r)r\Delta\mu_k \tag{B.7}$$

where $\Delta\mu_k$ is the jump in the linear attenuation coefficient of the pure K-edge element.

Some examples: KES signal as function of the concentration

Figure B.1 shows the plot of KES signals as a function of the relative weights of Iodine, Barium, Gadolinium K-edge elements in water. Figure B.1 shows how the KES signal increases with the increase of the

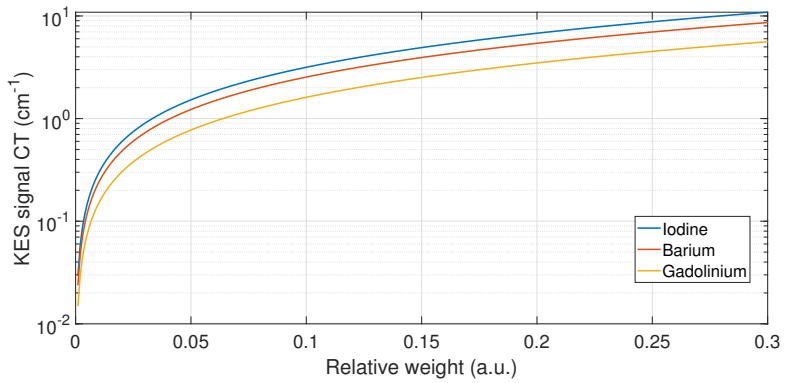

Figure B.1: Plots of KES signal with two monochromatic energies infinitesimally below and above the target K-edge

relative weight of the K-edge element. Moreover, at fixed KES signal it is worth to underline that the required relative weight increases with the Z the K-edge element.
The plots shown in Figure B.1 report the highest KES signal achievable, thus giving a theoretical limit to the visibility of a target K-edge element. In absence of noise, very low quantities of the K-edge element can be detected.

For the sake of completeness, the relative weights can be converted into milligrams of K-edge element per milliliter (i.e. mg/ml). This unit is more frequently used. Figure B.2 reports the plot of KES signals as a

function of the concentrations of iodine, barium, gadolinium K-edge elements in water

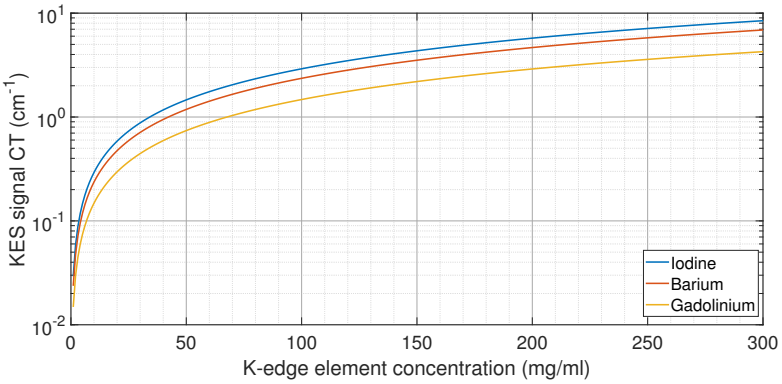

Figure B.2: Plots of KES signal with two monochromatic energies infinitesimally below and above the target K-edge

C

SIMPLIFIED MONTE CARLO MODEL TO SIMULATE THE SPECTROSCOPIC PERFORMANCE OF THE PIXIRAD/PIXIE-III XPCD

The spectroscopic performance of a XPCD are potentially affected both by the charge-sharing issue and by secondary fluorescence photons induced within the semiconductor sensor. If the charge summing algorithm fully corrects for the charge sharing issue, it can only partially solve the problem of fluorescences. Considering the charge summing algorithm, the problem of fluorescence photons can be summarized as follows: (i) if the fluorescence photon releases its energy within the cluster of pixels considered by the charge summing algorithm, the incoming photon with energy E is correctly detected; (ii) if a fluorescence photon with energy E_f releases its energy outside the cluster defined by the charge summing algorithm, an input photon with energy E generates two separate signals. These signals are interpreted by the XPCD readout as two separate photons with energy respectively E_f and $E - E_f$. For spectral applications this latter case can induce an incorrect allocation of photons within the energy bins selected by the energy thresholds of the XPCD. Therefore, to properly simulate the response of a real XPCD, this effect has to be considered.

This section presents the modeling and the development of a MC simulator to estimate the spectroscopic response of the Pixirad-1/pixie-iii XPCD. The model considers photons with energies in the range 10 keV-60 keV and a XPCD featuring the same characteristics of the Pixirad-1/pixie-iii, i.e. 650μm thick CdTe sensor and a pixel pitch of 62 μm. Considering the scheme of the charge summing algorithm implemented in the pixie-iii readout system, the MC model simulates the spectroscopic performance of the simulated detector. These information can be then exploited to calculate the energy responsivity ϵ achieved by the simulated XPCD.

C.1 MODEL

Usually a MC model for a semiconductor XPCD includes [151]: (i) the interaction of incoming photons with the semiconductor sensor; (ii) the production of secondary photons, scattered or fluorescence photons; (iii) the production of couples charges-holes; (iv) the charge collection at the pixels.

The model here described presents several simplifications. In particular, the points (iii) and (iv) are replaced by geometrical considerations as described in the following sections. Moreover, considering that

in the range of energies considered the photoelectric absorption is the dominant interaction in CdTe, Compton scattering has not been considered.

C.1.1 *Interactions radiation-CdTe-sensor*

Absorption of incoming radiation

The geometry of the CdTe sensor is described in Figure C.1. The position (x_0, y_0) of the incoming radiation within the pixel area is randomly assigned.

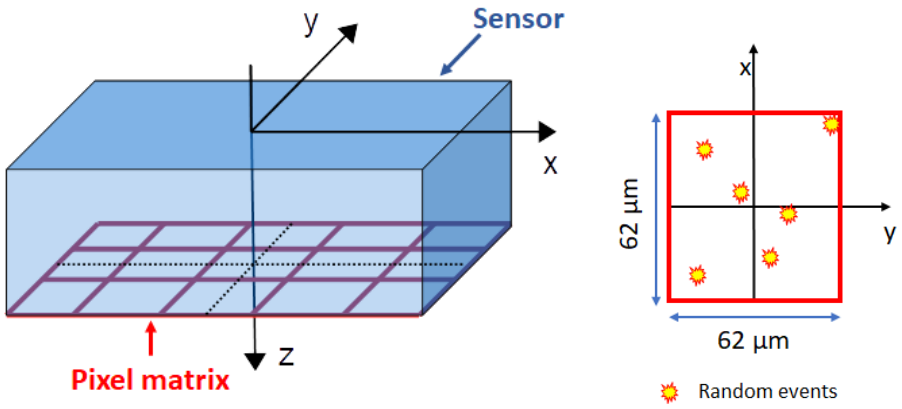

(a) (b)

Figure C.1: Geometry of the simulated XPCD: (a) Cartesian coordinate system for the sensor and the pixel matrix; (b) the positions (x_0, y_0) of the input event is randomly generated within the pixel centered in $(x_c, y_c) = (0, 0)$.

The attenuation depth, z_0, of the incoming photon is calculated from the probability distribution obtained from the Lambert-Beer's law:

$$P(z) = e^{-\mu_{CdTe}(E)\cdot z} \tag{C.1}$$

The probability of interacting with a Cd or Te atom has been calculated as follows [152]:

$$P_{Cd} = w_{Cd}\frac{(\mu/\rho)_{Cd}}{(\mu/\rho)_{CdTe}}; \quad P_{Te} = w_{Te}\frac{(\mu/\rho)_{Te}}{(\mu/\rho)_{CdTe}}; \tag{C.2}$$

where ρ is the density of the material; $w_{Cd} = 0.4684$ and $w_{Te} = 0.5316$ are respectively the weight fractions of Cd and Te in CdTe [9].

Secondary photons: fluorescences

The first stage of the simulation process outputs the attenuation depth within the CdTe sensor and the atom with which the incoming radiation interacts.

If the energy of the incoming radiation interacting with a Cd or Te atom is below their K-edge energy ($E_{K(Cd)} = 26.7\ keV$; $E_{K(Te)} = 31.8\ keV$), the photon releases all its energy in the first interaction. The spatial coordinates of this interaction are defined as follows:

$$R_0 = (x_0, y_0, z_0) \tag{C.3}$$

where (x_0, y_0) is the random position of the incoming radiation in the plane of the pixel matrix and z_0 is the attenuation depth in the CdTe sensor.

If the energy of the incoming radiation interacting with a Cd or Te atom is above their K-edge energy, a secondary fuorescence photon can be emitted by a Cd or Te atom. Such photon can release its energy far from the pixel where the primary interaction occurs. The probability of inducing a fluorescence photon is defined by the Jump factor (J_k) [153, 151]:

$$J_k = \frac{r_k - 1}{r_k} \tag{C.4}$$

where r_k, called jump ratio, is the ratio between the K- shell photoionization cross section and the photoionization cross section of the rest of the atom at the K-edge.

After an electron is kicked out from the K-shell of an atom, different transitions can be induced. The energies and and the rate of the transitions generated as consequence of the K-shell ionization are summarized in Table C.1. The photons generated by the transitions

	transition	Energy (keV)	rate
Cd	$k\alpha 1$	23.174	0.55
	$k\alpha 2$	22.984	0.29
	$k\beta 1$	26.095	0.09
	$k\beta 2$	26.654	0.02
	$k\beta 3$	26.061	0.05
Te	$k\alpha 1$	27.473	0.53
	$k\alpha 2$	27.202	0.29
	$k\beta 1$	30.996	0.10
	$k\beta 2$	31.700	0.03
	$k\beta 3$	30.945	0.05

Table C.1: Energy and rates of Cd and Te k-transitions [154].

listed in Table C.1 are called fluorescence photons. The direction of the emitted fluorescence photon is uniformly distributed over all solid angles. The length d of the path of such photons is determined as described by eq. C.1. The fluorescence photon can be then absorbed,

induce another fluorescence or escape the sensor. The spatial coordinates of the primary interaction, $R_0 = (x_0, y_0, z_0)$, and the point $R_f = (x_f, y_f, z_f)$ where the fluorescence photon deposits its energy are computed by the simulation as shown in Figure C.2.

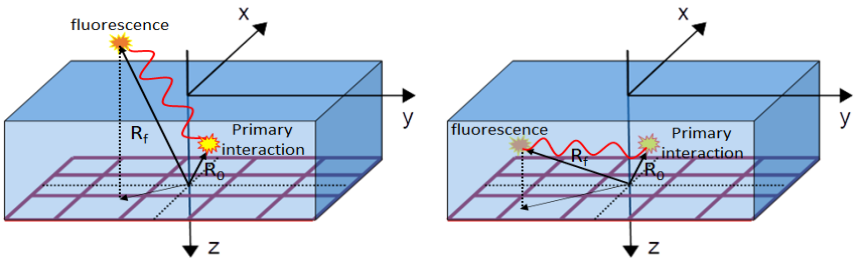

Figure C.2: Example of $R_0 = (x_0, y_0, z_0)$ and $R_f = (x_f, y_f, z_f)$ computation. In (a) the fluorescence photon escapes the sensor; in (b) the fluorescence photon releases its energy within the sensor.

C.1.2 *Spectral response reconstruction*

The considerations made to perform the spectral response reconstruction of the simulated XPCD are hereafter described. At this stage, usually a MC model simulates the production of electrons/holes within the sensor, the drift of the charge cloud and the charge collection at each pixel.

The model here presented implements some simplifications. The first is that, independently from the energy released by the considered interaction, the size of the charge cloud at the pixel collection is considered to be a homogeneous distribution of charges displaced in a circular area with diameter $\approx p_x/2$, where p_x is the pixel pitch.

The pixel where the primary interaction occurs is divided into 3 types of sub-regions (central, edge, corner) showed in Figure C.3.

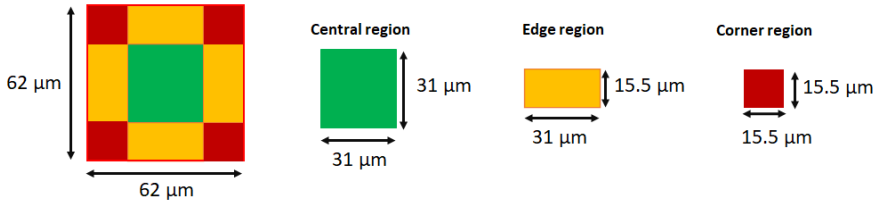

Figure C.3: The pixel where the primary interaction occurs is divided into sub-regions.

According to the region where the primary interaction occurs, the charge summing algorithm has been simulated as follows:

- if the primary interaction occurs in the central region, all the neighboring pixels can be considered in the cluster defined by

the charge summing algorithm. In this case four possible clusters can be considered (Figure C.4 (a)).

- if the primary interaction occurs in an edge region, the event is considered to be shared among two neighboring pixels. In this case, only two clusters including the pixels were the event is shared can be considered (Figure C.4 (b)).
- If the primary interaction occurs in a corner region, the event is considered already shared in a cluster of four neighboring pixels (Figure C.4 (c)).

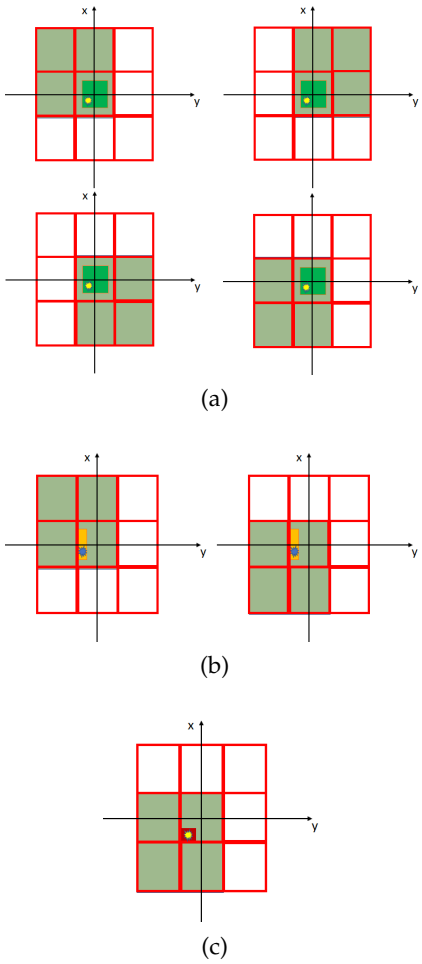

Figure C.4: Charge summing algorithm simulation: (a) if the if the primary interaction occurs in the central region, the algorithm considers four possible clusters; (b) if the primary interaction occurs in an edge region only two possible clusters are considered; (c) If the primary interaction occurs in a corner region, only one cluster of pixels is considered.

In the model two cases are distinguished: (i) the primary interaction does not induce fluorescences; (ii) secondary fluorescence photons are induced.

In the first case, the charge cloud delivered by the primary interaction is considered totally recovered by the charge summing algorithm. Therefore, the energy of the incoming radiation is correctly evaluated.

The second case presents the complications arising from secondary fluorescence photons emitted by Cd or Te. In this case, the position $R_f = (x_f, y_f, z_f)$ where the fluorescence photon interacts plays a crucial role.

The height z_f of the fluorescence photon determines if the fluorescence photon interacts within the sensor or if it escapes the sensor. In this latter case, an incoming photon with energy E is erroneously detected as a photon with energy $E - E_f$.

If the fluorescence photon does not escape the sensor, its position (x_f, y_f) in the pixel matrix is evaluated. In particular, if the fluorescence photon interacts outside from one of the possible clusters defined above, the primary interaction and the fluorescence photon are detected as two separate events with energy respectively $E - E_f$ and E_f. If the fluorescence photon releases its energy within a possible cluster, the identified cluster is uniquely defined and divided into sub-regions as shown in Figure C.5.

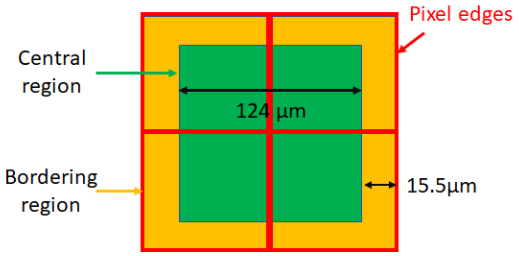

Figure C.5: The possible cluster identified by the charge summing algorithm is divided into sub-regions.

Referring to Figure C.5, the energy released by the fluorescence photon is assigned as follows:

- if the fluorescence photon interacts in the central region, the energies of the primary interaction and the secondary photon are summed-up. In this case, the energy of the incoming radiation is properly evaluated.
- if the fluorescence photon interacts in the bordering regions, the center of mass of the induced charge cloud falls outside from the cluster. Therefore, the fluorescence event is handled as an independent event triggering its own cluster. In this case, two separate photons are detected: the primary interaction with energy $E - E_f$ and the fluorescence photon with energy E_f.

C.2 RESULTS

Given an input spectrum $W(E)$, the MC model here presented outputs the spectrum $W_{det}(E)$ as detected by the simulated XPCD.

In practice the spectra are acquired by performing threshold scans, therefore the spectroscopic performance of a XPCD depend also on the energy resolution of the implemented threshold. To validate the model here described, threshold scans of $W_{det}(E)$ were simulated by using the simulator described in sect. 4.4. The results were compared with actual spectra acquired with the Pixirad-1/pixie-iii XPCD.

In Figure C.6 are showed the spectra acquired for monochromatic photons with energies: (a) 26 keV; (b) 33 keV; (c) 37 keV; (d) 50 keV.

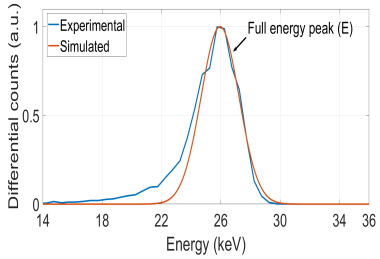

(a) $E = 26\ keV$.

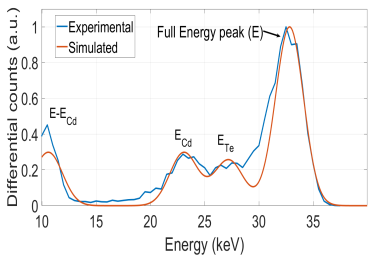

(b) $E = 33\ keV$.

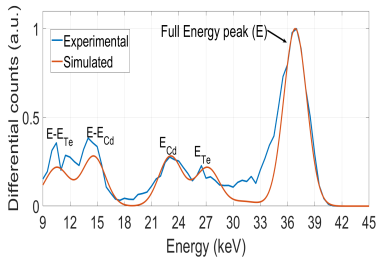

(c) $E = 37\ keV$.

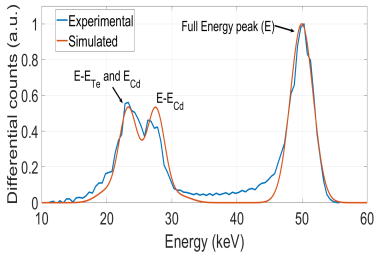

(d) $E = 50\ keV$.

Figure C.6: Experimentally observed and simulated spectra for monochromatic radiation set to: (a) $E = 26\ keV$; (b) $E = 33\ keV$; (c) $E = 37\ keV$; (d) $E = 50\ keV$.

For each simulation, 10^4 photons were employed. The results in Figure C.6 show a good agreement between the simulated and the actual spectra. Slight mismatches between the experimental spectra and the model are observed at low energies $< 20\ keV$ and in the left sides of the full energy peaks. In particular, the asymmetric left tail in the left side of the full energy peak is not properly reproduced by the simulator. The source of such deviations can be due to residual charge sharing effects occurring in the actual case and not considered by the simplified MC model.

The case of a polychromatic spectrum generated by an X-ray tube has been considered as well. In particular, for an X-ray tube with Voltage 40 kV, current 200μA, filter 0.253 $mmCu$, threshold scans

were both acquired and simulated. In the simulated case, the input spectrum was generated with Spektr 3.0 toolbox. Figure C.7 shows the comparison between the simulated and the actual spectroscopic response of the Pixirad-1/pixie-iii XPCD when considering a polychromatic spectrum.

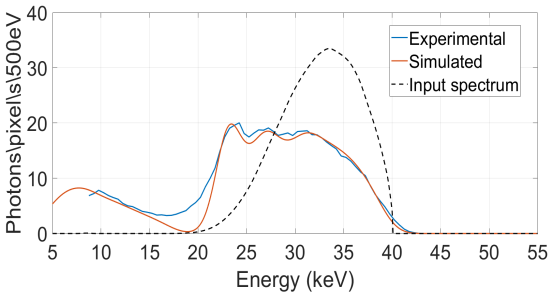

Figure C.7: Experimentally observed and simulated spectra for a polychromatic beam generated by an X-ray tube with the following settings: Voltage 40 kV, current 200μA, filter 0.253 $mmCu$.

As reference, in Figure C.7 the input spectrum was plotted. Referring to the figure, the simulated and the actual spectroscopic performance are in good agreement limited to energies above 20 keV. Also in this case, the visible mismatch between the simulated and the actual spectra occurring in the energy range $15 - 20$ keV can be attributed to the charge sharing effects not properly simulated by the MC model. However, tor the case of study presented in sect. 4.4 where only thresholds ≥ 26 keV were considered, the MC model here described is fully suitable.

For further studies and to extend the validity of the simulator described in sect 4.4, a more detailed MC simulator implementing the charge collection is in preparation.

BIBLIOGRAPHY

[1] W. C. Röntgen. "On a new kind of rays". In: *Science* 3.59 (1896), pp. 227–231. DOI: 10.1126/science.3.59.227 (cit. on p. 1).

[2] J. D. Howell. "Early clinical use of the X-ray". In: *Transactions of the American Clinical and Climatological Association* 127 (2016), pp. 341–349 (cit. on p. 1).

[3] *KEST experiment*. https://web.infn.it/kest. Accessed: 2020-01-31 (cit. on p. 2).

[4] G. F. Knoll. *Radiation detection and measurement*. 4th ed. Wiley New York, 2010. ISBN: 978-0-470-13148-0 (cit. on pp. 4, 33, 38, 85).

[5] J. Fernandez. *Interaction of X-rays with matter*. Jan. 2000, pp. 17–62. ISBN: 0-471-97426-9 (cit. on p. 4).

[6] T. Buzug. *Computed tomography: From photon statistics to modern cone-beam CT*. 2008, pp. 1–521. DOI: 10.1007/978-3-540-39408-2 (cit. on pp. 4, 9).

[7] A. Sethi. "X-Rays: Interaction with Matter". In: *Encyclopedia of Medical Devices and Instrumentation*. American Cancer Society, 2006. ISBN: 9780471732877. DOI: https://doi.org/10.1002/0471732877.emd263 (cit. on p. 4).

[8] E. F. Plechaty, Dermott Cullen, and R.J. Howerton. "Tables and graphs of photon-interaction cross sections from 0.1 keV to 100 MeV derived from the LLL Evaluated-Nuclear-Data Library". In: (Dec. 1978). DOI: 10.2172/6320120 (cit. on p. 4).

[9] M. J. Berger et al. "XCOM: photon cross sections database". In: *NIST Standard Reference Database* 8 (1998). DOI: https://dx.doi.org/10.18434/T48G6X (cit. on pp. 4, 136).

[10] J. M. Boone and A. E. Chavez. "Comparison of x-ray cross sections for diagnostic and therapeutic medical physics". In: *Medical Physics* 23 (12 1996). ISSN: 00942405. DOI: 10.1118/1.597899 (cit. on p. 4).

[11] *NIST XCOM database*. https://physics.nist.gov/PhysRefData/Xcom/html/xcom1.html. Accessed: 2020-01-31 (cit. on p. 4).

[12] *XMuDat: Photon attenuation data on PC*. https://www-nds.iaea.org/publications/iaea-nds/iaea-nds-0195.htm. Accessed: 2020-01-31 (cit. on p. 4).

[13] J. H. Hubbell. "Photon cross sections, attenuation coefficients, and energy absorption coefficients from 10 keV to 100 GeV". In: *National Standard Reference Data System.* (1969) (cit. on pp. 4, 14).

[14] B. Heismann, B. Schmidt, and T. Flohr. *Spectral computed tomography*. SPIE press, 2012. DOI: 10.1117/3.977546 (cit. on pp. 6, 7, 18, 19).

[15] A. C. Kak and M. Slaney. *Principles of Computerized Tomographic Imaging*. USA: Society for Industrial and Applied Mathematics, 1987. ISBN: 089871494X (cit. on p. 9).

[16] L. A. Feldkamp, L. C. Davis, and J. W. Kress. "Practical cone-beam algorithm". In: *J. Opt. Soc. Am. A* 1.6 (1984), pp. 612–619. DOI: 10.1364/JOSAA.1.000612 (cit. on p. 9).

[17] W. Thomlinson et al. "K-edge subtraction synchrotron X-ray imaging in bio-medical research". In: *Physica Medica* 49 (May 2018), pp. 58–76. DOI: 10.1016/j.ejmp.2018.04.389 (cit. on p. 11).

[18] B. Bertrand et al. "Comparison of synchrotron radiation angiography with conventional angiography for the diagnosis of in-stent restenosis after percutaneous transluminal coronary angioplasty". In: *European Heart Journal* 26.13 (Feb. 2005), pp. 1284–1291. DOI: 10.1093/eurheartj/ehi165 (cit. on p. 11).

[19] M. Van Straten et al. "Automated bone removal in CT angiography: Comparison of methods based on single energy and dual energy scans". In: *Medical Physics* 38 (11 2011). DOI: 10.1118/1.3651475 (cit. on p. 11).

[20] X. Kong et al. "Xenon-enhanced dual-energy CT lung ventilation imaging: Techniques and clinical applications". In: *American Journal of Roentgenology* 202 (2 2014). ISSN: 0361803X. DOI: 10.2214/AJR.13.11191 (cit. on p. 11).

[21] A. N. Primak et al. "Noninvasive Differentiation of Uric Acid versus Non-Uric Acid Kidney Stones Using Dual-Energy CT". In: *Academic Radiology* 14 (12 2007). ISSN: 10766332. DOI: 10.1016/j.acra.2007.09.016 (cit. on p. 11).

[22] R. E. Alvarez and A. Macovski. "Energy-selective reconstructions in X-ray computerised tomography". In: *Physics in Medicine and Biology* 21.5 (1976), pp. 733–744. DOI: 10.1088/0031-9155/21/5/002 (cit. on p. 14).

[23] T. F. Coleman and Y. Li. "A reflective Newton method for minimizing a quadratic function subject to bounds on some of the variables". In: *SIAM Journal on Optimization* 6 (4 1996). ISSN: 10526234. DOI: 10.1137/S1052623494240456 (cit. on p. 14).

[24] R. E. Ricketts. "Practical optimization". In: *International Journal for Numerical Methods in Engineering* 18 (6 1982). ISSN: 0029-5981. DOI: 10.1002/nme.1620180612 (cit. on p. 14).

[25] C. L. Lawson and R. J. Hanson. *Solving Least Squares Problems*. 1995. DOI: 10.1137/1.9781611971217 (cit. on p. 15).

[26] P. Baldelli et al. "Evaluation of the minimum iodine concentration for contrast-enhanced subtraction mammography". In: *Physics in Medicine and Biology* 51.17 (2006), pp. 4233–4251. DOI: 10.1088/0031-9155/51/17/008 (cit. on p. 16).

[27] W. Thomlinson et al. "K-edge subtraction synchrotron X-ray imaging in bio-medical research". In: *Physica Medica* 49 (2018), pp. 58–76. DOI: 10.1016/j.ejmp.2018.04.389 (cit. on p. 16).

[28] W. A. Kalender et al. "Evaluation of a prototype dual energy computed tomographic apparatus. I. Phantom studies". In: *Medical Physics* 13 (3 1986). ISSN: 00942405. DOI: 10.1118/1.595958 (cit. on p. 17).

[29] D. Zhang, X. Li, and B. Liu. "Objective characterization of GE Discovery CT750 HD scanner: Gemstone spectral imaging mode". In: *Medical Physics* 38 (3 2011). ISSN: 00942405. DOI: 10.1118/1.3551999 (cit. on p. 17).

[30] T. G. Flohr et al. "First performance evaluation of a dual-source CT (DSCT) system". In: *European Radiology* 16.2 (2006), pp. 256–268. DOI: 10.1007/s00330-005-2919-2 (cit. on p. 17).

[31] N. Rassouli et al. "Detector-based spectral CT with a novel dual-layer technology: principles and applications". In: *Insights into Imaging* 8 (6 2017). ISSN: 18694101. DOI: 10.1007/s13244-017-0571-4 (cit. on pp. 18, 19).

[32] K. Taguchi and J. S. Iwanczyk. "Vision 20/20: Single photon counting x-ray detectors in medical imaging". In: *Medical Physics* 40.10 (2013), p. 100901. DOI: 10.1118/1.4820371 (cit. on pp. 19, 20, 25, 56).

[33] E. Sato et al. "Investigation of dual-energy X-ray photon counting using a cadmium telluride detector with dual-energy selection electronics". In: *Radiation Physics and Chemistry* 130 (2017), pp. 385–390. DOI: 10.1016/j.radphyschem.2016.09.018 (cit. on p. 19).

[34] Y. Lee, A.C. Lee, and H.-J. Kim. "A Monte Carlo simulation study of an improved K-edge log-subtraction X-ray imaging using a photon counting CdTe detector". In: *Nuclear Instruments and Methods in Physics Research, Section A: Accelerators, Spectrometers, Detectors and Associated Equipment* 830 (2016), pp. 381–390. DOI: 10.1016/j.nima.2016.06.024 (cit. on p. 19).

[35] R. Ballabriga et al. "Review of hybrid pixel detector readout ASICs for spectroscopic X-ray imaging". In: *Journal of Instrumentation* 11.01 (2016), P01007. DOI: 10.1088/1748-0221/11/01/p01007 (cit. on pp. 20, 27, 56, 85).

[36] P. Delogu et al. "Characterization of Pixirad-1 photon counting detector for X-ray imaging". In: *Journal of Instrumentation* 11.01 (2016), P01015. DOI: 10.1088/1748-0221/11/01/p01015 (cit. on pp. 20, 26, 34, 41).

[37] E. Guni et al. "The Influence of Pixel Pitch and Electrode Pad Size on the Spectroscopic Performance of a Photon Counting Pixel Detector With CdTe Sensor". In: *IEEE Transactions on Nuclear Science* 58.1 (2011), pp. 17–25. ISSN: 0018-9499 (cit. on pp. 20, 26).

[38] A. Vincenzi et al. "Energy characterization of Pixirad-1 photon counting detector system". In: *Journal of Instrumentation* 10.04 (2015), p. C04010. DOI: 10.1088/1748-0221/10/04/c04010 (cit. on pp. 20, 26, 38, 39, 56, 85).

[39] P. Zambon et al. "Spectral response characterization of CdTe sensors of different pixel size with the IBEX ASIC". In: *Nuclear Instruments and Methods in Physics Research Section A: Accelerators, Spectrometers, Detectors and Associated Equipment* 892 (2018), pp. 106 –113. ISSN: 0168-9002. DOI: https://doi.org/10.1016/j.nima.2018.03.006 (cit. on pp. 20, 26).

[40] M. C. Veale et al. "Measurements of charge sharing in small pixel CdTe detectors". In: *Nuclear Instruments and Methods in Physics Research Section A: Accelerators, Spectrometers, Detectors and Associated Equipment* 767 (2014), pp. 218 –226. ISSN: 0168-9002. DOI: https://doi.org/10.1016/j.nima.2014.08.036 (cit. on pp. 20, 26).

[41] R. Ballabriga et al. "Characterization of the Medipix3 pixel readout chip". In: *Journal of Instrumentation* 6.01 (2011), p. C01052. DOI: 10.1088/1748-0221/6/01/c01052 (cit. on p. 20).

[42] J. P. Ronaldson et al. "Characterization of Medipix3 with the MARS readout and software". In: *Journal of Instrumentation* 6.01 (2011), p. C01056. DOI: 10.1088/1748-0221/6/01/c01056 (cit. on p. 20).

[43] V. Di Trapani et al. "Characterization of noise and efficiency of the Pixirad-1/Pixie-III CdTe X-ray imaging detector". In: *Journal of Instrumentation* 13.12 (2018), p. C12008. DOI: 10.1088/1748-0221/13/12/c12008 (cit. on p. 20).

[44] V. Di Trapani et al. "Characterization of the acquisition modes implemented in Pixirad-1/Pixie-III X-ray Detector: Effects of charge sharing correction on spectral resolution and image quality". In: *Nuclear Instruments and Methods in Physics Research, Section A: Accelerators, Spectrometers, Detectors and Associated Equipment* 955 (2020). DOI: 10.1016/j.nima.2019.163220 (cit. on p. 20).

[45] M. F. Walsh et al. "First CT using Medipix3 and the MARS-CT-3 spectral scanner". In: *Journal of Instrumentation* 6.01 (2011), p. C01095. DOI: 10.1088/1748-0221/6/01/c01095 (cit. on p. 21).

[46] T. Koenig et al. "How spectroscopic x-ray imaging benefits from inter-pixel communication". In: *Physics in Medicine and Biology* 59.20 (2014), pp. 6195–6213. DOI: 10.1088/0031-9155/59/20/6195 (cit. on p. 21).

[47] F. Brun et al. "Single-shot K-edge subtraction x-ray discrete computed tomography with a polychromatic source and the Pixie-III detector". In: *Physics in Medicine & Biology* 65.5 (2020), p. 055016. DOI: 10.1088/1361-6560/ab7105 (cit. on p. 21).

[48] F. Brun et al. "K-edge spectral computed tomography with a photon counting detector and discrete reconstruction". In: *2018 40th Annual International Conference of the IEEE Engineering in Medicine and Biology Society (EMBC)*. 2018, pp. 5245–5248. DOI: 10.1109/EMBC.2018.8513425 (cit. on pp. 21, 28).

[49] F. Brun et al. "Towards In Vivo K-Edge X-Ray Micro-CT with the Pixirad-I/Pixie-III Detector". In: *World Congress on Medical Physics and Biomedical Engineering 2018*. Ed. by Lenka Lhotska et al. Singapore: Springer Singapore, 2019, pp. 123–126 (cit. on pp. 21, 28).

[50] F. Brun et al. "Edge-subtraction X-ray ptychographic imaging with pink beam synchrotron radiation and a single photon-counting detector". In: *Scientific Reports* 10.1 (2020). DOI: 10.1038/s41598-020-63161-x (cit. on p. 21).

[51] P. Suortti et al. "A single crystal bent Laue monochromator for coronary angiography". In: *Nuclear Inst. and Methods in Physics Research, A* 336.1-2 (1993), pp. 304–309. DOI: 10.1016/0168-9002(93)91114-3 (cit. on pp. 21, 22, 113).

[52] P. Suortti et al. "Performance evaluation of a bent Laue monochromator". In: *Nuclear Instruments and Methods in Physics Research Section A: Accelerators, Spectrometers, Detectors and Associated Equipment* 297.1 (1990), pp. 268 –274. ISSN: 0168-9002. DOI: https://doi.org/10.1016/0168-9002(90)91375-L (cit. on p. 21).

[53] P. Suortti and W. Thomlinson. "A bent laue crystal monochromator for angiography at the NSLS". In: *Nuclear Instruments and Methods in Physics Research Section A: Accelerators, Spectrometers, Detectors and Associated Equipment* 269.3 (1988), pp. 639 –648. ISSN: 0168-9002. DOI: https://doi.org/10.1016/0168-9002(88)90145-3 (cit. on p. 21).

[54] Y. Zhu et al. "Spectral K-edge subtraction imaging". In: *Physics in Medicine and Biology* 59.10 (2014), pp. 2485–2503. DOI: 10.1088/0031-9155/59/10/2485 (cit. on pp. 21, 22, 113).

[55] B. Bassey et al. "Multiple energy synchrotron biomedical imaging system". In: *Physics in Medicine and Biology* 61.23 (2016), pp. 8180–8198. DOI: 10.1088/0031-9155/61/23/8180 (cit. on pp. 21, 22, 113, 121).

[56] P. Qi et al. "Wide field imaging energy dispersive X-ray absorption spectroscopy". In: *Scientific Reports* 9 (1 2019). ISSN: 20452322. DOI: 10.1038/s41598-019-54287-8 (cit. on pp. 22, 113, 115).

[57] B. Bassey et al. "Crossover artifact in X-ray focusing imaging systems: K-edge subtraction imaging". In: *Nuclear Instruments and Methods in Physics Research, Section A: Accelerators, Spectrometers, Detectors and Associated Equipment* 910 (2018), pp. 26–34. DOI: 10.1016/j.nima.2018.08.072 (cit. on p. 22).

[58] A. Panahifar et al. "Spectral K-edge subtraction imaging of experimental non-radioactive barium uptake in bone". In: *Physica Medica* 32.12 (2016), pp. 1765–1770. DOI: 10.1016/j.ejmp.2016.07.619 (cit. on p. 22).

[59] N. Samadi et al. "An energy dispersive bent Laue monochromator for K-edge subtraction imaging". In: vol. 1741. 2016. DOI: 10.1063/1.4952876 (cit. on pp. 22, 113, 115).

[60] D. Pacella. "Energy-resolved X-ray detectors: The future of diagnostic imaging". In: *Reports in Medical Imaging* 8 (Jan. 2015), p. 1. DOI: 10.2147/RMI.S50045 (cit. on pp. 25, 56).

[61] S. Weigel et al. "Digital Mammography Screening with Photon-counting Technique: Can a High Diagnostic Performance Be Realized at Low Mean Glandular Dose?" In: *Radiology* 271.2 (2014), pp. 345–355. DOI: 10.1148/radiol.13131181 (cit. on p. 25).

[62] N. Berger et al. "Dedicated Breast Computed Tomography With a Photon-Counting Detector: Initial Results of Clinical In Vivo Imaging". In: *Investigative radiology* Publish Ahead of Print (Mar. 2019). DOI: 10.1097/RLI.0000000000000552 (cit. on p. 25).

[63] L. Brombal et al. "Large-area single-photon-counting CdTe detector for synchrotron radiation computed tomography: a dedicated pre-processing procedure". In: *Journal of Synchrotron Radiation* 25.4 (2018), pp. 1068–1077. DOI: 10.1107/S1600577518006197 (cit. on p. 25).

[64] R. Longo et al. "Advancement in phase-contrast breast CT using monochromatic beam". In: *Journal of Synchrotron Radiation* (2019) (cit. on p. 25).

[65] H. Spieler. *Semiconductor Detector Systems*. Oxford University Press, 2005. DOI: 10.1093/acprof:oso/9780198527848.001.0001 (cit. on p. 26).

[66] G. Pellegrini et al. "Performance limits of a 55-/spl mu/m pixel CdTe detector". In: *IEEE Transactions on Nuclear Science* 53.1 (2006), pp. 361–366. ISSN: 0018-9499 (cit. on p. 26).

[67] E. N. Gimenez et al. "Study of charge-sharing in MEDIPIX3 using a micro-focused synchrotron beam". In: *Journal of Instrumentation* 6.01 (2011), pp. C01031–C01031. DOI: 10.1088/1748-0221/6/01/c01031 (cit. on p. 26).

[68] F. C. M. Lopez et al. "Comparator threshold settings and the effective pixel width of the PICASSO detector". In: *Journal of Instrumentation* 9.05 (2014), pp. C05056–C05056. DOI: 10.1088/1748-0221/9/05/c05056 (cit. on pp. 26, 41).

[69] X. Llopart et al. "Medipix2: A 64-k pixel readout chip with 55-/spl mu/m square elements working in single photon counting mode". In: *IEEE Transactions on Nuclear Science* 49.5 (2002), pp. 2279–2283. DOI: 10.1109/TNS.2002.803788 (cit. on p. 27).

[70] L. Rossi et al. *Pixel Detectors: From Fundamentals to Applications*. Berlin, Heidelberg: Springer Berlin Heidelberg, 2006. DOI: 10.1007/3-540-28333-1 (cit. on p. 27).

[71] C. Ullberg et al. "Measurements of a dual-energy fast photon counting CdTe detector with integrated charge sharing correction". In: *proc. SPIE* 8668 (2013). DOI: 10.1117/12.2007892 (cit. on p. 27).

[72] R. Bellazzini et al. "PIXIE III: a very large area photon-counting CMOS pixel ASIC for sharp X-ray spectral imaging". In: *Journal of Instrumentation* 10.01 (2015), pp. C01032–C01032. DOI: 10.1088/1748-0221/10/01/c01032 (cit. on p. 27).

[73] P. Maj et al. "Measurements of Matching and Noise Performance of a Prototype Readout Chip in 40 nm CMOS Process for Hybrid Pixel Detectors". In: *IEEE Transactions on Nuclear Science* 62.1 (2015), pp. 359–367. ISSN: 0018-9499. DOI: 10.1109/TNS.2014.2385595 (cit. on p. 27).

[74] P. Otfinowski and A. Krzyżanowska. "Algorithms for elimination of charge sharing effects in single photon counting pixel detectors". In: *2017 MIXDES - 24th International Conference "Mixed Design of Integrated Circuits and Systems*. 2017, pp. 211–214. DOI: 10.23919/MIXDES.2017.8005185 (cit. on p. 27).

[75] H. E. Nilsson et al. "Charge sharing suppression using pixel-to-pixel communication in photon counting X-ray imaging systems". In: *Nuclear Instruments and Methods in Physics Research Section A: Accelerators, Spectrometers, Detectors and Associated Equipment* 576.1 (2007). Proceedings of the 8th International

Workshop on Radiation Imaging Detectors, pp. 243 –247. ISSN: 0168-9002. DOI: https://doi.org/10.1016/j.nima.2007.01.160 (cit. on p. 27).

[76] P. Maj et al. "Algorithms for minimization of charge sharing effects in a hybrid pixel detector taking into account hardware limitations in deep submicron technology". In: *Journal of Instrumentation* 7.12 (2012), pp. C12020–C12020. DOI: 10.1088/1748-0221/7/12/c12020 (cit. on p. 27).

[77] M. Campbell et al. "Method for determining a particle and sensor device therefor". Pat. US7667205 (cit. on p. 27).

[78] C. Ullberg et al. "Photon counting dual energy x-ray imaging at CT count rates: measurements and implications of in-pixel charge sharing correction". In: *Medical Imaging 2018: Physics of Medical Imaging*. Vol. 10573. International Society for Optics and Photonics. SPIE, 2018, pp. 316 –323. DOI: 10.1117/12.2293591 (cit. on p. 27).

[79] P. Grybos et al. "Measurements of Matching and High Count Rate Performance of Multichannel ASIC for Digital X-Ray Imaging Systems". In: *IEEE Transactions on Nuclear Science* 54.4 (2007), pp. 1207–1215. DOI: 10.1109/TNS.2007.903176 (cit. on p. 27).

[80] P. Coan et al. "In vivo x-ray phase contrast analyzer-based imaging for longitudinal osteoarthritis studies in guinea pigs". In: *Physics in medicine and biology* 55 (Dec. 2010), pp. 7649–62. DOI: 10.1088/0031-9155/55/24/017 (cit. on pp. 28, 50).

[81] L. Broche et al. "Dynamic Mechanical Interactions Between Neighboring Airspaces Determine Cyclic Opening and Closure in Injured Lung". In: *Critical care medicine* 45 (Jan. 2017). DOI: 10.1097/CCM.0000000000002234 (cit. on pp. 28, 50).

[82] M. Ruat and C. Ponchut. "Defect signature, instabilities and polarization in CdTe X-ray sensors with quasi-ohmic contacts". In: *Journal of Instrumentation* 9.04 (2014), pp. C04030–C04030. DOI: 10.1088/1748-0221/9/04/c04030 (cit. on p. 30).

[83] V. Astromskas et al. "Evaluation of Polarization Effects of e^- Collection Schottky CdTe Medipix3RX Hybrid Pixel Detector". In: *IEEE Transactions on Nuclear Science* 63.1 (2016), pp. 252–258. DOI: 10.1109/TNS.2016.2516827 (cit. on p. 30).

[84] S. E. Park et al. "A flat-field correction method for photon-counting-detector-based micro-CT". In: *Medical Imaging 2014: Physics of Medical Imaging*. Vol. 9033. International Society for Optics and Photonics. SPIE, 2014, pp. 1536 –1542. DOI: 10.1117/12.2043317 (cit. on p. 30).

[85] P. Delogu et al. "Optimization of the equalization procedure for a single-photon counting CdTe detector used for CT". In: *Journal of Instrumentation* 12.11 (2017), pp. C11014–C11014. DOI: 10.1088/1748-0221/12/11/c11014 (cit. on pp. 30, 56).

[86] I. A. Cunningham. "Applied Linear-Systems Theory". In: *Handbook of Medical Imaging, Volume 1. Physics and Psychophysics*. Ed. by Richard L. Van Metter, Jacob Beutel, and Harold L. Kundel. Bellingham, WA, USA: SPIE, 2000. Chap. 2, pp. 79–160. DOI: https://doi.org/10.1117/3.832716.ch2 (cit. on pp. 30, 43, 75, 77, 82).

[87] J. T. Dobbins. "Image Quality Metrics for Digital Systems". In: *Handbook of Medical Imaging, Volume 1. Physics and Psychophysics*. Ed. by Richard L. Van Metter, Jacob Beutel, and Harold L. Kundel. Bellingham, WA, USA: SPIE, 2000. Chap. 3, pp. 161–222. DOI: https://doi.org/10.1117/3.832716.ch2 (cit. on pp. 30, 43–45, 48, 75).

[88] W. Vennart. "ICRU Report 54: Medical imaging - the assessment of image quality: ISBN 0-913394-53-X. April 1996, Maryland, U.S.A." In: *Radiography* 3.3 (1997), pp. 243 –244. ISSN: 1078-8174. DOI: https://doi.org/10.1016/S1078-8174(97)90038-9 (cit. on pp. 30, 45, 75).

[89] P. Suortti et al. "Fixed-exit monochromator for computed tomography with synchrotron radiation at energies 18–90keV". In: *Journal of Synchrotron Radiation* 7.5 (2000), pp. 340–347. DOI: 10.1107/S0909049500008384 (cit. on pp. 31, 38, 100).

[90] I. A. Cunningham and A. Fenster. "A method for modulation transfer function determination from edge profiles with correction for finite-element differentiation". In: *Medical Physics* 14.4 (1987), pp. 533–537. DOI: 10.1118/1.596064 (cit. on p. 40).

[91] I. A. Cunningham and B. K. Reid. "Signal and noise in modulation transfer function determinations using the slit, wire, and edge techniques". In: *Medical Physics* 19.4 (1992), pp. 1037–1044 (cit. on p. 40).

[92] E. Samei, M. J. Flynn, and D. A. Reimann. "A method for measuring the presampled MTF of digital radiographic systems using an edge test device". In: *Medical Physics* 25.1 (1998), pp. 102–113. DOI: 10.1118/1.598165 (cit. on p. 40).

[93] J. Marchal and K. Medjoubi. "Detective quantum efficiency model of single-X-ray-photon counting hybrid pixel detectors". In: *Journal of Instrumentation* 7 (Nov. 2012), P11028. DOI: 10.1088/1748-0221/7/11/P11028 (cit. on pp. 41, 44).

[94] International Electrotechnical Commission. "Medical electrical equipment-Characteristics of digital X-ray imaging devices Part-1: determination of the detective quantum efficiency". In: *IEC 62220-1 Geneva: IEC* (2003) (cit. on p. 44).

[95] M. L. Giger and K. Doi. "Investigation of basic imaging properties in digital radiography. I. Modulation transfer function". In: *Medical Physics* 11.3 (1984), pp. 287–295. DOI: 10.1118/1.595629 (cit. on p. 45).

[96] P. Henrot et al. "Breast microcalcifications: The lesions in anatomical pathology". In: *Diagnostic and Interventional Imaging* 95.2 (2014). Radio-histological correlations in breast imaging, pp. 141 –152. ISSN: 2211-5684. DOI: https://doi.org/10.1016/j.diii.2013.12.011 (cit. on p. 50).

[97] P. Delogu et al. "Imaging study of a phase-sensitive breast-CT system in continuous acquisition mode". In: *Journal of Instrumentation* 12.01 (2017), pp. C01016–C01016. DOI: 10.1088/1748-0221/12/01/c01016 (cit. on p. 56).

[98] E. N. Gimenez et al. "Characterization of Medipix3 With Synchrotron Radiation". In: *IEEE Transactions on Nuclear Science* 58.1 (2011), pp. 323–332. DOI: 10.1109/TNS.2010.2089062 (cit. on p. 56).

[99] R. L. Baer. "Circular-edge spatial frequency response test". In: *Image Quality and System Performance*. Vol. 5294. International Society for Optics and Photonics. 2004, pp. 71–81. DOI: 10.1117/12.524829 (cit. on p. 57).

[100] S. N. Friedman et al. "A simple approach to measure computed tomography (CT) modulation transfer function (MTF) and noise-power spectrum (NPS) using the American College of Radiology (ACR) accreditation phantom". In: *Medical Physics* 40.5 (2013). DOI: 10.1118/1.4800795 (cit. on p. 57).

[101] T. Takenaga et al. "Modulation transfer function measurement of CT images by use of a circular edge method with a logistic curve-fitting technique". In: *Radiological Physics and Technology* 8.1 (2015), pp. 53–59. DOI: 10.1007/s12194-014-0286-x (cit. on p. 57).

[102] A. Biguri et al. "TIGRE: a MATLAB-GPU toolbox for CBCT image reconstruction". In: *Biomedical Physics & Engineering Express* 2.5 (2016), p. 055010. DOI: 10.1088/2057-1976/2/5/055010 (cit. on p. 58).

[103] A. Biguri et al. "Arbitrarily large tomography with iterative algorithms on multiple GPUs using the TIGRE toolbox". In: 146 (2020), pp. 52–63. DOI: 10.1016/j.jpdc.2020.07.004 (cit. on p. 58).

[104] H. Hwang and R. A. Haddad. "Adaptive median filters: new algorithms and results". In: *IEEE Transactions on Image Processing* 4.4 (1995), pp. 499–502. DOI: 10.1109/83.370679 (cit. on p. 59).

[105] M. E. Eldib et al. "A ring artifact correction method: Validation by micro-CT imaging with flat-panel detectors and a 2D photon-counting detector". In: *Sensors (Switzerland)* 17.2 (2017). DOI: 10.3390/s17020269 (cit. on p. 63).

[106] J. Sijbers and A. Postnov. "Reduction of ring artefacts in high resolution micro-CT reconstructions". In: *Physics in Medicine and Biology* 49.14 (2004), N247–N253. DOI: 10.1088/0031-9155/49/14/n06 (cit. on pp. 63, 64).

[107] M. J. Oimoen. "An Effective Filter for Removal of Production Artifacts in U.S. Geological Survey 7.5-Minute Digital Elevation Models". In: *Proc. 14th Intl Conf. Appl. Geol. Remote Sens.* Las Vegas, N USAV, 2000, pp. 311–319 (cit. on pp. 63, 64, 70, 72, 74).

[108] X. Tang et al. "Cone beam volume CT image artifacts caused by defective cells in x-ray flat panel imagers and the artifact removal using a wavelet-analysis-based algorithm". In: *Medical Physics* 28.5 (2001), pp. 812–825. DOI: 10.1118/1.1368878 (cit. on p. 63).

[109] M. Boin and A. Haibel. "Compensation of ring artefacts in synchrotron tomographic images". In: *Opt. Express* 14.25 (2006), pp. 12071–12075. DOI: 10.1364/OE.14.012071 (cit. on p. 63).

[110] B. Münch et al. "Stripe and ring artifact removal with combined wavelet- Fourier filtering". In: *Opt. Express* 17.10 (2009), pp. 8567–8591. DOI: 10.1364/OE.17.008567 (cit. on pp. 63, 64).

[111] E. M. A. Anas, S. Y. Lee, and Md. K. Hasan. "Removal of ring artifacts in CT imaging through detection and correction of stripes in the sinogram". In: *Physics in Medicine and Biology* 55.22 (2010), pp. 6911–6930. DOI: 10.1088/0031-9155/55/22/020 (cit. on p. 63).

[112] M. Axelsson, S. Svensson, and G. Borgefors. "Reduction of Ring Artifacts in High Resolution X-Ray Microtomography Images". In: *Pattern Recognition*. Ed. by Katrin Franke et al. Berlin, Heidelberg: Springer Berlin Heidelberg, 2006, pp. 61–70 (cit. on p. 64).

[113] F. Brun et al. "An improved method for ring artifacts removing in reconstructed tomographic images". In: *World Congress on Medical Physics and Biomedical Engineering, September 7 - 12, 2009, Munich, Germany*. Ed. by Olaf Dössel and Wolfgang C. Schlegel. Berlin, Heidelberg: Springer Berlin Heidelberg, 2010, pp. 926–929. DOI: 10.1007/978-3-642-03882-2_247 (cit. on p. 64).

[114] F. Brun et al. “Effective implementation of ring artifacts removal filters for synchrotron radiation microtomographic images”. In: *2013 8th International Symposium on Image and Signal Processing and Analysis (ISPA)*. 2013, pp. 672–676. DOI: 10.1109/ISPA.2013.6703823 (cit. on p. 64).

[115] D. Prell, Y. Kyriakou, and W. A. Kalender. “Comparison of ring artifact correction methods for flat-detector CT”. In: *Physics in Medicine and Biology* 54.12 (2009), pp. 3881–3895. DOI: 10.1088/0031-9155/54/12/018 (cit. on p. 64).

[116] M. Rivers. *Tutorial introduction to x-ray computed microtomography data processing, 1998*. URL: http://www.mcs.anl.gov/research/projects/X-raycmt/rivers/tutorial.html. (accessed: 01.01.2020) (cit. on p. 64).

[117] C. Raven. “Numerical removal of ring artifacts in microtomography”. In: *Review of Scientific Instruments* 69.8 (1998), pp. 2978–2980. DOI: 10.1063/1.1149043 (cit. on p. 64).

[118] S. J. Riederer, N. J. Pelc, and D. A. Chesler. “The noise power spectrum in computed X-ray tomography”. In: *Physics in Medicine and Biology* 23 (3 1978). DOI: 10.1088/0031-9155/23/3/008 (cit. on p. 76).

[119] H. H. Barrett, S. K. Gordon, and R. S. Hershel. “Statistical limitations in transaxial tomography”. In: *Computers in Biology and Medicine* 6 (4 1976). DOI: 10.1016/0010-4825(76)90068-8 (cit. on p. 76).

[120] R. F. Wagner, D. G. Brown, and M. S. Pastel. “Application of information theory to the assessment of computed tomography”. In: *Medical Physics* 6 (2 1979). DOI: 10.1118/1.594559 (cit. on p. 76).

[121] A. Savitzky and M.J.E. Golay. “Smoothing and Differentiation of Data by Simplified Least Squares Procedures”. In: *Analytical Chemistry* 36.8 (1964), pp. 1627–1639. DOI: 10.1021/ac60214a047 (cit. on pp. 77, 90).

[122] P. Delogu et al. “Optimization of the energy for Breast monochromatic absorption X-ray Computed Tomography”. In: *Scientific Reports* 9 (2019). DOI: 10.1038/s41598-019-49351-2 (cit. on p. 83).

[123] P. Oliva et al. “Experimental optimization of the energy for breast-CT with synchrotron radiation”. In: *Scientific Reports* 10.1 (2020). DOI: 10.1038/s41598-020-74607-7 (cit. on p. 83).

[124] J. Punnoose et al. “Technical Note: Spektr 3.0 - A computational tool for x-ray spectrum modeling and analysis”. In: *Medical Physics* 43.8 (2016), pp. 4711–4717. DOI: 10.1118/1.4955438 (cit. on p. 84).

[125] A. M. Hernandez and J. M. Boone. "Tungsten anode spectral model using interpolating cubic splines: Unfiltered x-ray spectra from 20 kV to 640 kV". In: *Medical Physics* 41.4 (2014). DOI: 10.1118/1.4866216 (cit. on p. 84).

[126] L. Rossi et al. *Pixel Detectors: from Fundamentals to Applications*. Jan. 2006. DOI: 10.1007/3-540-28333-1 (cit. on p. 85).

[127] A. Owens and A. Peacock. "Compound semiconductor radiation detectors". In: *Nuclear Instruments and Methods in Physics Research Section A: Accelerators, Spectrometers, Detectors and Associated Equipment* 531.1 (2004). Proceedings of the 5th International Workshop on Radiation Imaging Detectors, pp. 18–37. DOI: https://doi.org/10.1016/j.nima.2004.05.071 (cit. on p. 85).

[128] S. Y. Wan, E. L. Ritman, and W. E. Higgins. "Multi-generational analysis and visualization of the vascular tree in 3D micro-CT images". In: *Computers in Biology and Medicine* 32 (2 2002). ISSN: 00104825. DOI: 10.1016/S0010-4825(01)00034-8 (cit. on p. 97).

[129] S. Grabherr et al. "Angiofil®-mediated visualization of the vascular system by microcomputed tomography: A feasibility study". In: *Microscopy Research and Technique* 71 (7 2008). ISSN: 1059910X. DOI: 10.1002/jemt.20585 (cit. on p. 97).

[130] L. Zagorchev et al. "Micro computed tomography for vascular exploration". In: *Journal of Angiogenesis Research* 2 (1 2010). ISSN: 20402384. DOI: 10.1186/2040-2384-2-7 (cit. on p. 97).

[131] G. T. Herman and A. Kuba. "Discrete tomography in medical imaging". In: vol. 91. 2003. DOI: 10.1109/JPROC.2003.817871 (cit. on p. 98).

[132] K. J. Batenburg et al. "3D imaging of nanomaterials by discrete tomography". In: *Ultramicroscopy* 109 (6 2009). ISSN: 03043991. DOI: 10.1016/j.ultramic.2009.01.009 (cit. on pp. 98, 102).

[133] X. Zhuge, W. J. Palenstijn, and K. J. Batenburg. "TVR-DART: A more robust algorithm for discrete tomography from limited projection data with automated gray value estimation". In: *IEEE Transactions on Image Processing* 25 (1 2016). ISSN: 10577149. DOI: 10.1109/TIP.2015.2504869 (cit. on pp. 98, 102).

[134] P. Retif et al. "Nanoparticles for radiation therapy enhancement: The key parameters". In: *Theranostics* 5 (9 2015). ISSN: 18387640. DOI: 10.7150/thno.11642 (cit. on pp. 98, 111).

[135] C. Maenz et al. "Epithelial-mesenchymal plasticity is a decisive feature for the metastatic outgrowth of disseminated WAP-T mouse mammary carcinoma cells". In: *BMC Cancer* 15.1 (2015). DOI: 10.1186/s12885-015-1165-5 (cit. on p. 100).

[136] M. Endrizzi et al. "CMOS APS detector characterization for quantitative X-ray imaging". In: *Nuclear Instruments and Methods in Physics Research Section A: Accelerators, Spectrometers, Detectors and Associated Equipment* 703 (2013), pp. 26–32. ISSN: 0168-9002. DOI: https://doi.org/10.1016/j.nima.2012.11.080 (cit. on p. 100).

[137] A. Mittone et al. "Characterization of a sCMOS-based high-resolution imaging system". In: *Journal of Synchrotron Radiation* 24 (6 2017). ISSN: 16005775. DOI: 10.1107/S160057751701222X (cit. on p. 100).

[138] G. G. Poludniowski. "Calculation of x-ray spectra emerging from an x-ray tube. Part II. X-ray production and filtration in x-ray targets". In: *Medical Physics* 34 (6 2007). ISSN: 00942405. DOI: 10.1118/1.2734726 (cit. on p. 102).

[139] G. G. Poludniowski and P. M. Evans. "Calculation of x-ray spectra emerging from an x-ray tube. Part I. Electron penetration characteristics in x-ray targets". In: *Medical Physics* 34 (6 2007). ISSN: 00942405. DOI: 10.1118/1.2734725 (cit. on p. 102).

[140] G. Poludniowski et al. "SpekCalc: A program to calculate photon spectra from tungsten anode x-ray tubes". In: *Physics in Medicine and Biology* 54 (19 2009). ISSN: 00319155. DOI: 10.1088/0031-9155/54/19/N01 (cit. on p. 102).

[141] J. Guo et al. "Gold nanoparticles enlighten the future of cancer theranostics". In: *International Journal of Nanomedicine* 12 (2017). ISSN: 11782013. DOI: 10.2147/IJN.S140772 (cit. on p. 111).

[142] P. Suortti, P. Pattison, and W. Weyrich. "X-ray spectrometer for inelastic scattering experiments. I. curved-crystal X-ray optics." In: *Journal of Applied Crystallography* 19 (pt 5 1986). ISSN: 00218898. DOI: 10.1107/S0021889886089264 (cit. on p. 113).

[143] E. Erola et al. "X-ray reflectivity of bent perfect crystals in Bragg and Laue geometry". In: *Journal of Applied Crystallography* 23 (1 1990). ISSN: 00218898. DOI: 10.1107/S0021889889010800 (cit. on p. 113).

[144] Z. Zhong et al. "A lamellar model for the x-ray rocking curves of sagittally bent Laue crystals". In: *Acta Crystallographica Section A: Foundations of Crystallography* 59 (1 2003). ISSN: 01087673. DOI: 10.1107/S0108767302016835 (cit. on pp. 113, 114).

[145] M. Sanchez Del Rio et al. "Simulation of X-ray diffraction profiles for bent anisotropic crystals". In: *Journal of Applied Crystallography* 48 (2015). ISSN: 16005767. DOI: 10.1107/S1600576715002782 (cit. on p. 113).

[146] M. Martinson et al. "Phase-preserving beam expander for biomedical X-ray imaging". In: *Journal of Synchrotron Radiation* 22 (2015). ISSN: 16005775. DOI: 10.1107/S1600577515004695 (cit. on p. 113).

[147] P. Qi et al. "Focusing and Energy Dispersion Properties of a Cylindrically Bent Asymmetric Laue Crystal". In: *arXiv* (2020). ISSN: 23318422. DOI: 10.1117/12.2525449 (cit. on p. 113).

[148] P. Qi et al. "Bent Laue crystal anatomy: new insights into focusing and energy-dispersion properties". In: *Journal of Applied Crystallography* 54.2 (2021), pp. 409–426. DOI: https://doi.org/10.1107/S1600576720016428 (cit. on pp. 113, 115).

[149] J. J. Wortman and R. A. Evans. "Young's Modulus, Shear Modulus, and Poisson's Ratio in Silicon and Germanium". In: *Journal of Applied Physics* 36.1 (1965), pp. 153–156. DOI: 10.1063/1.1713863 (cit. on p. 114).

[150] L. Zhang et al. "Anisotropic elasticity of silicon and its application to the modelling of X-ray optics". In: *Journal of Synchrotron Radiation* 21.3 (2014), pp. 507–517. DOI: 10.1107/S1600577514004962 (cit. on p. 114).

[151] K. A. L. Koch-Mehrin, J. E. Lees, and S. L. Bugby. "A spectroscopic Monte-Carlo model to simulate the response of pixelated CdTe based detectors". In: *Nuclear Instruments and Methods in Physics Research, Section A: Accelerators, Spectrometers, Detectors and Associated Equipment* 976 (2020). DOI: 10.1016/j.nima.2020.164241 (cit. on pp. 135, 137).

[152] R. Jenkins. *Quantitative X-Ray Spectrometry*. 1995. DOI: 10.1201/9781482273380 (cit. on p. 136).

[153] N. Kaya, G. Apaydin, and E. Tirasoglu. "Measurement of K-shell jump ratios and jump factors for some elements in 76<Z<92 using EDXRF spectrometer". In: *Radiation Physics and Chemistry* 80.6 (2011), pp. 677–681. DOI: https://doi.org/10.1016/j.radphyschem.2011.02.001 (cit. on p. 137).

[154] A. Thompson et al. "X-Rray Data Booklet". In: *Lawrence Berkeley National Laboratory* (2009). ISSN: 09090495 (cit. on p. 137).